ABSTRACT

Title of Dissertation: MODELING AND SIMULATION OF A TUNGSTEN CHEMICAL VAPOR DEPOSITION REACTOR

Hsiao-Yung Chang, Doctor of Philosophy, 2000

Dissertation directed by: Assistant Professor Raymond A. Adomaitis
Department of Chemical Engineering

Chemical vapor deposition (CVD) processes are widely used in semiconductor device fabrication to deposit thin films of electronic materials. Physically based CVD modeling and simulation methods have been adopted for reactor design and process optimization applications to satisfy the increasingly strigent processing requirements. In this research, an ULVAC ERA-1000 selective tungsten chemical vapor deposition system located at the University of Maryland was studied where a temperature difference as large as 120 ^{o}C between the system wafer temperature reading and the thermocouple instrumented wafer measurement was found during the manual processing mode. The goal of this research was to develop a simplified, but accurate, three-dimensional transport model that is capable of describing the observed reactor behavior.

A hybrid approach combining experimental and simulation studies was used for model development. Several sets of experiments were conducted to investigate the effects of process parameters on wafer temperature. A three-dimensional gas flow and temperature model was developed and used to compute the energy transferred across the gas/wafer interface. System dependent heat transfer parameters were formulated as a nonlinear parameter estimation problem and identified using experimental measurements. Good agreement was found between the steady-state wafer temperature predictions and experimental data at various gas compositions, and the wafer temperature dynamics was successfully predicted using a temperature model considering the energy exchanges between the thermocouple, wafer, and showerhead.

MODELING AND SIMULATION OF A TUNGSTEN CHEMICAL VAPOR DEPOSITION REACTOR

by

Hsiao-Yung Chang

Dissertation submitted to the Faculty of the Graduate School of the
University of Maryland, College Park in partial fulfillment
of the requirements for the degree of
Doctor of Philosophy
2000

Advisory Committee:

Assistant Professor Raymond A. Adomaitis, Chairman/Advisor
Professor James W. Gentry
Associate Professor Michael T. Harris
Assistant Professor John N. Kidder, Jr.
Associate Professor Evanghelos Zafiriou

© Copyright by

Hsiao-Yung Chang

2000

Dedication

To my parents and sisters

Acknowledgements

Coming into the end of another phase in my life, it is only appropriate to think and acknowledge all the people who gave me the knowledge and support to pursue and complete another goal in my life.

First of all, I would like to express my appreciation and gratitude to my advisor, Dr. Raymond A. Adomaitis. It has been my privilege to study under his direction and I thank him for providing me his invaluable and thoughtful guidance, encouragement, and expertise on every subject that arose.

I would like to thank Drs. Gary W. Rubloff and John N. Kidder, Jr. for their generous support on my experimental work and their advice and expertise on a variety of topics.

I am grateful to all of my teachers. In particular, I would like to thank Dr. Evanghelos Zafiriou for his fascinating lectures, Drs. James W.

Gentry and Michael T. Harris for serving on my advisory committee and providing many valuable comments.

I have been fortunate to work with many talented and interesting colleagues. I would like to thank Dr. Yi-hung Lin, Jiefei Huang, and Ashish Suresh Sabadra for their efforts in MWRtools development and many useful discussions on the modeling and solution issues; Dr. Theodosia Gougousi, Laurent Henn-Lecordier, and Yiheng Xu for their technical support during the experimental work.

I have been blessed to receive the constant love, support, understanding, and encouragement of my parents, sisters, and friends. This accomplishments is theirs to share with me.

Table of Contents

List of Tables viii

List of Figures x

1 Introduction 1

2 Chemical Vapor Deposition Reactor Mathematical Modeling 8

2.1 Fundamentals of Chemical Vapor Deposition Processes 9

2.1.1 Rapid Thermal Chemical Vapor Deposition 11

2.1.2 Tungsten Chemical Vapor Deposition 12

2.1.3 Tungsten Chemical Vapor Deposition Chemical Mechanisms 13

2.2 Mathematical Modeling Overview of CVD Systems 16

2.2.1 CVD Transport Modeling 17

2.2.2 Literature Review 18

2.2.3 CVD Modeling Using Commercial CFD Software 27

2.2.4 General Modeling Assumptions 27

2.2.5 Gas Phase Transport Model 29

2.2.6 Wafer Thermal Dynamics Model 31

2.3 ULVAC Selective Tungsten Chemical Vapor Deposition Cluster Tool 33

2.4 ULVAC W CVD Transport Model Formulation 37
2.4.1 Gas Flow Field 37
2.4.2 Gas Temperature Field 42
2.4.3 Wafer Thermal Dynamics 43
2.4.4 Showerhead Thermal Dynamics 45
2.4.5 Thermocouple Thermal Dynamics 47
2.4.6 Gasous Reactants and Wafer Physical Properties 47
2.5 Dimensionless Equations 52
2.5.1 Gas Phase Flow and Energy Equations 52
2.5.2 Wafer and Showerhead Energy Balance Equations 55

3 Experimental Studies 57
3.1 Data Acquisition in the ULVAC ERA-1000 System 58
3.1.1 Instrumented Thermocouple Wafer and Computer Boards 61
3.1.2 LabVIEW Data Acquisition Interface 62
3.2 Lamp Control Signal Correction 65
3.3 Influence of Gas Composition on Wafer Temperature 69
3.4 Wafer Thermal Dynamics 75
3.4.1 Influence of the Chamber Pressure 76
3.4.2 Deposition Processing Window 78
3.4.3 Wafer Temperature Response of Single and Multiple Heating Cycles 80

4 Numerical Solution Procedures 89
4.1 Introduction to Method of Weighted Residuals 90
4.2 MWRtools 94

4.3 Introduction to Nonlinear Least-Squares Parameter Estimation . . 99
4.3.1 Nonlinear Least Squares Problem Formulation and the Newton Method 100
4.3.2 The Gauss-Newton Method 102

5 Simulation Results 104
5.1 Influence of Gas Composition on Steady-State Wafer Temperature 105
5.1.1 Parameter Estimation 107
5.1.2 Solution Procedure 108
5.1.3 Model Validation and Discussion 113
5.2 Wafer Thermal Dynamical Simulation 117
5.2.1 Single Equation Wafer Temperature Model 117
5.2.2 The Three Equation Temperature Simulator 121
5.2.3 Model Validation and Simulation Results 125

6 Conclusions and Future Work 132
6.1 Concluding Remarks 132
6.2 Suggested Future Work 134

Bibliography 136

List of Tables

2.1 Important dimensionless groups and their typical range in low pressure CVD (LPCVD) reactors. 29

2.2 Summary of the dimensionless variables used in the transport model. 52

2.3 Definitions and values of physical properties and dimensionless parameters evaluated at 1 atm, $H_2/N_2 = 40/10sccm$, $T_{amb} = 25$, $T_w = 304.3$, $T_{sh} = 150$, and $T_f = 60^o$C. 54

2.4 Definitions of dimensionless parameters used in wafer, shower-head, and thermocouple modeling equations. 56

3.1 Values of the lamp current and voltage and the lamp control signal. 67

3.2 Values of the fitting coefficients c_i in Equation (3.1). 69

4.1 List of current MWRtools functions used for initialization, collocation methods, and solution reconstruction. 96

4.2 List of the MWR functions especially designed for solving problems defined in higher dimensions. 97

4.3 List of classes in MWRtools and their corresponding methods. . . 98

5.1 A list of model parameter values, their estimated values or range, and the final values obtained from the identification procedure. . 114
5.2 A list of identified model parameter values. 125

List of Figures

1.1 Comparison of ULVAC CVD system adjusted wafer temperature and TC instrumented wafer measurements. 4

2.1 Schematic illustration of modeling approach. 17

2.2 Top view schematic ULVAC cluster tool. 33

2.3 Sketch of the Tungsten CVD reactor system. 35

2.4 ULVAC W CVD reactor operating and control structure. 36

2.5 The default ULVAC look-up table correcting functions plotted as the ULVAC thermocouple measurements against the adjusted wafer temperature at (top) 0.8 $Torr$ and (bottom) 0.4 $Torr$ total chamber pressure in pure H_2 or Ar gas. R1 and R2 represent the correcting function for reactors 1 and 2, respectively. 38

2.6 The default ULVAC look-up table correcting functions plotted as the ULVAC thermocouple measurements against the adjusted wafer temperature at (top) 0.17 $Torr$ and (bottom) 0.1 $Torr$ total chamber pressure in pure H_2 or Ar gas. R1 and R2 represent the correcting function for reactors 1 and 2, respectively. 39

2.7 The default ULVAC look-up table correcting functions plotted as the ULVAC thermocouple measurements against the adjusted wafer temperature at high vacuum condition $1.8\times10^{-6} Torr$ total chamber pressure in pure H_2 or Ar gas. R1 and R2 represent the correcting function for reactors 1 and 2, respectively. 40
2.8 Geometry of the heating lamp and wafer. 44
2.9 Radial variation of the lamp radiant heat flux at the wafer surface at full lamp power. 46

3.1 ULVAC CVD reactor data acquisition system. 59
3.2 The top and side views of the test wafer position with thermocouple positions marked. 61
3.3 LabVIEW data acquisition interface window. 63
3.4 Relationship of the ULVAC wafer temperature (top) and the steady-state lamp power control signal (bottom) at 0.2 $Torr$ total chamber pressure and 100 $sccm$ N_2. 66
3.5 Relationship of the lamp control signal and the true lamp power (computed by the product of lamp current and voltage). 68
3.6 The temperature response of the wafer to reactant gas composition variations. 71
3.7 The temperature response of the wafer to reactant gas flow rate and composition changes. 72
3.8 The temperature trajectory of a slightly shifted wafer during a process cycle at 0.5 $Torr$ and $H_2/N_2 = 40/10$ $sccm$. 73

3.9 Comparison of the wafer temperature in the first five minutes at different gas composition and 0.5 $Torr$. Dash-dotted curve (from Figure 3.15) was found using $H_2/N_2 = 40/10$ $sccm$ and the solid curves (from Figure 3.6) correspond to 100 $sccm$ H_2. 74

3.10 The ULVAC adjusted wafer temperature and the five thermocouple measurements of the instrumented wafer during a process cycle at (top) 0.17 $Torr$ and (bottom) 0.5 $Torr$ total chamber pressure in 2000 $sccm$ H_2. 77

3.11 Comparison of wafer temperature at different chamber pressure from Figure 3.10. 78

3.12 Process recipe found by adjusting initial heating sequence at 0.2 $Torr$ and $N_2 = 100$ $sccm$. 79

3.13 Process recipe (top) and corresponding lamp power signal (bottom) found by adjusting initial heating sequence at 0.5 $Torr$ and $H_2/N_2 = 40/10$ $sccm$. 81

3.14 The wafer temperature responses to ULVAC temperature setpoints 450 ^{o}C at 0.5 $Torr$ and $H_2/N_2 = 40/10$ $sccm$. 82

3.15 The wafer temperature responses to ULVAC temperature setpoints 500 ^{o}C at 0.5 $Torr$ and $H_2/N_2 = 40/10$ $sccm$. 83

3.16 The wafer temperature responses to ULVAC temperature setpoints 550 ^{o}C at 0.5 $Torr$ and $H_2/N_2 = 40/10$ $sccm$. 84

3.17 (Top) The TC wafer temperature responses to three different temperature setpoints at 0.5 $Torr$ and $H_2/N_2 = 40/10$ $sccm$. (Bottom) The temperature trajectories of each thermocouple at the beginning of the soak phase for the SP: 500 ^{o}C experiment. . . . 85

3.18 The TC wafer temperature responses during the first two minutes to three different temperature setpoints (top) and the corresponding lamp power signal (bottom) at 0.5 $Torr$ and $H_2/N_2 = 40/10$ $sccm$. 86

3.19 The wafer temperature identification trajectory (top) and the long term temperature drift comparison (bottom) at 0.5 $Torr$ and $H_2/N_2 = 40/10$ $sccm$. 87

3.20 The wafer temperature responses to multiple heating cycles for model validation at 0.5 $Torr$ and $H_2/N_2 = 40/10$ $sccm$. 88

5.1 (a) Gas flow field and temperature contours where each contour represents 50 K temperature difference. (b) Wafer/gas heat transfer rate at centerline of the reactor chamber. Simulation performed at $N_2 = 100$ $sccm$ and 500 $mTorr$. (c) Difference of heat flux across wafer/gas boundary between $N_2 = 100$ and 60 $sccm$, where $\Delta q = q_{N_2=100} - q_{N_2=60}$. 110

5.2 Wafer temperature from experimental data (solid curves with circles at data points) and model prediction (dot-dash curves and squares). 112

5.3 Contributions of individual heat transfer mechanisms for (a) interior region, and (b) region outside the susceptor. 115

5.4 Comparison of the wafer temperature between the experimental measurements $T_{w,exp}$ (from Figure 3.19) and the single equation nonlinear wafer temperature model predictions $T_{w,1}, T_{w,2}$ and $T_{w,3}$ for a multiple heating cycles process. 120

5.5 The wafer temperature (thermocouples) fast response to the lamp power variations during setpoint changes. Data are taken from Figure 3.19. 122
5.6 The wafer temperature prediction from the identified model. Results are compared with experimental data shown in Figure 3.19. 124
5.7 The wafer temperature prediction from the identified model. Results are compared with experimental data shown in Figure 3.20. 126
5.8 The wafer temperature prediction from the identified model. Results are compared with experimental data shown in Figure 3.14. 128
5.9 The wafer temperature prediction from the identified model. Results are compared with experimental data shown in Figure 3.15. 129
5.10 The wafer temperature prediction from the identified model. Results are compared with experimental data shown in Figure 3.16. 130
5.11 The wafer temperature prediction from the identified model for processing window shown in Figure 3.13. 131

MODELING AND SIMULATION OF A
TUNGSTEN CHEMICAL VAPOR
DEPOSITION REACTOR

Hsiao-Yung Chang

August 1, 2000

This comment page is not part of the dissertation.

Typeset by LaTeX using the `dissertation` style by Pablo A. Straub, University of Maryland.

Chapter 1

Introduction

Chemical vapor deposition (CVD) is a technique extensively used in the semiconductor industry to form nonvolatile solid films on a substrate from chemical reactions fed by vapor phase reactants. Compared with other deposition techniques, CVD offers good control of film structure and composition, high growth rates, excellent uniformity and conformality, and can deposit a wide variety of materials: doped and undoped silicon oxide, polysilicon, epitaxial silicon, silicide, silicon nitride, tungsten, titanium, copper, and aluminum when manufacturing silicon-based integrated circuits. Some III-V and II-VI compounds and more complex opto-electronic compounds can also be processed using CVD. These versatile processing properties and the wide selection of materials make the CVD techniques useful in many manufacturing steps in both the front-end devices and back-end interconnect processes.

As the dimensions of the microelectronic devices decreases and the diameter of the wafers increase, to ensure the quality of the deposited films, e.g., the thickness, composition, and microstructure, be reproducible and uniform within wafer itself and from wafer to wafer in a processing batch is a critical manufacturing

requirement. To meet the more stringent requirements imposed by continually shrinking device sizes, physically based process modeling and simulation methods have been gradually adopted as both a design tool in the development of semiconductor manufacturing equipment [1] and a platform for process optimization of the existing systems using experimentally validated physical models [2]. The value of process modeling is especially underscored by its broad acceptance [3, 4, 5, 6, 7, 8] in CVD control systems design or improvement.

Many research studies have focused on modeling the equipment and process transport phenomena in different type of CVD systems, as those summarized in Kleijn [9], Jensen et. al. [10], and Badgwell et. al. [11]. Although some approaches, such as thermodynamic equilibrium [12], particle transport modeling (PTM) [13], and the Monte Carlo (MC) simulations on trench step coverage [14, 15], are employed for various simulation purposes, most of the modeling studies are based on the macroscopic transport phenomena in the different types of the CVD reactors. In addition to studying the process parameters on reactor performance, chamber design, scale up, and process control applications, these first-principle CVD equipment models can also be used to help understand the process physics by providing the information on various transport and reaction mechanisms.

With the help of the development of computational fluid dynamics (CFD), these first-principle transport models are becoming more comprehensive and accurate. However, in order to reach the best predictive results, the computational efficiency is sacrificed by finely discretizing the model equations with either finite-element (FEM) [16], or finite-volume (FVM) [17], or finite-difference (FDM) [18] methods. Because these discretization schemes use spatially localized basis func-

tions which determine the corresponding numerical values of the equations only at each separate local basis, obtaining acceptable resolution of simulation results requires a large number of basis functions which increases the total computing time.

Motivation and Goals of this Research

In this research, we focus on the ULVAC ERA-1000 selective tungsten chemical vapor deposition cluster tool that is located at the University of Maryland, College Park. This CVD system is designed for selectively depositing tungsten into the via or contact holes that connect the metal interconnection layers of the integrated circuits (ICs). The cluster tool has two production scale, cold-wall, horizontal single-wafer reactors in addition to the load-lock and buffer chambers and is capable to process 8 inch wafers.

A data acquisition system was built to collect the in-situ wafer temperature measured by an instrumented wafer and other process variables. Experimental results showed a temperature difference between the ULVAC system wafer temperature readings and the thermocouple wafer measurements as large as 150 ^{o}C during a process cycle in the I/O manual operation mode (see Figure 1.1).

Instead of attempting to model the overall behavior of this system by considering all constituent physical mechanisms, the goal of this research was to develop a simplified but accurate, multi-dimensional transport model that is capable of describing the observed reactor behavior and can be used to improve the temperature control system.

To achieve quantitatively accurate predictions that can explain the true wafer

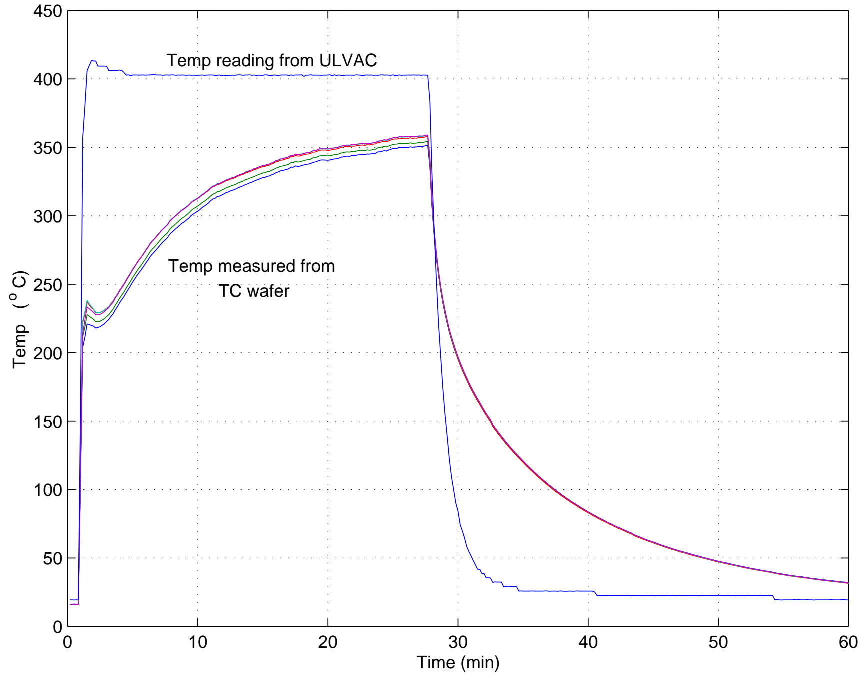

Figure 1.1: Comparison of ULVAC CVD system adjusted wafer temperature and TC instrumented wafer measurements.

temperature responses, a hybrid experimental-model simulation approach was used to explore heat transfer phenomena during the CVD process. Several sets of experiments were used to study the effects of key process parameters such as wafer temperature setpoint and reactant gas compositions on wafer temperature response, and the modeling terms were adjusted accordingly to those experimental findings. Both the steady-state and dynamic experiments were used to investigate the possible transport mechanisms because the gas phase effects such as the thermal conduction/convection at gas/wafer interface were relatively small when compared with the radiative energy transfer between the chamber components inside the reactor.

Numerical simulations were then performed to test different model structures

and the system dependent parameter values were estimated using the experimental data. If the identified parameter values did not satisfy the theoretical constraints or were found to differ significantly from the results reported in similar studies, modifications of the model were made and this experimental-model identification based model development procedure was repeated.

The weighted residual methods based on globally defined trial functions were used to solve the three-dimensional gas flow and temperature field modeling equations. The MWRtools, a MATLAB based toolbox that collects the common numerical computing elements to form a one-to-one correspondence with the methods of weighted residual solution steps, was developed and implemented for both numerical simulation and parameter estimation.

Scope and Contributions

In summary, the scope and original contributions of this thesis research are listed as follows,

1. A systematic approach combining experimental and numerical simulation methods to build a chemical vapor reactor transport model was developed;

2. To facilitate the experimental studies, a data acquisition system was built to collect in-situ wafer temperature and other process information;

3. A method to estimate system dependent heat transfer parameters was established and the identified parameter values were validated with published data and transport model simulation results;

4. The most important energy transport mechanisms were identified through different experimental designs and numerical simulations;

5. The method of weighted residuals based on global basis functions was applied to the CVD simulations as an alternative to FEM, FVM, and FDM methods. The simplicity of the global projection methods allowed researchers to focus on identifying the most important heat transfer modes;

6. A dynamic wafer temperature simulator was built that uses only the lamp power control signals to predict the wafer temperature trajectory. The simulator was tested on different process recipes and showed good agreements with the experimental data.

Organization of the dissertation

This thesis is organized as follows.

Chapter 2 The chemical vapor deposition mechanisms and the tungsten CVD kinetic model are introduced. The ULVAC CVD system as well as its operation procedure and control structure is also presented. The CVD modeling literature is reviewed and the formulation of the transport model developed in this research is addressed.

Chapter 3 The data acquisition system built for the ULVAC CVD system is described and experimental results of the wafer temperature responses to different process parameters are presented.

Chapter 4 Mathematical preliminaries for solving the modeling equations and estimating the parameter values from experimental data are provided. A

brief review of the MWRtools is also given.

Chapter 5 Simulation results of steady-state gas flow and temperature fields are provided. Predictions of the wafer temperature response to different gas compositions and wafer temperature dynamics are presented and compared with experimental results.

Chapter 6 The thesis research contributions are concluded and the future research opportunities that can be built on this work are suggested.

Chapter 2

Chemical Vapor Deposition Reactor Mathematical Modeling

This chapter addresses the problem of developing a high-fidelity, three-dimensional transport model for predicting the equipment process status of a commercial cold-wall, single-wafer CVD reactor used for depositing thin tungsten films on silicon wafer. This problem is studied as a joint project between Dr. Raymond A. Adomaitis of the Department of Chemical Engineering and Institute for Systems Research (ISR) and Drs. Gary W. Rubloff and John N. Kidder, Jr. of the Department of Materials and Nuclear Engineering and ISR, at the University of Maryland, College Park. The overall project objective is modeling and control applications of the ULVAC ERA-1000 selective tungsten CVD cluster tool.

The fundamentals of chemical vapor deposition are introduced in Section 2.1 with special emphasis on the single-wafer rapid thermal CVD process. Tungsten CVD reaction kinetics and deposition rate expression are also presented. The overview of the general transport modeling of CVD systems is then given in Section 2.2 followed by the descriptions of the ULVAC tungsten CVD reactor in

Section 2.3. The overall process equipment model for ULVAC system is detailed in Section 2.4, including the correlations used for computing the material thermal and transport properties. In Section 2.5, the dimensionless form of the modeling equations are developed.

2.1 Fundamentals of Chemical Vapor Deposition Processes

In chemical deposition processes, thin films are formed on a substrate from the gas phase by chemical reactions. Vapor reactants are fed into the reactor chamber at a controlled composition and the reactions are initiated after receiving sufficient energy from thermal, plasma, or other energy sources. Because the involvement of the chemical reactions, CVD processes are distinguished from other physical deposition methods such as sputtering, sublimation, and evaporation.

From a chemical engineering point of view, a CVD process involves the combination of fluid transport phenomena and chemical reaction kinetic mechanisms, especially in the gas phase near the gas/wafer interface and on the wafer surface. The major transport and reaction sequences during a deposition process are summarized in the following steps,

1. Convective and diffusive transport of reactants, reactive intermediates, and/or byproducts from bulk gas phase to the gas boundary layer near the wafer surface;

2. Convective and diffusive transport bringing gas species from the gas phase boundary layer to the wafer surface;

3. Adsorption and/or chemisorption of those species on the wafer surface, often after some migration on the surface;

4. Heterogeneous surface reactions to form the desired thin films, primarily initiated by the high wafer temperature;

5. Desorption of the gas phase products;

6. Convective and diffusive transport of gaseous products from wafer surface to gas boundary layer and then from boundary layer to bulk gas phase.

Due to the wide variety of deposited materials (conductors, insulators, and semiconductors) and thin film requirements (conformality, planarization, and high growth rate), many different types of CVD reactors and processes have been developed. For example, the reactor operating pressure ranges from one atmosphere (APCVD) to ultra high vacuum conditions (10^{-9} Torr) in UHV/CVD; likewise, the deposition temperature measures from 250 ^{o}C for plasma enhanced deposition (PECVD) of silicon nitride passivation layers to 1100 ^{o}C for epitaxial silicon films [19]. Other issues, such as particle contamination and throughput requirements also change the reactor design from hot-wall to cold-wall, and batch to single wafer CVD reactors, respectively. However, as larger wafer size and the more stringent fabrication demands are continuously implemented to improve profits and provide faster IC chips, the manufacturing technology shifts towards using single-wafer cluster tools that have the ability to reduce thermal budget. The single-wafer rapid thermal processing (RTP) technology is particularly suitable for those purposes and is increasingly accepted and used in the semiconductor manufacturing industry. The research presented in this thesis focuses on a commercial lamp-heating, single wafer chemical vapor deposition system which makes it similar to a rapid thermal CVD (RTCVD) reactor, thus it is useful to review the RTP processes. Additional information on the RTP pro-

cesses can be found in the next section; a general overview of the CVD processes can be found in Sherman [20] and Sivaram [21].

2.1.1 Rapid Thermal Chemical Vapor Deposition

A rapid thermal chemical vapor deposition reactor employing a single wafer technique (SWT) generally uses a smaller deposition chamber designed to achieve a short residence time of the process gases. The SWT also introduces the possibility of sequential processing such as annealing, oxidation, and deposition in the same reactor, or in connected multiple processing chambers (a cluster tool) where the wafer can be transferred between chambers in a modest vacuum environment [22]. In order to compete with the throughput of conventional multi-wafer reactor systems, RTP systems use radiant lamp heating with reactor designs of stainless steel or aluminum chamber walls that reflect the optical radiation for wafer illumination and high heating rates. Combining the SWT technique and the cold-wall, low-pressure operating conditions, the contamination problem encountered in batch CVD processes are largely reduced in RTP reactors.

Several equipment and process control issues are actively studied in RTCVD systems. A number of challenging aspects of these problems can be analyzed from a modeling point: for example, the cold wall process exhibits strong thermal gradients within the gas phase that can lead to significant changes in flow patterns, mass transfer rates, and gas mixture physical properties. Moreover, due to the radiation heat transfer domination in RTP reactors, the wafer pattern and surface roughness can result in different emissivities across the wafer and change the deposited film thickness significantly [23]. The lack of proven in-situ, real-time temperature and film thickness measurement technologies [24] makes

the wafer temperature control more complex and difficult. Further details of these equipment and control issues can be found in Chapter 4 of Chang and Sze [19] and other references [25, 26, 27, 28].

2.1.2 Tungsten Chemical Vapor Deposition

The metalization, depositing and patterning of metal films, has become a critical aspect of semiconductor technology as larger chip size and higher packing density are used to manufacturing advanced integrated circuits (ICs). The interconnect metal layers provide long-distance electrical transport between the active areas of the chip and the communication with the outside world. The materials used in metalization (e.g., metals, contact diffusion barrier) thus should have low resistivity to permit high speed and limited power dissipation, good adherence to underlying materials such as silicon, non-reactive to the adjacent films or oxidizing ambient, and be stable enough that can withstand the following process steps of high-temperature treatments or chemically reactive environments. Tungsten, due to its favorable properties, is selected over the aluminum as the material to fill the contact holes, connecting the source or drain regions of transistors and interconnect layer, or via holes which connect multilevel interconnection layers.

Tungsten has another major advantage over the other materials in the available deposition technique. Tungsten CVD uses a relative low process temperature so it will not degrade the previously formed device and provides good step coverage of the contact or via holes. The deposition rate of tungsten CVD is also fast enough to be economically feasible in industry.

2.1.3 Tungsten Chemical Vapor Deposition Chemical Mechanisms

Deposition of tungsten films on silicon surface can be achieved either through hydrogen (H_2) or silane (SiH_4) reduction of tungsten hexafluoride (WF_6). By depositing a metal nucleation layer such as TiN on the entire wafer, tungsten can be blanket-deposited on the wafer and contact or via holes using a hydrogen reduction pathway at the temperature range 400-500 ^oC [19, 29]. This process has the advantages of achieving high step coverage and good across-wafer conformality. Subsequent etch-back steps using chemical-mechanical polishing (CMP) or reactive ion eatching (RIE) are required for planarization to ensure good interconnect metal (Cu, Al) step coverage [19].

Tungsten can also been deposited selectively using the silane reduction of WF_6, where W is deposited on Si surface and not on SiO_2 insulator layer due to the reactivity difference at wafer temperature lower than 400 ^oC [19]. This deposition process does not require any metal liner such as TiN or TiW, or etch back steps for the plug processes [29]. However, the selectivity loss due to spurious nucleation and the following W growth on SiO_2 surface, as well as the difficulty to fill holes with different depths within the wafer, are still major issues continuously under study [19, 29].

Currently, a combination of these two processes is used in industry for contact or via hole filling. Silane is initially introduced without any flow of WF_6 to initiate the deposition of a very thin Si pre-nucleation layer, followed by a SiH_4 + WF_6 silane reduction nucleation process and then the high-rate H_2 + WF_6 hydrogen reduction deposition to fill via or contact holes. CMP steps are used afterward for global planarization [19]. An excellent review of the materials and processing parameters for the tungsten plug processes can be found in Ireland

[30].

Hydrogen Reduction of WF_6

In the hydrogen reduction reaction pathway currently used in the research in the ULVAC CVD system at the University of Maryland [31], the wafer silicon surface provides the initial nucleation layer for the formation of W seed layer,

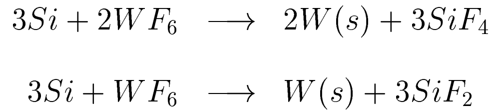

$$\begin{aligned} 3Si + 2WF_6 &\longrightarrow 2W(s) + 3SiF_4 \\ 3Si + WF_6 &\longrightarrow W(s) + 3SiF_2 \end{aligned}$$

and

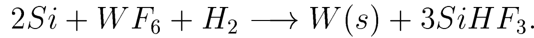

$$2Si + WF_6 + H_2 \longrightarrow W(s) + 3SiHF_3.$$

This W seed layer provides the active sites for the H_2 reduction of the WF_6 through adsorption and removal of F-atom from the surface in the form of volatile HF product,

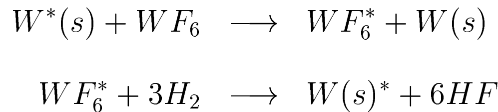

$$\begin{aligned} W^*(s) + WF_6 &\longrightarrow WF_6^* + W(s) \\ WF_6^* + 3H_2 &\longrightarrow W(s)^* + 6HF \end{aligned}$$

where * denotes the activated surface sites.

The hydrogen reduction process is usually performed at process conditions of 400-500 ^{o}C and 0.1-80 $Torr$ total pressure [32]. In the chemical reaction kinetics rate-limited operation region, used in most industrial deposition processes due to the superior conformality produced under these conditions, the deposition rate shows square root dependence on H_2 partial pressure and zero-order dependence on WF_6 partial pressure [29, 32]. The empirical rate expression can be expressed as

$$R_{H_2} = k_0 P_{H_2}^{0.5} P_{WF_6}^{0} exp\left(\frac{-Ea}{RT}\right) \quad (2.1)$$

where k_0 is the frequency coefficient, P_{H_2} and P_{WF_6} are the partial pressure of each species, Ea is the activation energy and R is the gas constant. Kleijn et. al. [17] showed that the assumption of a zero order dependence on WF_6 partial pressure is still valid even when the WF_6 partial pressure is as low as 7.5×10^{-3} $Torr$. The reported activation energy varies from 69 to 73 kJ/mole in the temperature and pressure ranges of 270 to 470 ^{o}C and 0.2 to 10 $Torr$ [33, 34], respectively.

Silane Reduction of WF_6

The silane reduction process [19, 29, 35] starts with silicon reduction step caused by WF_6,

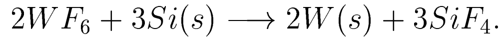

$$2WF_6 + 3Si(s) \longrightarrow 2W(s) + 3SiF_4.$$

This reaction is self-limited in that it stops when the atomic silicon disappears from the wafer surface. Two competing kinetic mechanisms are found at common deposition conditions (150 to 300 ^{o}C and 40 to 50 $Torr$):

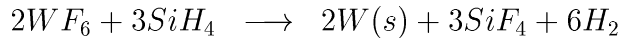

$$\begin{aligned} 2WF_6 + 3SiH_4 &\longrightarrow 2W(s) + 3SiF_4 + 6H_2 \\ WF_6 + 2SiH_4 &\longrightarrow W(s) + 2SiHF_3 + 3H_2. \end{aligned}$$

In the range of deposition temperatures of 145 to 395 ^{o}C, Ammerlaan [32] reports non-linear Arrhenius plots of the silane reduction process with the maximum rates observed near 300 ^{o}C. The author also finds the kinetics are determined by the partial pressure ratio of silane and tungsten hexaflouride P_{SiH_4}/P_{WF_6}:

- For $P_{SiH_4}/P_{WF_6} < 0.3$, a first-order dependence in silane partial pressure P_{SiH_4} and a small negative order dependence in tungsten hexaflouride par-

tial pressure P_{WF_6} are found giving

$$R_{SiH_4} = k_1 P_{SiH_4}^{1.06} P_{WF_6}^{-0.16} P_{H_2}^{0} exp\left(\frac{-Ea}{RT}\right).$$

- For $0.5 < P_{SiH_4}/P_{WF_6} < 1$, the dependence changes to almost second order in P_{SiH_4} and minus first-order in P_{WF_6}, giving

$$R_{SiH_4} = k_2 P_{SiH_4}^{1.80} P_{WF_6}^{-0.94} P_{H_2}^{0} exp\left(\frac{-Ea}{RT}\right).$$

Other researchers [36, 37] did not investigate the ratio of partial pressures and reported rate expression model with a first-order in the silane partial pressure P_{SiH_4} and a zero or negative order in the tungsten hexaflouride partial pressure P_{WF_6}. However, measured activation energy values range between 8 and 50 kJ/mole [36, 37] from different reports.

2.2 Mathematical Modeling Overview of CVD Systems

In this section, we will discuss the necessary modeling components and solution steps for developing a complete CVD equipment-process model, and will give a short survey of the published CVD equipment modeling studies. In the subsequent subsection, use of the currently available commercial computational fluid dynamic (CFD) software suitable for CVD modeling is discussed. An overview of the general transport equations of the gas phase and wafer for single wafer systems will be described in the following subsections. The other simulation components such as physical properties and a chamber heating model, will be discussed in Section 2.4. Further simplifications of the transport equations and the appropriate boundary conditions for the ULVAC W CVD reactor modeling are also addressed in Section 2.4.

2.2.1 CVD Transport Modeling

A general chemical vapor deposition simulation model has several building blocks as illustrated in Figure 2.1. Generally, the details of the reactor geometry and dimensions as well as processing conditions such as inlet gas flow rates, wafer temperature setpoints, chamber pressure, and heating lamp output efficiency are model input parameters. Simulator predictions such as the gas velocity and temperature profiles, across-wafer temperature contours, wafer temperature trajectory, chemical species concentration distribution, deposition rate, and deposited film uniformity are outputs of the model.

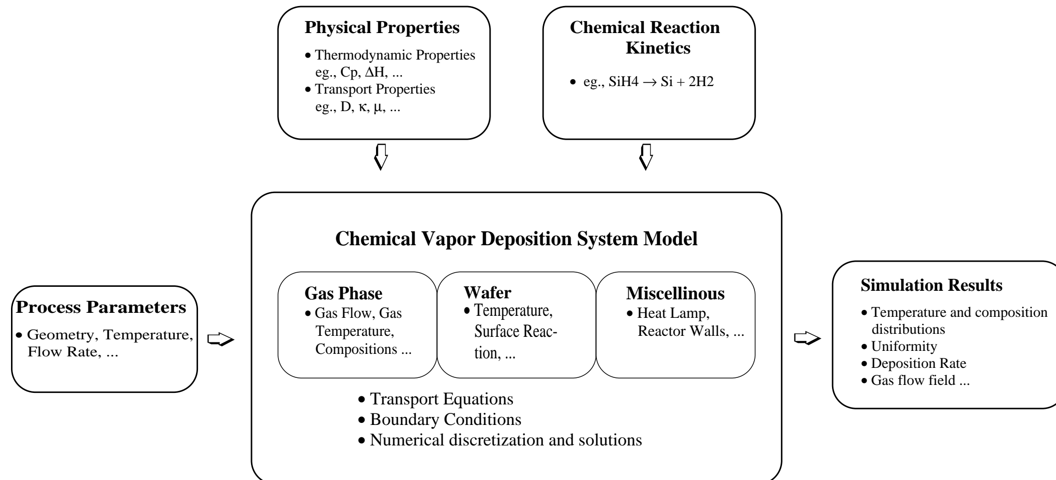

Figure 2.1: Schematic illustration of modeling approach.

The core system model usually consists three submodels describing the transport phenomena in gas phase, wafer, and the other components in the reactor chamber. Conservation equation of mass, momentum, and energy [38] provide sets of coupled partial differential equations describing the interacting transport processes among the three submodels subject to appropriate boundary conditions. Physical properties including thermodynamic and transport properties

of the gases, wafer, and other chamber materials, as well as chemical reaction kinetics from either empirical experiments or computational chemistry predictions, are two supplementary blocks that interact with the governing equations providing parameter values for model computations.

At the beginning of the simulation, a mesh generation program should be called to construct the computational domains from the true physical system domains. The governing equations of different submodels are then discretized on the computation domains using a weighted residual projection method. The sets of equations must be solved simultaneously due to the interactive transfer mechanisms between submodels and the continuous boundary conditions across adjacent domains. The physical properties that strongly depend on the state variables should be updated simultaneously during the computation process.

2.2.2 Literature Review

CVD reactor transport modeling began to receive broad attention in the early 1980s when researchers used the simulation results to study the transport mechanisms in the reactors and performed numerical experiments to evaluate different reactor designs [39, 40]. Detailed CVD reactor models are developed by generalizing the transport equations to account for multiple dimensions, transient effects, multiple mass and energy transport mechanisms, and chemical reactions. The relative importance between different physical phenomena varies among different types of CVD reactors and processing modes. Middleman and Hochberg [41] give a comprehensive introduction of the CVD modeling for different type of reactors from a chemical engineering viewpoint; Kleijn and Werner [9, 42] provide a general guideline for a CVD transport modeling procedure; Badgwell

et. al. [11] and Jensen et. al. [10], as well as Kleijn [9] all give excellent reviews for the papers studying the CVD modeling problems. In this literature review section, the entire spectrum of CVD modeling research will not be covered; only the portion helpful in developing the modeling work for ULVAC system will be discussed.

APCVD Reactor Modeling

Most initial efforts of CVD modeling focused on the atmosphere pressure deposition tools (APCVD), which were mainly used for expitaxial deposition in horizontal rectangular chambers. Moffat and Jensen [16, 40] studied the transport models for horizontal, cold-wall GaAs metalorganic CVD (MOCVD) and silicon epitaxial APCVD reactors. The models were based on steady-state mass, energy, and momentum balances in three dimensions, and was simplified by a 2D boundary layer approximation for the case where secondary flow is not important. The finite-element method was used to discretized the governing equations. The major conclusion of their work was that buoyancy driven transverse convection cells, due to the large temperature gradients near the cold chamber walls, significantly altered the deposition process. The later papers by Jensen and coworkers (Fotiadis et. al. [43, 44], Jensen [45]) experimentally verified the gas flow and temperature fields and the generation of recirculation cells using Raman scattering temperature measurement technology and smoke trace method. They also extended the three-dimensional, steady-state modeling approach to a vertical MOCVD reactor, and experimented with reactor design parameters to conclude that increasing the inlet gas flow rate, rotating the susceptor, reducing the pressure, and modifying the reactor shape can help to suppress the natural

convection flows.

Similar simulation results of the natural convection effects were also found by other researchers. Ingle and Mountziaris [46] developed a finite element discretized two-dimensional flow and heat transfer model of a horizontal MOCVD reactor, and identified the operating conditions where the transverse buoyancy-driven flow existed when H_2 or N_2 gas was used. Their predictions were in good agreement with the experimental values obtained from Chiu and Rosenberger [47, 48]. In another paper, Mountziaris et. al. [49] extended the modeling framework by adding reactant species mass balance equations and a detailed gas phase as well as surface reaction kinetic models to predict the GaAs deposition rate. Optimal operating conditions were found to maximize the thin film growth uniformity and precursor utilization.

Holstein and Fitzjohn [50] studied the conditions for the formation of buoyancy driven secondary flows in the forms of transverse recirculation, longitudinal rolls, and traveling waves in a channel MOCVD reactor used for growing InP. They performed simulations on a Galerkin finite element method solving two-dimensional, steady-state model having the capability to predict the gas flow and temperature fields as well as the film deposition rate. By changing the gravity in the modeling equations, they investigated the reactor performance in both horizontal and vertical orientations and categorized the operating conditions resulting in different types of secondary flows in terms of the Rayleigh number (Ra), Reynolds number (Re) and Grashof number (Gr), and their ratios Gr/Re and Gr/Re^2. Evans and Greif [51] presented the transient solutions of the two-dimensional flow equations for a similar reactor geometry, showing the occurrence of transversal rolls leading to time-periodic, “snaking” motion of the

gas that enhanced the heat transfer.

In another paper, Evans and Greif [52] modeled the three-dimensional flow and temperature fields of a vertical rotating disk CVD reactor. The coupled partial differential governing equations were solved with central/upwind finite difference method. They reported the formation of forced convection flows was determined by the value of a mixed dimensionless convection parameter $\mathrm{Gr}/\mathrm{Re}_\omega^{3/2}$ where $\mathrm{Re}_\omega = \rho\omega D^2/\mu$ was the rotation Reynolds number with susceptor diameter D and rotation speed ω. If the $\mathrm{Gr}/\mathrm{Re}_\omega^{3/2}$ was smaller than 3, the flow field was dominated by the rotation-induced forced convection. When the $\mathrm{Gr}/\mathrm{Re}_\omega^{3/2}$ value was larger than 3, strong natural convection flow induced recirculations were observed.

A horizontal APCVD reactor with rotating disk was studied by Habuka and coworkers [53, 54]. The governing equations for gas velocity, temperature, and chemical species transport were solved with finite-difference scheme in three dimensions. Unlike the vertical reactors with high rotating speed designed to have a simple gas stream and a rather homogeneous species distribution, they found an asymmetric and nonuniform gaseous reactant distribution profile in the region above the wafer due to thermal diffusion and reactant consumption despite the wafer rotation induced gas circulation. However, good film thickness was observed in both simulation and experimental studies and was attributed to the averaging effect of wafer rotation.

LPCVD Reactor Modeling

Horizontal low pressure CVD (LPCVD) reactors have been used to deposit polysilicon films, and the hot-wall multi-wafer reactor designs have demonstrated

homogeneous temperature distribution in the furnace tube. Jensen and Graves [55] used a one-dimensional description for the diffusive transport and deposition between the wafers, neglecting convective effect and axial temperature gradients. This inter-wafer model was used with another one-dimensional model to describe the convection-diffusion phenomena for the annular region. Badgwell et. al. [56] performed a series of in-situ wafer temperature measurements that confirmed the radiant mechanisms were the most important heat transfer mode while the gas phase conduction and convection can be neglected in LPCVD operating conditions. In a paper published later [57], they extended Jensen and Graves's work by adding the mass balance for the reactant gas phase and a radiation heat transfer model. This equipment model was solved by orthogonal collocation on finite-element meshes and was used to optimize the processing recipe.

Kuijlaars and coworkers [58] studied the multi-component diffusion phenomena in a LPCVD reactor similar to Jensen and Graves's. They used Fisk's law for binary diffusion in a bulk carrier gas to approximate the multi-component diffusion fluxes, and concluded that the Fick's law approximation should not be used in LPCVD modeling if the reactant and reaction-product species were not sufficiently diluted or there was a large difference in the reactant molar mass.

RTCVD Reactor Modeling

Rapid Thermal chemical vapor deposition (RTCVD) has been used for various thermal processing applications including polysilicon, tungsten, and thin dielectric deposition as well as selective epitaxial growth. A large volume of literature can be found for RTCVD modeling due to the difficulties in temperature and uniformity control during the development of the RTP technology.

The first comprehensive modeling studies were those by Kleijn and coworkers [17, 42, 59, 60, 61, 62] and Werner and coworkers [63, 64]. Kleijn et. al. initially studied blanket tungsten deposition from WH_6 and H_2 in a cold-wall, single-wafer LPCVD reactor [17]. The two-dimensional axisymmetric model was solved by a finite-volume method to predict the gas flow, heat transfer, species transport, and chemical reactions. Their results showed a transition from uniform, kinetically limited growth to nonuniform transport limited growth at decreasing WH_6 inlet concentrations. They also found that thermal diffusion in the reactor leads to large concentration gradients and a strong depletion of WH_6 at the wafer/gas interface. The same model later was used to study the effect of micro-loading and macro-loading on growth rates in the selective tungsten growth from WH_6 and SiH_4 [59]. Werner and coworkers [63] use the PHOENICS computational fluid dynamics (CFD) software to solve a two-dimensional mass and heat transfer model with a detailed surface reaction model for selective tungsten deposition. Their simulation results also showed that thermal diffusion was very important in such a cold-wall low-pressure systems and proposed two selectivity loss models that featured the formation of SiF_y and WF_x intermediates. Simulations were also used to study the reactor design for optimal selectivity.

Pollard and coworkers [65, 66] developed a simultaneous reaction kinetics and steady-state transport model for tungsten deposition using WH_6 and H_2 in a LPCVD reactor. Their model included 8 gas phase reactions and 65 surface reaction steps and used statistical thermodynamics, transition state theory, and bond dissociation enthalpies to determine the reaction rate constants without fitting any parameters. Good agreements with experimental data were reported; they found the process was controlled by surface kinetics while the gas phase

reactions were unimportant. The major reaction pathways and the rate-limiting steps were also identified and used to develop the simplified rate expression. Kleijn and coworkers [60, 61, 62] later adopted Pollard's kinetic model in their two-dimensional transport phenomena simulations using a commercial CFD software PHOENICS-CVD to study the reaction intermediates and the optimization of selective processes.

In a series studies, Jensen and coworkers [10, 67, 68, 69, 23] presented a systematic approach for simulating the rapid thermal processes. Their model was based on a axisymmetric RTCVD reactor and the wafer temperature trajectory was predicted. The major contribution of their work was the incorporation of the numerical computation methods for radiant heat transfer between lamps, substrates, reflectors, and system walls. The finite element and/or the Monte Carlo (MC) methods were used to compute the view factors between radiation components exchanging radiant energy and the temperature dependent material radiative properties during the dynamic simulations. Quantum chemistry based computational chemistry models solved by Monte Carlo simulations were also included in the modeling framework to predict reaction kinetic parameters in an effort to study processes without proven kinetic models. In the most recent paper [23], a thin film optics model was included to predict the effect of patterns on the wafer radiative properties; the resulting temperature distributions were used to predict the film stress and deformation.

The University of Texas, Austin research group led by Edgar and Trachtenberg studied a polysilicon CVD reactor using a two-dimensional transport model discretized by a finite-difference method [8, 70, 71, 72]. The main goal of their studies was to identify the dominant factors governing the heat transfer and fluid

flow using various levels of simplification on the modeling equations. They found the gas-phase reactions can be neglected in predicting the polysilicon deposition rate [71] and developed an empirical rate expression for the conversion of silane to solid silicon from experimental data.

Kailath led a Stanford research group that modeled the wafer temperature trajectory and uniformity in a polysilicon RTCVD reactor [73, 74, 75, 76, 7, 77, 78, 79]. Unlike Jensen's approach, they used an explicit method for computing the view factors in a simplified reactor geometry. However, their model did not consider the gas flow field and thermal diffusion, nor did include reactions that were induced by the wafer surface property variations, however, their model predictions were in good agreement with experimental wafer temperature data obtained in non-reacting gases. They also developed the semi-empirical heat transfer model by identifying several key parameters such as process time constant, view factors, and heat transfer coefficient at the wafer/gas interface [74, 7]; a black-box linear model also was identified from process input-output data [75]. Their goal was to develop model-based control algorithms for lamp design and power control to achieve uniform heat flux across the wafer.

Feature-Scale Modeling

All of the above modeling studies considered equipment models that focused on the macroscopic transport phenomena of the systems. With decreasing feature dimensions in microelectronic devices, feature-scale models with the ability to predict the conformality is useful for determining optimal process conditions. Hasper and coworkers [2, 80] and Thiart and Hlavacek [81] developed continuum-like diffusion-reaction models (DRM) based on simultaneous free molecular dif-

fusion and heterogeneous surface reactions. However, the DRM models needed simple and known kinetic models such as those developed by Pollard et. al. [65, 66]; the predictions only qualitatively agreed with the experimental observation [82].

An analytical model based on a hemispherical vapor source was reported by Yun and Rhee [83]. Their model computed the particle arriving angle and the re-emission effect, thus largely reducing the computational resources required for the MC solution, but only qualitative comparison was made in their paper. Cale et. al. [15, 14] developed ballistic transport and reaction models (BTRM) to predict the step coverage in feature holes. Monte Carlo simulation methods were used to solve the direct and re-emitted deposition processes subject to feature geometrical effects. The impact of the processing conditions on step coverage was explained in relation to reactive sticking coefficient, the fraction of the total incident particles that stick on the surface. Quantitative agreement between prediction and experiment was reported when the deposition conditions are accurately known [82].

Multi-scale Modeling

Cale and coworkers [84] and Jensen and coworkers [85] both reported integrated modeling approaches that combine the macroscopic flow and transport phenomena and feature-scale step coverage simulations. The multi-scale integration difficulties resulted from the length scale differences, from centimeters to microns. In both reports, finite element solution procedures were used for macroscopic transport equations and MC methods were used to predict the feature conformality in BTRM models. To interface the computation between two scales, Cale

introduced an intermediate scale using local refinement on finite element meshes in the vicinity of the features, and Jensen introduced an effective reactivity function that determined the average number and nature of the molecules entering the substrate surface from macroscopic scale.

2.2.3 CVD Modeling Using Commercial CFD Software

Commercially available computational fluid dynamics software packages provide powerful and flexible solution platforms of the multidimensional transport equations developed for the CVD models. To deal with the complex reactor geometries and the specific set of chemical reactions, these packages offer finite volume (FLUENT, PHOENICS-CVD) or finite element methods, three dimensional grid generation functions and special material properties as well as chemical kinetics models for the CVD simulations. To set up problems and conduct simulations without detailed knowledge of fluid dynamics and computational techniques, these packages feature a user interface layer for the simulation input/output purposes. This interface allows all the numerical computations to be processed in the background, however, there are drawbacks for such approach since it is often difficult to use the CFD code in model reduction, control, or other specialized applications [9, 86].

2.2.4 General Modeling Assumptions

Kleijn indicated in [9] that there are several general assumptions can be made to simplify the complexity of the transport modeling problem and the solution computational effort needed for typical chemical vapor deposition processes:

1. Gas mixtures usually can be treated as a continuum. This assumption is valid when the mean free path length (λ) of the gas molecules is much smaller than the typical characteristic dimension of the reactor (L), i.e., the Knudsen number $Kn = \lambda/L < 0.01$.

2. At pressure and temperature conditions commonly used in CVD processes, the gas can be treated as ideal gas that satisfies the ideal gas law and Newton's law of viscosity.

3. The gas flow is in the laminar region.

4. The gas mixture is transparent to heat radiation.

5. The wafer is round (no chord).

6. The wafer is relatively thin that there is no temperature gradient across the wafer thickness.

A number of characteristic dimensionless groups, appearing in the transport equations by scaling all variables with reference values, are used to characterize the general features of CVD processes. Each dimensionless group can be interpreted as the ratio of the magnitudes of two physical mechanisms and can be used to estimate the importance of different physical phenomena in a particular process, or to check the possible scale-up effects. Typical values of the dimensionless groups as well as their physical interpretations are summarized in Table 2.1 [9, 45, 87] for low pressure chemical vapor deposition (LPCVD) processes. The definitions and values of typical process in ULVAC W CVD will be given and further discussed in Section 2.5.

Table 2.1: Important dimensionless groups and their typical range in low pressure CVD (LPCVD) reactors.

Dimensionless Groups	Physical Interpretation	Value
Renolds (Re)	$\frac{\text{Interial forces}}{\text{Viscous forces}}$	10^{-2} - 10^{2}
Grashof (Gr)	$\frac{\text{Bouyancy forces}}{\text{Viscous forces}}$	0-10
Prandtl (Pr)	$\frac{\text{Momentum diffusivity}}{\text{Thermal diffusivity}}$	0.7
Rayleight (Ra)	$\frac{\text{Bouyancy forces}}{\text{Viscous forces}}$	1-10^{5}
Peclet (thermal) (Pe_T)	$\frac{\text{Convective heat transfer}}{\text{Conductive heat transfer}}$	10^{-2} - 10^{2}
Peclet (mass) (Pe_M)	$\frac{\text{Convective mass transfer}}{\text{Conductive mass transfer}}$	10^{-2} - 10^{3}
Schmidt (Sc)	$\frac{\text{Momentum diffusivity}}{\text{Species diffusivity}}$	1-10
Knudsen (Kn)	$\frac{\text{Mean free path length}}{\text{Typical dimension}}$	10^{-3} - 10^{-2}
Surface Damkohler (Da)	$\frac{\text{Chemical reaction rate}}{\text{Diffusion rate}}$	10^{-3} - 10^{3}

2.2.5 Gas Phase Transport Model

Under the general assumptions listed in previous subsection, the gas flow in the CVD chamber is described by the equation of continuity and the momentum balance equations following the classic textbook by Bird et al. [38],

$$\frac{\partial \rho}{\partial t} + \nabla \cdot (\rho \mathbf{v}) = 0 \tag{2.2}$$

$$\frac{\partial (\rho \mathbf{v})}{\partial t} + \nabla \cdot (\rho \mathbf{v}\mathbf{v}) - \nabla \cdot [\mu(\nabla \mathbf{v} + (\nabla \mathbf{v})^T) - \frac{2}{3}\mu(\nabla \cdot \mathbf{v})\mathbf{I}] + \nabla P + \rho \mathbf{g} = 0 \tag{2.3}$$

where T is gas temperature, ρ is gas density, t is time, μ is gas viscosity, $\mathbf{I}$ is identity matrix, $\mathbf{v}$ is gas velocity, P is pressure, $\mathbf{g}$ is gravity. The first three

terms in the momentum balance equation (2.3) describe the transients in the flow, the inertial, and viscous forces, respectively. The last two terms account for the pressure and gravity forces. The flow equations are coupled to the energy balance equation:

$$\frac{\partial(\rho C_p T)}{\partial t} + \nabla \cdot (\rho C_p \mathbf{v} T) - \nabla \cdot (\kappa \nabla T) - \nabla \cdot \left(RT \sum_{i=1}^{N} \frac{D_i^T}{M_i} \nabla(ln f_i) \right) \\ - \sum_{i=1}^{N} \frac{H_i}{M_i} \nabla \cdot \mathbf{j}_i + \sum_{i=1}^{N} \sum_{k=1}^{K} H_i \nu_{ik} (R_k^g - R_{-k}^g) = 0. \tag{2.4}$$

Here, C_p is gas heat capacity, κ is gas thermal conductivity, R is the gas constant, D_i, M_i, f_i, H_i, and $\mathbf{j}_i$ are the diffusion coefficient, molecular weight, mole fraction, molar enthalpy, and diffusive mass flux with respect to the ith gas species, respectively. The kth gas phase reaction and its inverse reaction as well as the stoichiometric coefficient corresponding to the ith component are denoted as R_k^g, R_{-k}^g and ν_{ik}. The first term in the energy equation shows the transient temperature variation; the second and third terms describe the convection and diffusion heat transfer in gas mixture. The heat transfer resulting from concentration gradient, known as Dufour effect, and the heat flux generated by interdiffusion of chemical species are represented in the fourth and fifth terms, although they are not significant in most CVD processes. The last term represents the heat generation or lost due to the gas phase reactions.

Because the physical properties such as ρ, μ, C_p, κ, and D_i are not only functions of gas temperature and pressure, but also the functions of gas composition, the above equations thus are coupled with the species concentration equations. For the ith species, the conservation equation is

$$\frac{\partial(\rho\omega_i)}{\partial t} = -\nabla \cdot (\rho \underline{\mathbf{v}} \omega_i) - \nabla \cdot \underline{\mathbf{j}}_i + M_i \sum_{k=1}^{K} \nu_{ik} (R_k^g - R_{-k}^g) \tag{2.5}$$

with mass average velocity $\underline{\mathbf{v}}$ and diffusive mass flux $\underline{\mathbf{j}}_i$ defined as follows:

$$\underline{\mathbf{v}} = \sum_{i=1}^{N} \omega_i \, \underline{\mathbf{v}}_i$$

$$\underline{\mathbf{j}}_i = \rho \, \omega_i (\underline{\mathbf{v}}_i - \underline{\mathbf{v}})$$

where ω_i is the mass fraction and $\underline{\mathbf{v}}_i$ is the velocity vector of the ith species. In the above equation (2.5), the first term represents the transient variation in species concentration; the second and third terms describe the convective and diffusive mass transport, and the last term accounts for the generation/lost of the gaseous species from gas phase reaction.

2.2.6 Wafer Thermal Dynamics Model

The time evolution of the temperature distribution of the wafer is described by the energy balance equation:

$$\frac{\partial}{\partial t}(\rho_w C_{p_w} T_w) = \nabla \cdot (\kappa_w \nabla T_w) + \frac{\mathbf{q}_{top} + \mathbf{q}_{bot}}{Z_w} \tag{2.6}$$

where T_w is the temperature, C_{p_w} is the heat capacity, κ_w is heat conductivity, and Z_w is the thickness of the wafer. The first term in the right-hand side of the equation accounts for the conduction heat transfer and $\mathbf{q}_{top}$ and $\mathbf{q}_{bot}$ are heat fluxes coming in at the top and bottom of the corresponding components that

can be given as follows:

$$
\begin{aligned}
\mathbf{q}_{top}, \mathbf{q}_{bot} &= \mathbf{q}^{em} + \mathbf{q}^{ab} + \mathbf{q}^{conv} + \mathbf{q}^{cond} + \mathbf{q}^{rxn} \\
\mathbf{q}^{em} &= -\sum_{j=wall,sh} F_\epsilon F_A \sigma (T_w^4 - T_j^4) \\
\mathbf{q}^{ab} &= Qu\alpha_w \\
\mathbf{q}^{conv} &= -h_g(T_w - T_g) \\
\mathbf{q}^{cond} &= -\sum_{j=s,r} h_j(T_w - T_j) \\
\mathbf{q}^{rxn} &= -Z_w \sum_{i=1}^{N}\sum_{k=1}^{K} H_i \nu_{ik}(R_k - R_{-k})
\end{aligned}
$$

where $\mathbf{q}^{em}$ is radiative heat exchange from wafer to chamber wall T_{wall} or showerhead T_{sh}; $\mathbf{q}^{ab}$ is the radiative heat flux absorbed by wafer from heating lamps; $\mathbf{q}^{conv}$ is convection and conduction heat transport between gas phase T_g and wafer; $\mathbf{q}^{cond}$ is conduction heat transfer from wafer to the susceptor T_s or guard ring T_r; $\mathbf{q}^{rxn}$ is the heat transport from wafer surface heterogeneous chemical reactions. The radiative heat flux is calculated by defining the geometrical factor, or configuration factor F_A and emissivity factor F_ϵ between two gray surfaces [88, 89]. The absorptivity and Boltzmann constant are represented as α and σ, respectively.

The other components in the reactor chamber such as quartz showerhead, can be modeled in a similar approach. Chamber walls are usually modeled by considering both heat transfer mechanisms inside the chamber and the cooling effect provided outside the chamber by reactor cooling jackets. All modeling equations are subject to the system dependent boundary conditions.

2.3 ULVAC Selective Tungsten Chemical Vapor Deposition Cluster Tool

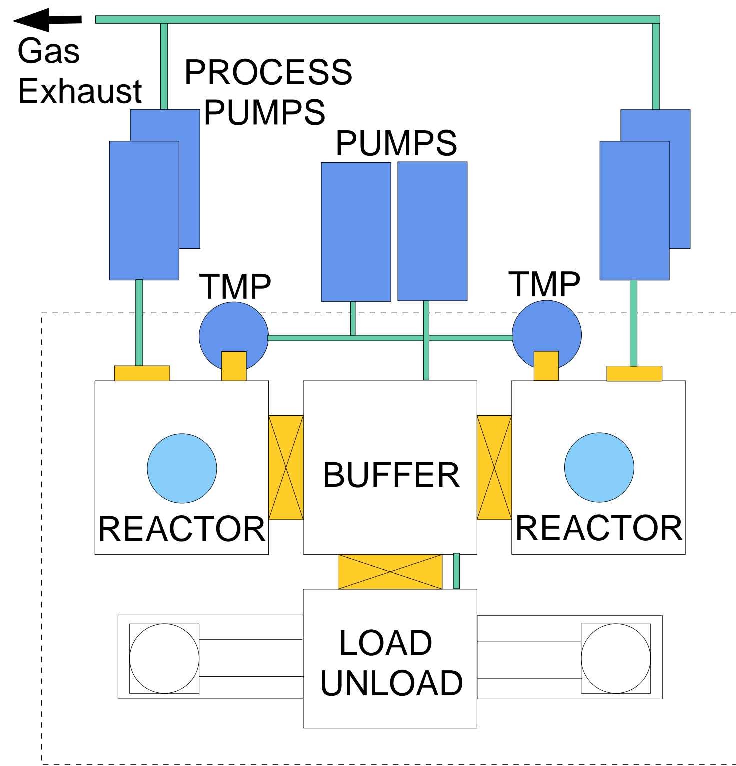

Figure 2.2: Top view schematic ULVAC cluster tool.

Our research focuses on the ULVAC ERA-1000 selective tungsten deposition cluster tool, consisting of two production-scale, cold-wall, single-wafer reactors joined by a buffer and a load-lock chamber for automatic loading and transfer of wafers. This CVD system is located at the Laboratory for Advanced Material Processing (LAMP) of the University of Maryland and an overhead view of the cluster tool is shown in Figure 2.2. Each reactor is water cooled to prevent deposition on the chamber walls and is equipped with two sets of pumps: a mechanical pump for maintaining gas flow during the processing and a turbo

molecular pump (TMP) that can bring down the pressure to as low as 10^{-7} $Torr$ for reducing water vapor or other residual contaminants while idling.

CVD Reactor Geometry

Figure 2.3 depicts the individual reactor configuration. Reactant gases are fed to the reactor from two sources: a gas mixture of silane, tungsten hexafluoride, and argon or nitrogen (if used) is injected through a two-dimensional nozzle array installed on one side wall, and hydrogen is pumped in through a transparent showerhead mounted in the top of the reactor chamber. Gases mix in the chamber and react at the surface of a wafer located at the chamber center. For convenience we use 4 inch diameter wafers, although the tool is capable of processing 8 inch wafers. The wafer is supported by a slowly rotating 4 inch diameter quartz susceptor to assure the azimuthal symmetry of the deposited film. An incoherent tungsten-halogen lamp ring above and outside the reactor chamber is used to heat the wafer to desired temperature through the transparent quartz showerhead window. Typical deposition runtimes last 5 minutes after operating temperature is reached.

Process Operating Procedure

The general operation procedure and control structure of the reactor is illustrated in Figure 2.4. An editable multi-step operating recipe, defining the processing sequence including the choice of reactant gases, gas flow rates, chamber pressure, and wafer temperature setpoints, is setup first by touching the ULVAC system control screen prior to the processing. An integrated system controller receives the status signals from several sensors and adjusts the operating parameters

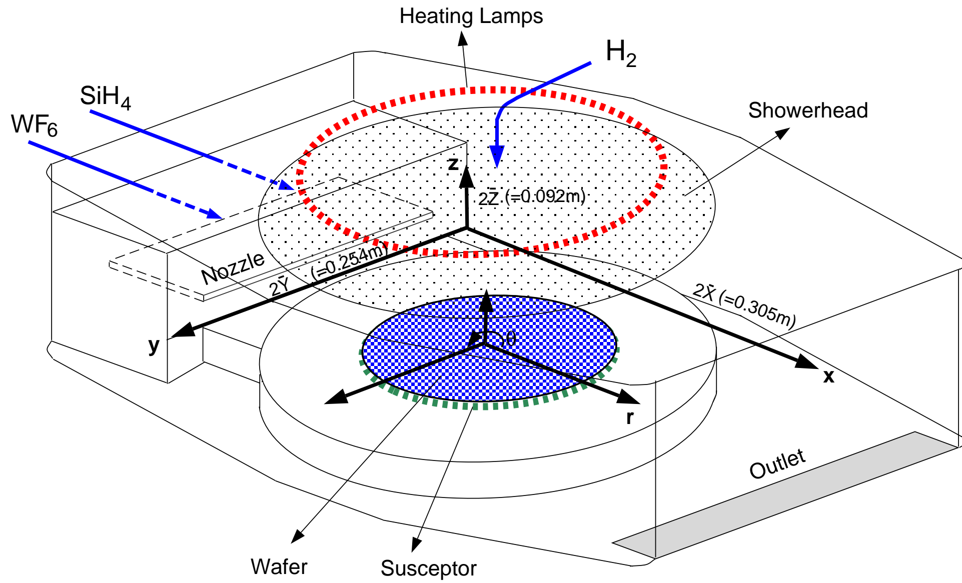

Figure 2.3: Sketch of the Tungsten CVD reactor system.

(pressure, temperature, reactant flow rates, and duration of each step) preset by the recipe through the corresponding controllers.

The equipment setting parameters such as wafer temperature PID controller parameters and wafer rotation speed can also be adjusted from hardware setting by the process engineers. However, in contrast to the recipe inputs, these equipment settings are usually not changed for each different process recipes.

Reactor Wafer Temperature Control System

Because the system thermocouple is located outside the reactor chamber near the lamp ring, it receives most of the radiation energy from the lamp directly and measures the temperature in atmosphere pressure. The equipment manufacturer uses a predetermined look-up table, considering the effects resulting from lower chamber pressure and different gas flow rates, to predict the wafer temperature under the process conditions. Part of the look-up table wafer temperature ad-

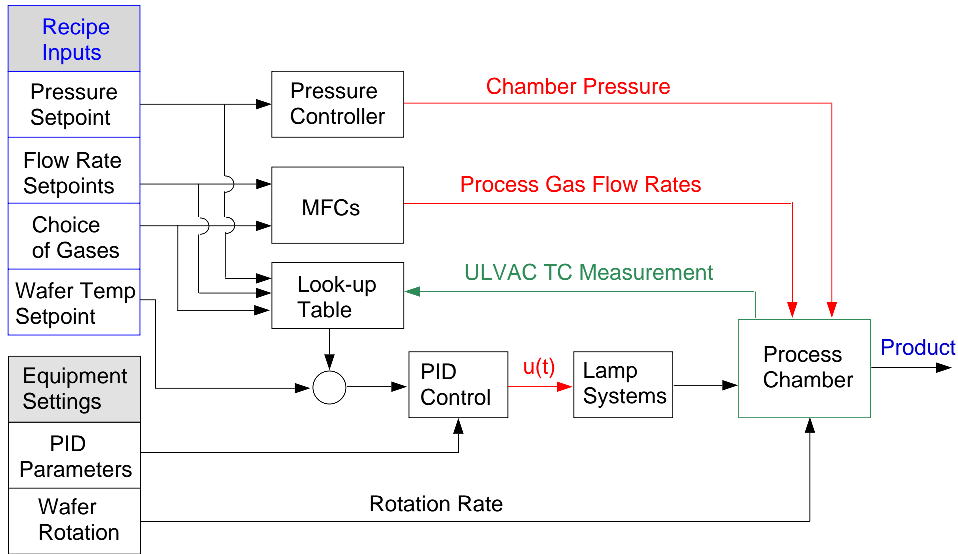

Figure 2.4: ULVAC W CVD reactor operating and control structure.

justing functions at different pressure ranges are plotted in Figures 2.5, 2.6, 2.7. This calibrated wafer temperature is then compared to the recipe setpoint and the PID controller adjusts the lamp power to bring wafer temperature to the desired value. However, because of the aging in the reactor lamps and the other changes of the equipment conditions, the look-up table deviates from current processing conditions and the adjusted wafer temperature value does not reflect the true wafer temperature as shown in the experimental results in the next chapter.

The CVD reactor can also be operated in an input/output (I/O) mode. In the I/O mode, the set points must be changed manually while processing and the internal look-up table is inactive.

As stated earlier, wafer temperature is set as recipe input. However, this single setting does not provide the capability to adjust the temperature distribution across the wafer surface. Although the wafer rotation can average out

the nonuniform heat fluxes received by wafer in the azimuthal direction, the single ring heat lamp does not provide sufficient freedom to control the temperature uniformity in wafer radial direction. Alternative heating methods such as heating susceptor plate are currently under investigation.

2.4 ULVAC W CVD Transport Model Formulation

Two coordinate systems are used in two modeling domains corresponding to their physical geometries. For gas phase model, a simplified rectangular domain is adopted with its origin located at the left lower corner of the reactor chamber as shown in Figure 2.3. The streamwise, spanwise, and normal coordinates are labeled as x, y, and z, respectively. On the other hand, the cylindrical coordinate system is used for the wafer and showerhead, and the coordinate origin overlaps the center of rectangular domain at the chamber floor. The radial and spinwise directions are defined as r and θ, and the axial direction is the same as the z direction in gas rectangular domain.

We assume the wafer shape is perfectly cylindrical and the wafer is pure silicon without the thin natural silicon oxide layer on the wafer surface. This allows us to use the physical properties of pure silicon for wafer.

2.4.1 Gas Flow Field

Although feed gas can enter from both the showerhead and side slits, we will only consider the case where the gas flow field over the wafer is assumed to be dominated by the horizontal flow, generated by the feed gas entering through the side wall nozzle. This assumption is suitable in our simulated operating

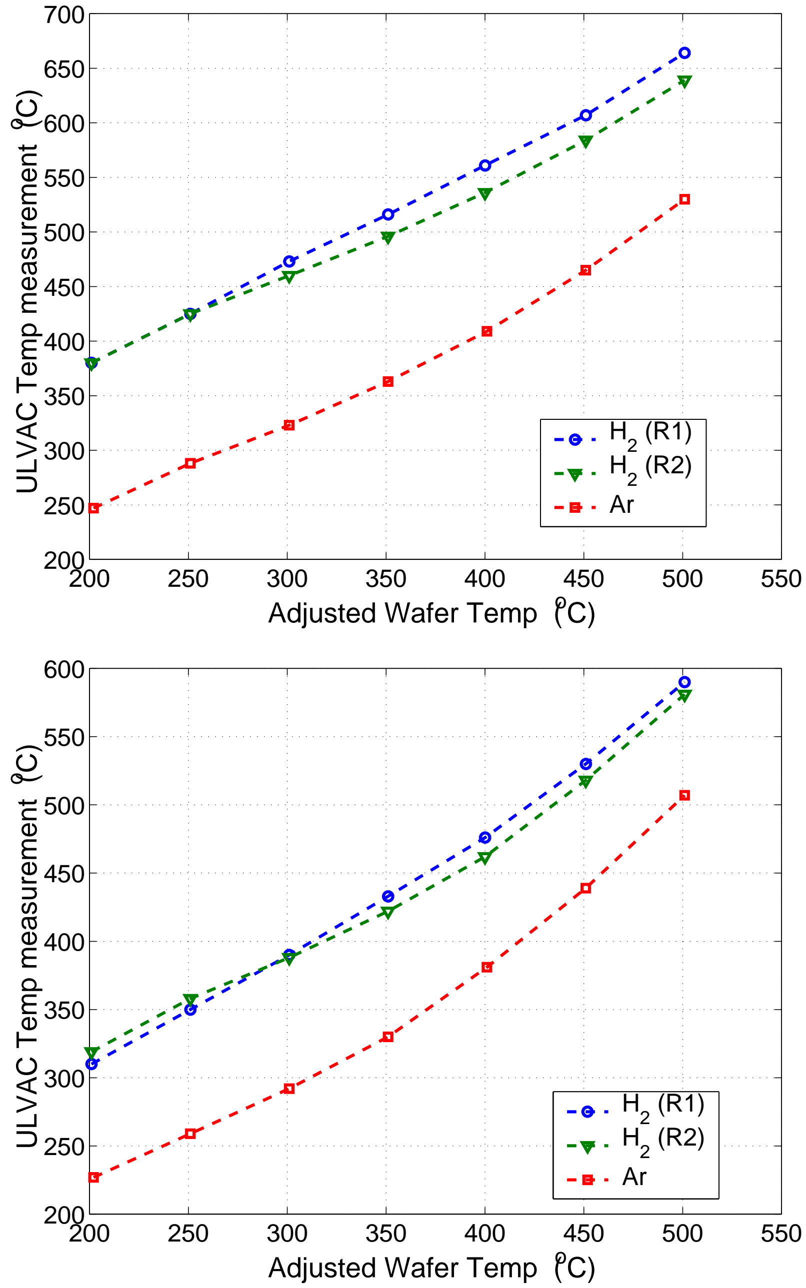

Figure 2.5: The default ULVAC look-up table correcting functions plotted as the ULVAC thermocouple measurements against the adjusted wafer temperature at (top) 0.8 $Torr$ and (bottom) 0.4 $Torr$ total chamber pressure in pure H_2 or Ar gas. R1 and R2 represent the correcting function for reactors 1 and 2, respectively.

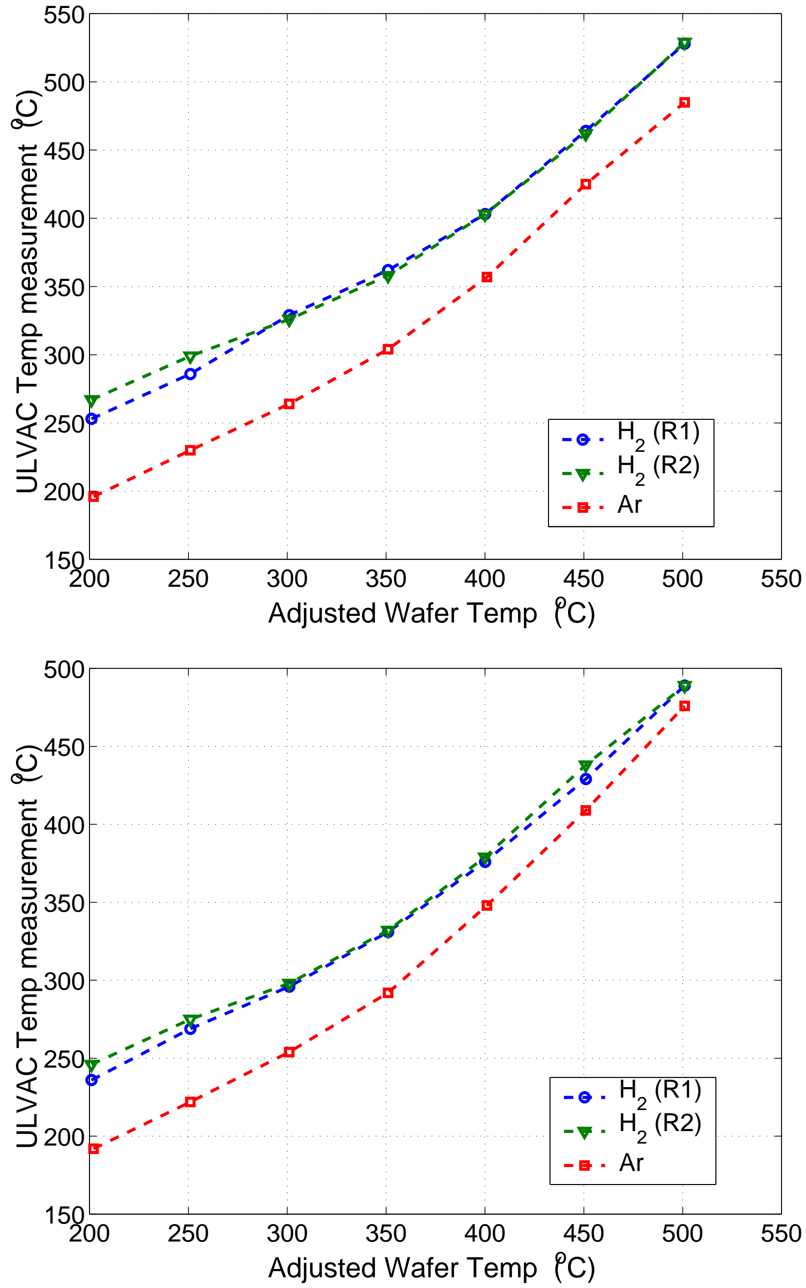

Figure 2.6: The default ULVAC look-up table correcting functions plotted as the ULVAC thermocouple measurements against the adjusted wafer temperature at (top) 0.17 $Torr$ and (bottom) 0.1 $Torr$ total chamber pressure in pure H_2 or Ar gas. R1 and R2 represent the correcting function for reactors 1 and 2, respectively.

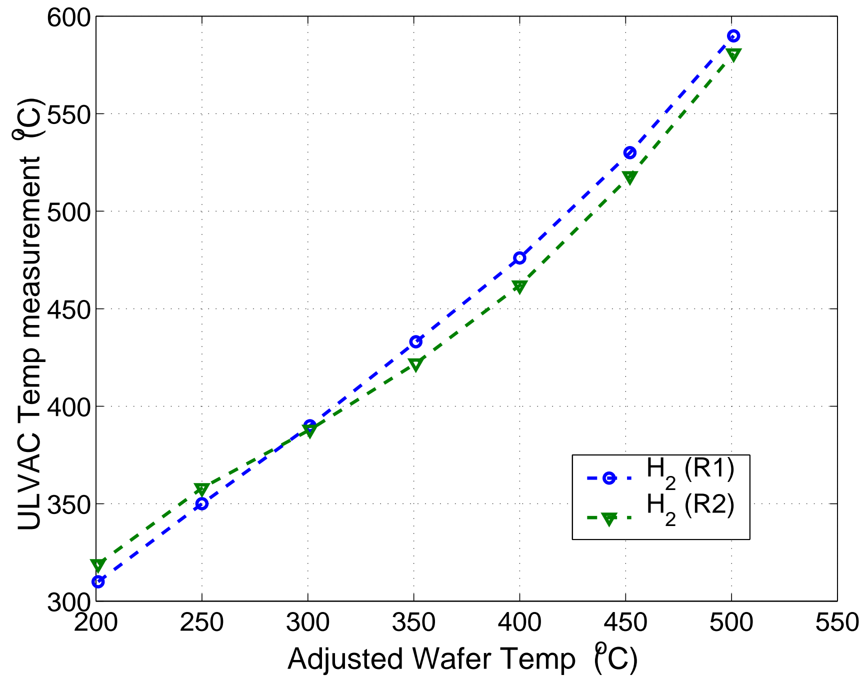

Figure 2.7: The default ULVAC look-up table correcting functions plotted as the ULVAC thermocouple measurements against the adjusted wafer temperature at high vacuum condition $1.8\times10^{-6}Torr$ total chamber pressure in pure H_2 or Ar gas. R1 and R2 represent the correcting function for reactors 1 and 2, respectively.

condition in which H_2 is not used; it is also verified by our experimental and simulation results discussed later and is supported by the gas flow visualization tests performed by the system manufacturer (BTU-ULVAC [90]) using a TiO_2 tracer which demonstrates that a rectangular pipe flow model maybe a suitable approximation for the reactant gas mixture in the neighborhood of the wafer.

The fully developed, laminar velocity profile is obtained by solving steady state Navier-Stokes and continuity equations. The transport and gas thermodynamic properties are assumed constant in the bulk phase and evaluated at the gas inlet temperature T_{amb}. It is also assumed that the slow wafer rotation as well as buoyancy-induced secondary flows, such as longitudinal and transverse recirculation resulting from free thermal convection near the wafer surface and chamber walls, do not affect the flow field. Because the Grashof number evaluated at the gas inlet is small (Gr=1.32) in our simulation, transverse recirculations should not occur in this low-pressure system according to the criteria suggested by Ingle and Mountziaris [46]. Other studies, such as Holstein and Fitzjohn [50] and Jensen [45], reveal that longitudinal recirculations occur in atmospheric pressure CVD systems at higher Rayleigh numbers (> 1780) than those representative of our system ($Ra = 0.59$) and so also should not occur. Therefore, the governing equations for the flow field component in the x direction are written as

$$\begin{aligned} \frac{\partial v_x^*}{\partial x^*} &= 0 \\ \mu(\frac{\partial^2 v_x^*}{\partial y^{*2}} + \frac{\partial^2 v_x^*}{\partial z^{*2}}) &= \frac{dp^*}{dx^*} \end{aligned}$$

subject to the no-slip boundary conditions at $y = 0,\ 2\bar{Y}$ and $z = 0,\ 2\bar{Z}$,

$$v_x^* = 0 \qquad \text{at } y^* = 0, 2\bar{Y}$$

$$v_x^* = 0 \qquad \text{at } z^* = 0, 2\bar{Z}$$

where the superscript * represents the dimensional quantities and $2\bar{Y}$ and $2\bar{Z}$ are the length of gas domain in y and z direction, respectively.

2.4.2 Gas Temperature Field

Neglecting heat generated by viscous dissipation, interdiffusion, thermal diffusion, and the gas phase chemical reactions, the gas phase energy balance equation (2.4) gives

$$\rho C_p v_x^* \frac{\partial T_g^*}{\partial x^*} = k \left(\frac{\partial^2 T_g^*}{\partial x^{*2}} + \frac{\partial^2 T_g^*}{\partial y^{*2}} + \frac{\partial^2 T_g^*}{\partial z^{*2}} \right).$$

Gas inlet temperature is assumed equal to the water-cooled chamber wall temperature T_{wall}; a zero temperature gradient along the flow direction boundary condition is used at the gas outlet. Assuming uniform temperature distribution across the wafer and showerhead, the gas temperature is set equal to the wafer temperature T_w inside the region of wafer radius R_w at $z = 0$, and the showerhead temperature T_{sh} inside the region of showerhead radius R_{sh} at $z = 2\bar{Z}$. The remaining areas in the top and bottom domain boundaries are assumed at wall temperature. Overall, this gives the gas temperature boundary conditions:

$$
\begin{aligned}
T_g^* &= T_{amb} \quad \text{at } x^* = 0 \\
\frac{\partial T_g^*}{\partial x^*} &= 0 \quad \text{at } x^* = 2\bar{X} \\
T_g^* &= T_{wall}^* \quad \text{at } y^* = 0, 2\bar{Y} \\
T_g^* &= \begin{cases} T_{sh}^* & \text{at } z^* = 2\bar{Y}, \quad (x^* - \bar{X})^2 + (y^* - \bar{Y})^2 < R_{sh}^2 \\ T_{wall}^* & \text{at } z^* = 2\bar{Y}, \quad R_{sh}^2 < (x^* - \bar{X})^2 + (y^* - \bar{Y})^2 \end{cases} \\
T_g^* &= \begin{cases} T_w^* & \text{at } z^* = 0, \quad (x^* - \bar{X})^2 + (y^* - \bar{Y})^2 < R_w^2 \\ T_{wall}^* & \text{at } z^* = 0, \quad R_w^2 < (x^* - \bar{X})^2 + (y^* - \bar{Y})^2. \end{cases}
\end{aligned}
$$

2.4.3 Wafer Thermal Dynamics

The two-dimensional wafer thermal dynamics model can be written as follows,

$$
\Delta_{Z_w} \rho_w \frac{\partial \left(C_{p_w} T_w \right)}{\partial t} = \Delta_{Z_w} \nabla^2 (\kappa_w T_w) + Q_{lamp} + Q_{rad} + Q_{top} + Q_{bot} \tag{2.7}
$$

where the energy fluxes from the lamp heating, radiation loss, convective/conductive losses from wafer top, and conduction loss from wafer bottom are defined as

$$
\begin{aligned}
Q_{lamp} &= \alpha_w(T_w) Q_{lp}(r) u(t) \\
Q_{rad} &= -\frac{F_{A,top}\sigma(T_w^4 - T_{sh}^4)}{\epsilon_w^{-1}(T_w) + \epsilon_{sh}^{-1}(T_{sh}) - 1} - \frac{F_{A,bot}\sigma(T_w^4 - T_f^4)}{\epsilon_w^{-1}(T_w) + \epsilon_f^{-1}(T_f) - 1} \\
Q_{top} &= \kappa_g(T_{w,z=0}) \frac{\partial T_{g,z=0}}{\partial z} \\
Q_{bot} &= -h_{eff}(T_w)(T_w - T_f).
\end{aligned} \tag{2.8}
$$

In the model, the subscripts w, sh, and f represent the state variables or physical properties corresponding to the wafer, showerhead, and chamber floor, respectively. Δ_{Z_w} is the wafer thickness, σ is the Boltzmann constant, and F_A is the geometric factor that is equal to 1 for both wafer top and bottom surfaces [88].

h_{eff} is an effective heat transfer coefficient, Q_{lp} is the incident lamp bank emissive power at the wafer surface, and $u(t)$ is dimensionless time-dependent lamp control signal recorded from the experiments. ϵ is the temperature-dependent total emissivity and the wafer absorptivity α_w is assumed equal to the emissivity of silicon [91]. The emissivity factor F_ϵ defined for parallel disk d_1 and d_2 is

$$\begin{aligned} F_\epsilon &= \frac{\epsilon_1(T_1)\epsilon_2(T_2)}{\epsilon_1(T_1)+\epsilon_2(T_2)-\epsilon_1(T_1)\epsilon_2(T_2)} \\ &= \frac{1}{\epsilon_1^{-1}(T_1)+\epsilon_2^{-1}(T_2)-1}. \end{aligned}$$

Calculation of Lamp Radiation Heat Flux

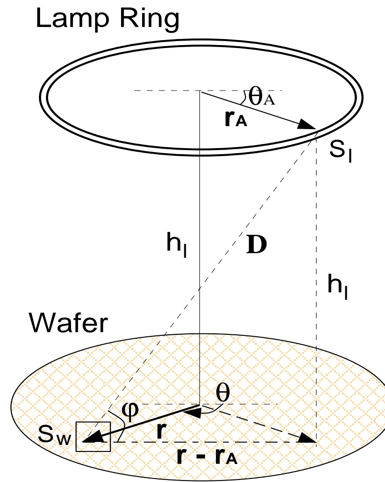

Figure 2.8: Geometry of the heating lamp and wafer.

The lamp radiation absorbed by the wafer is a function of temperature dependent total wafer absorptivity α_w, adjustable input signal with the value between 0 and 1 from lamp power controller $u(t)$, and the nominal lamp radiation $Q_{lp}(r)$. The nominal radiative lamp heat flux at every point on wafer surface depends on both the distances between the lamp elements and the specific point and the incident angle at that point between radiation flux and wafer surface. Figure 2.8

shows the simplified geometry of the ULVAC system circular heating bulb ring and the wafer.

Assuming there is a pair sample points S_w(r,θ) at the wafer surface and $S_l(r_A, \theta_A)$ on the lamp ring, the distance D from the wafer point S_w to any lamp element S_l can be calculated using the following equation,

$$\begin{aligned} D &= \sqrt{h_l^2 + (r\cos\theta - r_A\cos\theta_A)^2 + (r\sin\theta - r_A\sin\theta_A)^2} \\ &= \sqrt{h_l^2 + r^2 + r_A^2 - 2rr_A\cos(\theta - \theta_A)}. \end{aligned}$$

The radiative heat flux at S_l from the point heating source S_w can be computed by $\sin\phi\ Q_{max}/(\pi D^2)$ where Q_{max} is the maximum total lamp power. Because the ULVAC uses circular heating ring, the radiant flux thus will be symmetric around the wafer center. Therefore, the nominal total radiant flux from lamp system at maximum power to the wafer surface at radius r is obtained by integrating the heat flux over the entire lamp ring,

$$\begin{aligned} Q_{lp}(r) &= \frac{1}{2\pi}\int_0^{2\pi} \sin\phi \frac{Q_{max}}{4\pi D^2} d\theta_A \qquad (2.9) \\ &= Q_{max}\left[\frac{h_l}{(2\pi)(4\pi)}\int_{-\pi}^{\pi}\left[h_l^2 + r^2 + r_A^2 - 2rr_A\cos(\theta - \theta_A)\right]^{-3/2} d\theta_A\right] \end{aligned}$$

where $\sin\phi = h_l/D$. The radial variation of the lamp radiant heat flux at $u = 1$ is plotted in Figure 2.9.

2.4.4 Showerhead Thermal Dynamics

The transparent quartz showerhead at the top center of the reactor chamber is designed to pass the lamp radiation to wafer; however, it also absorbs part of the radiative energy directly from the tungsten halogen lamps and the radiation

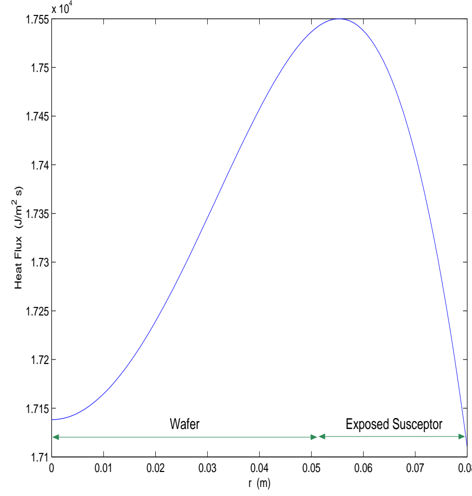

Figure 2.9: Radial variation of the lamp radiant heat flux at the wafer surface at full lamp power.

emitted from wafer [92, 93]. To sustain the pressure differential between the inner and outer surfaces, the quartz window also must be sufficiently thick to handle the stress. The thick quartz window thus becomes a heat source because quartz is not a good thermal conductor and at the low pressure operating condition, the amount of convective cooling inside the chamber or provided by the H_2 flow is small [92]. To account for the radiant energy exchanges between the quartz showerhead and wafer, and also the showerhead and reactor walls to a lesser extent, a showerhead window energy balance equation similar to that of the wafer is formulated:

$$\begin{aligned}\Delta_{Z_{sh}}\rho_{sh}\frac{\partial\left(C_{p_{sh}}T_{sh}\right)}{\partial t} &= \Delta_{Z_{sh}}\kappa_{sh}\nabla^2 T_{sh}+\alpha_{sh}(T_{sh})Q_{lp}(r)u(t) \\ &+\frac{F_{sh,w}\sigma(T_w^4-T_{sh}^4)}{\epsilon_w^{-1}(T_w)+\epsilon_{sh}^{-1}(T_{sh})-1}+\frac{F_{sh,f}\sigma(T_f^4-T_{sh}^4)}{\epsilon_f^{-1}(T_w)+\epsilon_{sh}^{-1}(T_f)-1} \\ &+h_{sh}(T_{sh})(T_{g,z=1}-T_{sh}). \qquad (2.10)\end{aligned}$$

2.4.5 Thermocouple Thermal Dynamics

Although the commercially manufactured thermocouple instrumented wafer is designed to measure the wafer temperature, it is still recognized that the thermocouple temperature can be different from the true wafer temperature [94, 95]. The heat losses through the wire, heat conduction in the wafer and the thermal contact resistance between the wafer and the thermocouple junction are some mechanisms that have been identified to account for the difference between true wafer temperature and the thermocouple reading [94]. In this research, we use a thermocouple temperature model similar to Vandenabeele and Renken [4],

$$M_{TC}\frac{\partial T_{TC}}{\partial t} = \alpha_{TC}Q_{lp}u(t) + h_{TC}(T_w - T_{TC}). \tag{2.11}$$

2.4.6 Gasous Reactants and Wafer Physical Properties

In typical low pressure CVD processes, the dilute gas mixture assumption usually approximates the gas mixture properties satisfactorily [9]. However, the recipe for blanket tungsten deposition we studied on the ULVAC reactor uses a relatively small ratio of reactant gases ($H_2/WF_6 = 4$) with large molecular weight difference ($H_2/WF_6 = 2/298$) and no carrier gas. To accurately estimate the gas mixture properties, we employed a molecular kinetic theoretic model that was experimentally verified to have very high accuracy.

On the other hand, the wafer temperature varies wildly during the process cycle, and its optical properties are strong functions of the temperature. Due to the dominant radiant transfer mechanism, represented by emissivity times fourth power of the wafer temperature, as well as other chamber components inside the reactor, a good emissivity model for the silicon wafer is critical to

accurately modeling the wafer dynamic temperature.

Gas Mixture Physical Properties

Two different kinds of physical properties are used in the transport equations: thermodynamics properties and transport properties. For pure species, the thermodynamics properties such as heat capacity and enthalpy can be obtained either from original experimental data or from the computation of the polynomial interpolation functions [38, 96]. The mixture-average method [96] is used to find the corresponding thermodynamics properties of the gas mixture.

While the pure species transport properties, e.g., viscosity and thermal conductivity, can be determined from the calculation of experimental data-based temperature functions if available, they also can be computed from the kinetic theory [38, 96] for the less common species. The Chapman-Enskog theory gives expressions for the transport coefficients in terms of the potential energy of interaction between a pair of molecules, and the negative derivatives of the potential function with respect to the distance between molecules then represents the interactive forces. One reasonable accurate potential energy function is the Lennard-Jones potential function, $\phi_{LJ}(r) = 4\epsilon[(\sigma_{LJ}/r)^{12} - (\sigma_{LJ}/r)^{6}]$, where it shows weak attraction at larger separations ($\propto r^{-6}$) and strong repulsion at small separations ($\propto r^{-12}$). Each species is characterized by a set of parameters of this potential function: the collision diameter σ_{LJ} and the maximum energy of attraction between a pair of molecules ϵ_{LJ}. The values of these two parameters for each species can be found experimentally or estimated from gas critical (c)

or liquid boiling (b,l) properties:

$$\frac{\epsilon_{LJ}}{\sigma} = 0.77T_c \quad \sigma_{LJ} = 0.841\tilde{V}_c^{1/3}$$
$$\frac{\epsilon_{LJ}}{\sigma} = 1.15T_b \quad \sigma_{LJ} = 1.166\tilde{V}_{b,l}^{1/3}$$

where σ is the Boltzmann constant.

Defining the dimensionless temperature variable $\Omega_\mu = \sigma T/\epsilon_{LJ}$, the viscosity and thermal conductivity of pure species are then approximated as follows,

$$\mu = 2.6693 \times 10^{-5} \quad \frac{\sqrt{MT}}{\sigma_{LJ}^2 \Omega_\mu}$$

$$\kappa = \begin{cases} \frac{5}{2}\frac{R}{M}\mu & \text{monatomic} \\ \left(\hat{C}_p + \frac{5}{4}\frac{R}{M}\right)\mu & \text{polyatomic} \end{cases}$$

and the binary diffusion coefficient can be obtained as

$$\mathcal{D}_{AB} = 1.8583 \times 10^{-3} \quad \frac{\sqrt{T^3\left(M_A^{-1} + M_B^{-1}\right)}}{P\sigma_{AB,LJ}^2 \Omega_{\mathcal{D},AB}}$$

with $\Omega_{\mathcal{D},AB} = \sigma T/\epsilon_{AB,LJ}$, $\sigma_{AB,LJ} = (\sigma_{A,LJ} + \sigma_{B,LJ})/2$ and $\epsilon_{AB,LJ} = \sqrt{\epsilon_{A,LJ}\epsilon_{B,LJ}}$. Here, R is gas constant and M is molecular weight. The dimensionless variables Ω_μ and $\Omega_{\mathcal{D},AB}$ can also be interpreted as the deviations from molecular rigid sphere behavior assumption.

The mixture-average method [96] is still used to compute the mixture viscosity and thermal conductivity from the following equations:

$$\mu_{mix} = \sum_{i=1}^{n} \frac{x_i \mu_i}{\sum_{j=1}^{n} x_i \Phi_{ij}}$$
$$\kappa_{mix} = \sum_{i=1}^{n} \frac{x_i \kappa_i}{\sum_{j=1}^{n} x_i \Phi_{ij}}$$
$$\Phi_{ij} = \frac{1}{8}\left(1 + \frac{M_i}{M_j}\right)^{-1/2}\left[1 + \left(\frac{\mu_i}{\mu_j}\right)^{1/2}\left(\frac{M_j}{M_i}\right)^{1/2}\right]$$

where x_i is the i-th species molar fraction.

One the other hand, the multicomponent formulation is adapted for computing the mixture diffusion coefficients. This method gives better accuracy than mixture-average formula in multicomponent environments because the latter is only correct asymptotically in some special cases such as in a binary mixture, or in diffusion of trace amounts of species into a nearly pure species [96]. The multicomponent formulation of mixture diffusion coefficient for species k is computed as

$$\mathcal{D}_{k,mix} = \frac{\sum_{j \neq k}^{n} x_j M_j}{\overline{M} \sum_{j \neq k}^{n} x_j / \mathcal{D}_{jk}}$$

where $\overline{M}$ is the mean molar mass. If the mixture is exactly a pure species, $x_j = \hat{x}_j + \hat{\epsilon}$ is used to avoid the numerical singularity, where $\hat{x}_j$ is the actual molar fraction and $\hat{\epsilon}$ is a small number less than 1×10^{-12}.

Wafer / Showerhead / Chamber Wall Physical Properties

The thermal radiative properties varies with wavelength and temperature. For example, the quartz showerhead is opaque to wavelengths greater than 4 μm and is transparent to shorter wavelengths. The radiant properties are more complicate for a wafer, where wafer emissivity also varies with surface roughness, wafer thickness, and doping [97]. The variation of emissivity beyond targeted wavelengths is one of the major problems for developing reliable in-situ, non-contact pyrometry wafer temperature measurement technique [97, 91].

In this research, we only consider the emissivity changes with respect to temperature and wavelength, and are interested in the wafer spectral emissivity $\epsilon(\lambda)$ which is defined as the ratio of the radiation emitted by a wafer at a given wavelength, angle of incidence, and plane of polarization to that emitted from

a black body under the same conditions. This spectral emissivity of an object under the same conditions should be identical to its absorptivity $\alpha(\lambda)$ due to Kirchhoff's law. Integrating the spectral emissivity over the chosen wavebands, weighted by the system's energy distribution, we can get the wafer or showerhead radiative properties as functions of corresponding temperatures. For typical CVD processes, the wavelength extremes of 0.4 and 25 μm include most of the emitted radiation [97, 91].

For example, the wafer emissivity is computed by

$$\epsilon(T_w) = \frac{\int_{0.4}^{25} \epsilon(\lambda, T) W_{bb}(\lambda, T) d\lambda}{\int_{0.4}^{25} \epsilon(\lambda, T) d\lambda}$$

where W_{bb} is the spectrum of radiation emitted from a black body described by the Plank radiation function

$$W_{bb}(\lambda, T) = \frac{c_1}{\lambda^5 \left(exp(\frac{c_2}{\lambda T}) - 1 \right)}$$

with constant $c_1 = 3.7418 \times 10^8 \; W \mu m^4 m^{-2}$ and $c_2 = 1.4388 \times 10^4 \; \mu m K$.

The wafer absorptivity is assumed to be identical with its emissivity over the temperature range of interest [98, 91], and the optical properties of the quartz showerhead and susceptor are interpolated from Dilhac et. al. [99]. A constant emissivity of 0.26 is used for the cooled, oxidized aluminum chamber wall and floor. Temperature dependent heat capacities and thermal conductivities are used and are interpolated from the experimental data in [100] for silicon and [101] for quartz.

2.5 Dimensionless Equations

The transport equations and boundary conditions can be made dimensionless by rescaling all the variables with the characteristic reference values. The resulting dimensionless groups in the governing equations will provide information regarding the relative importance of each tensor. The characteristic reference values and the dimensionless variables are summarized in Table 2.2.

Table 2.2: Summary of the dimensionless variables used in the transport model.

$x = x^*/2\bar{X}$	$T_g = (T_g^* - T_{amb})/T_{amb}$
$y = y^*/2\bar{Y}$	$T_w = T_w^*/T_{amb}$
$z = z^*/2\bar{Z}$	$T_{wall} = T_{wall}^*/T_{amb}$
$r = r^*/R_w$	$T_{sh} = T_{sh}^*/T_{amb}$
$t = t^*/\tau$	$T_f = T_f^*/T_{amb}$
$v_x = v_x^*/< v >$	$T_{TC} = T_{TC}^*/T_{amb}$
	$Q_{lp} = Q_{lp}^*/Q_{max}$

In the table, T_{amb} is the inlet gas temperature, $< v >$ is average gas entrance velocity, and $2\bar{X}, 2\bar{Y}$, and $2\bar{Z}$ are the true dimensions of the gas domain.

2.5.1 Gas Phase Flow and Energy Equations

Using the dimensionless variables defined in Table 2.2, the fully developed, laminar velocity profile is described by the continuity and steady-state Navier-Stokes

equations

$$\begin{aligned}\frac{\partial v_x}{\partial x} &= 0\\ \frac{\partial^2 v_x}{\partial y^2} + \alpha_v \frac{\partial^2 v_x}{\partial z^2} &= \beta_v.\end{aligned}$$

The dimensionless pressure drop term $\beta_v = 2\mathcal{P}\bar{Y}^2/(\mu < v > \bar{X})$ can only be determined after the flow field equations are solved. Thus, defining the flow velocity/pressure drop ratio as $\hat{v}_x = v_x/\beta_v$, the momentum balance equation can be written as

$$\frac{\partial^2 \hat{v}_x}{\partial y^2} + \alpha_v \frac{\partial^2 \hat{v}_x}{\partial z^2} = 1 \tag{2.12}$$

subject to no-slip boundary conditions $v_x = 0$ at $y = 0, 1$ and $z = 0, 1$.

The dimensionless gas temperature can be described by the steady-state conservation of energy equation

$$v_x \frac{\partial T_g}{\partial x} = \left(\delta_{gt} \frac{\partial^2}{\partial x^2} + \beta_{gt} \frac{\partial^2}{\partial y^2} + \gamma_{gt} \frac{\partial^2}{\partial z^2} \right) T_g = \mathcal{L} T_g. \tag{2.13}$$

After chosing the gas inlet temperature equal to the water-cooled chamber wall temperature, the gas temperature boundary conditions are simplified to

$$\begin{aligned}
T_g &= 0 \qquad \text{at } x = 0,\\
\frac{\partial T_g}{\partial x} &= 0 \qquad \text{at } x = 1,\\
T_g &= 0 \qquad \text{at } y = 0, 1,\\
T_g &= \begin{cases} C_{g,t}(T^*_{sh}) & \text{at } z = 1, \quad (x - 0.5)^2 + R^2_{xy}(y - 0.5)^2 \le R^2_t, \\ 0 & \text{at } z = 1, \quad (x - 0.5)^2 + R^2_{xy}(y - 0.5)^2 > R^2_t, \end{cases}\\
T_g &= \begin{cases} C_{g,b}(T^*_w) & \text{at } z = 0, \quad (x - 0.5)^2 + R^2_{xy}(y - 0.5)^2 \le R^2_b, \\ C_{g,f} & \text{at } z = 0, \quad (x - 0.5)^2 + R^2_{xy}(y - 0.5)^2 > R^2_b. \end{cases}
\end{aligned} \tag{2.14}$$

Representative process operating conditions correspond to a feed volumetric flow rate of 50 sccm, a feed gas temperature of $298K$ and mixture ratio of WF_6/H_2 equal to 1/4 sccm, chamber pressure of 0.5 torr, and a uniform wafer temperature set point at 500°C. The value of dimensionless parameters are given in Table 2.3.

Table 2.3: Definitions and values of physical properties and dimensionless parameters evaluated at 1 atm, $H_2/N_2 = 40/10sccm$, $T_{amb} = 25$, $T_w = 304.3$, $T_{sh} = 150$, and $T_f = 60^o$C.

Physical Properties	Value	Dimensionless Parameters	Value
ρ_g	1.9416×10^{-4} kg/m^3	$\alpha_v = \bar{Y}^2/\bar{Z}^2$	7.6224
κ_g	0.1295 J/(m K s)	$\beta_v = 2\mathcal{P}\bar{Y}^2/(\mu_g < v > \bar{X})$	-594.8230
C_{p_g}	398.26 J/(kg K)	$\alpha_{gt} = \kappa_g/(\rho_g C_{p_g})$	0.1674
μ_g	1.4520×10^{-5} kg /(m s)	$\delta_{gt} = \alpha_{gt}(2 < v > \bar{X})$	5.0696
ρ_w	2300 kg/m^3	$\beta_{gt} = \alpha_{gt}\bar{X}/(2 < v > \bar{Y}^2)$	7.3002
κ_w	67.8751 J/(m K s)	$\gamma_{gt} = \alpha_{gt}\bar{X}/(2 < v > \bar{Z}^2)$	55.6447
C_{p_w}	847.90 J/(kg K)	$C_{g,t} = T_{sh}/T_{amb}$	1.4195
ϵ_w	0.28	$C_{g,b} = T_w/T_{amb}$	1.9374
ρ_{qtz}	2.6433e3 kg/m^3	$C_{g,f} = T_f/T_{amb}$	1.1174
κ_{qtz}	2.3836 J/(m K s)		
$C_{p_{qtz}}$	1036.90 J/(kg K)		
ϵ_{qtz}	0.86		

2.5.2 Wafer and Showerhead Energy Balance Equations

By normalizing the temperature dependent physical properties with respect to the set of reference values, the dimensionless parameters are grouped and represent the relative importance of each transport mechanisms at those reference conditions. The resulting dimensionless wafer energy balance equation is shown as follows,

$$\begin{aligned} C_{p_w}\frac{\partial T_w}{\partial t} &= C_{w,cd}\frac{1}{r}\frac{\partial}{\partial r}\left(r\frac{\partial k_w(T_w)T_w}{\partial r}\right) + C_{w,lp}\left[\alpha_w(T_w)Q_{lp}u(t)\right] \\ &+C_{w,top}\left[F_{\epsilon,top}F_{A,top}\left(T_{sh}^4 - T_w^4\right)\right] + C_{w,bot}\left[F_{\epsilon,bot}F_{A,bot}\left(T_f^4 - T_w^4\right)\right] \\ &+C_{w,g}\left[h_g(T_w)(T_g + 1 - T_w)\right] + C_{w,f}\left[h_{w,f}(T_w)(T_w - T_f)\right] \end{aligned} \quad (2.15)$$

where the new wafer heat capacity is defined by

$$C_{p_w} = \frac{\tilde{C}^*_{p_w}}{\tilde{C}_{p_{w,ref}}} \qquad \text{and} \qquad \tilde{C}^*_{p_w} = T^*_w\frac{\partial C^*_{p_w}}{\partial T_w} + C^*_{p_w}.$$

Similarly, the dimensionless susceptor heat capacity $C_{p_{sh}}$ is defined as

$$C_{p_{sh}} = \frac{\tilde{C}^*_{p_{sh}}}{\tilde{C}_{p_{sh,ref}}} \qquad \text{and} \qquad \tilde{C}^*_{p_{sh}} = T^*_{sh}\frac{\partial C^*_{p_{sh}}}{\partial T_{sh}} + C^*_{p_{sh}}$$

and the dimensionless conservation of energy equations for susceptor and thermocouple are

$$\begin{aligned} C_{p_{sh}}\frac{\partial T_{sh}}{\partial t} &= C_{sh,cd}\frac{1}{r}\frac{\partial}{\partial r}\left(r\frac{\partial k_{sh}(T_{sh})T_{sh}}{\partial r}\right) + C_{sh,lp}\left[\alpha_{sh}(T_{sh})Q_{lp}u(t)\right] \\ &+C_{sh,w}\left[F_{\epsilon,sh-w}F_{A,sh-w}\left(T_w^4 - T_{sh}^4\right)\right] \\ &+C_{sh,f}\left[F_{\epsilon,sh-f}F_{A,sh-f}\left(T_f^4 - T_{sh}^4\right)\right] \\ &+C_{sh,g}\left[h_{sh}(T_{sh})(T_g + 1 - T_{sh})\right] \end{aligned} \quad (2.16)$$

$$C_{p_{TC}}\frac{\partial T_{TC}}{\partial t} = C_{TC,lp}\left[\alpha_{TC}Q_{lp}u(t)\right] + C_{TC,cd}\left[h_{TC}(T_w - T_{TC})\right]. \quad (2.17)$$

The dimensionless variables in equations (2.15), (2.16), and (2.17) are defined in Table2.4.

Table 2.4: Definitions of dimensionless parameters used in wafer, showerhead, and thermocouple modeling equations.

$C_{w,z} = \tau/(\Delta_{z_w}\rho_w\tilde{C}_{p_{w,ref}}T_{amb})$ [a]	$C_{sh,z} = \tau/(\Delta_{z_{sh}}\rho_{sh}\tilde{C}_{p_{sh,ref}}T_{amb})$ [a]
$C_{w,cd} = C_{w,z}(\Delta_{z,w}\kappa_{w,ref}T_{amb})/\Delta^2_{r_w}$	$C_{TC,z} = \tau/M_{TC}T_{amb}$ [a]
$C_{w,lp} = C_{w,z}Q_{max}$	$C_{sh,lp} = C_{sh,z}Q_{max}$
$C_{w,top}, C_{w,bot} = C_{w,z}\sigma T^4_{amb}$	$C_{sh,w}, C_{sh,f} = C_{sh,z}\sigma T^4_{amb}$
$C_{w,g} = C_{w,z}h_{g,ref}T_{amb}$	$C_{sh,g} = C_{sh,z}h_{sh,ref}T_{amb}$
$C_{w,f} = C_{w,z}h_{f,ref}T_{amb}$	$C_{TC,lp} = C_{TC,z}Q_{max}$
	$C_{TC,lp} = C_{TC,z}h_{TC,ref}T_{amb}$

[a] Dimensional parameters (m^2s/J).

Chapter 3

Experimental Studies

In this chapter we address the problem of setting up a data acquisition system for the ULVAC tungsten CVD reactor and present experimentally measured wafer temperature data used for equipment transport model development and validation. As stated in Section 2.3, the current ULVAC CVD reactor does not have an in-situ wafer temperature measurement apparatus and relies on the internal look-up table to compute the process condition-adjusted wafer temperature. Thus, the thermocouple instrumented wafer placed in the reactor chamber will provide valuable information regarding the true wafer temperature during the processes.

By carefully designing the processing conditions and recipes, the experimental results can be used to examine the basic assumptions of the mathematical models and distinguish the most important heat transfer effects from the others. The conduction and convection energy transfer at the gas/wafer interface is studied in this research by changing the gas composition and total flow rate, while other system dependent parameters, such as wafer thermal time constant, are estimated from the wafer temperature transient response.

Detailed descriptions of the thermocouple wafer and the data acquisition system hardware and software are presented in Section 3.1. Signal conditioning and integration issues are also discussed. The nonlinear behavior between the lamp power control signal and the power actually supplied to the lamp filaments are investigated using the steady-state experiments discussed in Section 3.2. In the following section, the influence of the gas composition on wafer temperature is demonstrated and different heat transfer mechanisms are examined. Results of the wafer temperature dynamics including the chamber pressure effects, recipes for achieving near constant deposition temperature, and parameter identification experiments are given in Section 3.4.

3.1 Data Acquisition in the ULVAC ERA-1000 System

The data acquisition system built in this research was used to record a variety of signals including the instrumented wafer temperature from five attached thermocouples, the ULVAC system wafer temperature, the lamp power controller signal, and the gas flow rates. Among these collected variables, only the TC wafer measurements were recorded directly from the measurement sensors and the remaining signals were collected by intercepting the inputs or outputs from the corresponding ULVAC system controllers. The general structure of the data acquisition system was demonstrated in Figure 3.1, and the ULVAC control scheme is shown in Figure 2.4.

There were three main components of this data acquisition system, namely the measurement apparatus (the TC test wafer), the signal processing hardware (for example, the computer boards), and the computer software user interface.

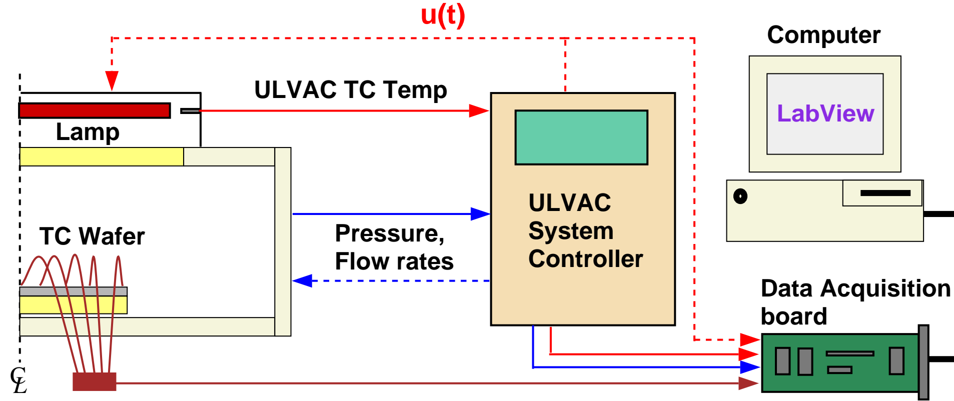

Figure 3.1: ULVAC CVD reactor data acquisition system.

Several integration issues between those main components had to be resolved to achieve high signal resolutions and ready-for-analyze data files:

- Compared to the signals such as lamp power controller output taken from the ULVAC system in the range of 0 to 10 V, the thermocouple signals from TC wafer were very small, measuring only between 10^{-4} and $5{\times}10^{-2}$ V. Therefore, the length of the connection cable between the extension board and the thermocouple wafer was restricted and the thermocouple signal had to be amplified as early as possible to obtain better signal-to-noise ratio before environmental noise was picked up by the connection cables. The connection cables were shielded with aluminum tape and the data acquisition board was housed in a metal box to reduce the environmental noise corruption. Because the signals taken from the ULVAC system were already close to the safety limitations of the computer boards, they could not be further amplified and were separately collected and processed in the second bank of signal terminals on the extension board. The TC measurements were collected and amplified with a high amplification ratio

in the other bank.

- In contrast to the single-ended voltage signals that were intercepted from the ULVAC system, the signal from the instrumented wafer measurement was of the floating differential type and the low and ground terminals of the corresponding channels on the extension board had to be closed with mounds of solder to provide a proper ground for the measurement. We used the same procedure to close out capacitors between the high and low terminals to add on-board signal filters for better thermocouple signal conditioning.

- A special data acquisition board having the capability to receive both floating differential and single ended signals was required to connect with the extension board. This particular acquisition board provided special treatment of the floating differential signals to increase the signal to noise ratio.

- Due to the setting of another data acquisition system on which the new system was built, we were only be able to record the adjusted ULVAC wafer temperature and did not have the access to the original ULVAC thermocouple measurements.

A more detailed descriptions of the instrumented thermocouple wafer and computer boards, and the LabVIEW software user interface are given in the following two subsections.

3.1.1 Instrumented Thermocouple Wafer and Computer Boards

A SensArray 1530 thermocouple (TC) wafer was used to measure the true wafer temperature, and the system was operated in I/O mode to enable manual loading/unloading of the instrumented wafer. There are five thermocouples, labeled as shown in Figure 3.2, attached to the top surface of this instrumented TC wafer. We note that the instrumented wafer is designed to measure the *wafer* temperature - as opposed to wafer surface or thermocouple temperature - by bonding the thermocouple leads in an undercut wafer area in a symmetric pattern [102, 95]. A $\pm$ 1.0 ^oC or better measurement variation between these thermocouples has been reported [102, 95]. The wafer rotation was turned off during the experiments to protect the leads of the test wafer.

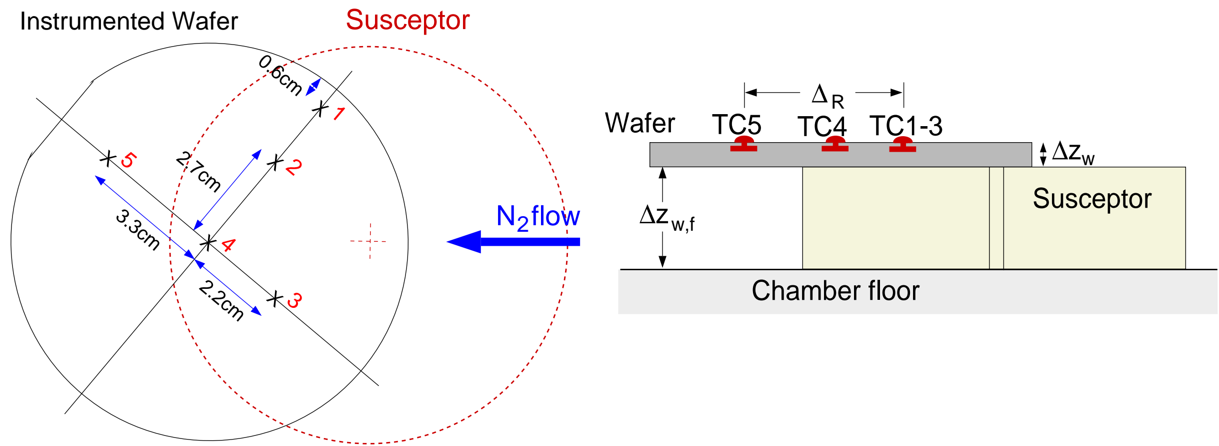

Figure 3.2: The top and side views of the test wafer position with thermocouple positions marked.

The temperature data collected from the instrumented wafer was sent to a personal computer-based data acquisition system that included a LabVIEW software interface and two computer boards: a CIO-DAS801 data acquisition board [103] and a CIO-EXP32 extension board [104]. Each thermocouple was

connected to a channel on the expansion board, where a low pass filter with bandwidth 7 Hz was implemented between the high and low ends and a 100 $k\Omega$ resistor was installed between low and ground to provide ground reference. The temperature signals were then amplified 300-fold before being sent to the data acquisition board. An on-board semiconductor sensor provides the adjustable cold junction compensation (CJC) function that subsequently is used as a reference to the measured thermocouple signals in the LabVIEW program. Additional processing variables of ULVAC CVD system, such as the system thermocouple temperature measured near the lamp, lamp power control signal, chamber pressure, and gas feed rates, are collected during the processing cycle. The default sampling rate was 20 Hz.

3.1.2 LabVIEW Data Acquisition Interface

The LabVIEW is a graphical programming language developed by National Instruments, Inc. [105] for a broad range of applications including data acquisition and analysis, process monitoring and control, and factory automation and personnel instrumentation. We built our data acquisition computer interface by prototyping the existing modules such as hardware drivers in the forms of dynamic link library (DLL) in the LabVIEW. Figures 3.3 showed the LabVIEW graphical user interface (GUI) developed in this research for collecting instrumented wafer temperature and other system parameters.

There were three main construction blocks in this interface program. To receive the signals from extension and data acquisition boards, we used the code interfaces, which were part of the DLL library supplied by acquisition board vendor Computer Boards, for temperature measurements of each thermocouple

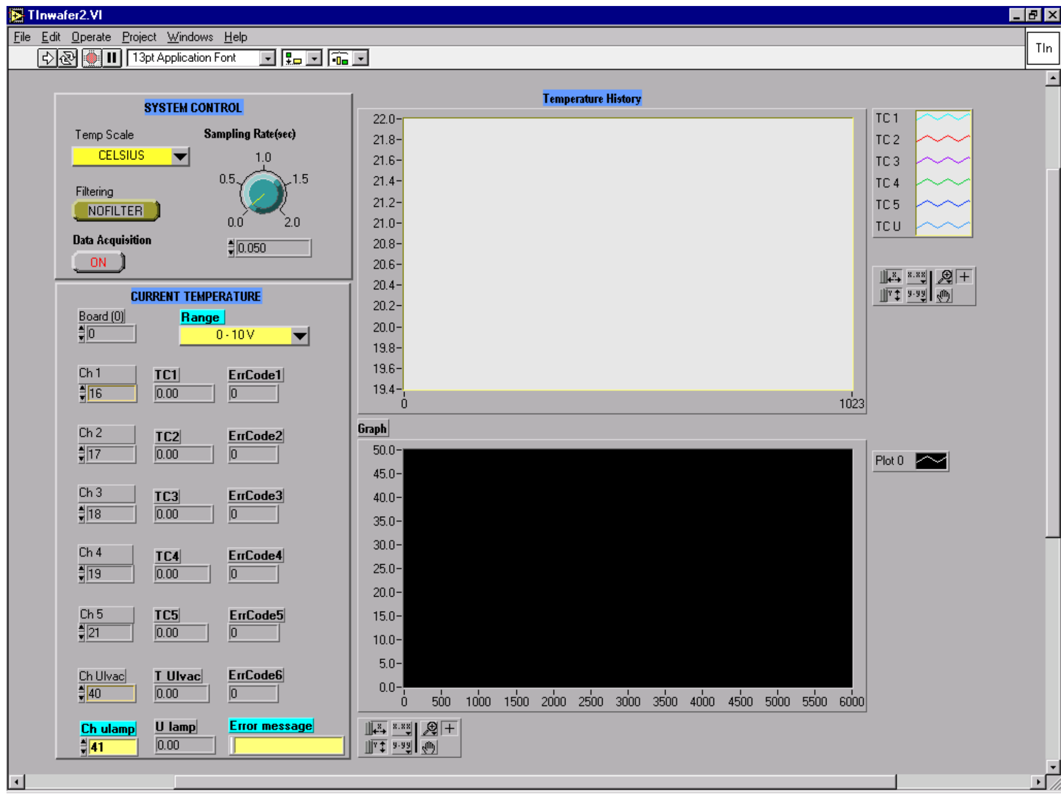

Figure 3.3: LabVIEW data acquisition interface window.

on test wafer and the voltage signals from the ULVAC control system. Each code interface had its own GUI visual instrument (VI) component to display the numerical values or errors, shown at the left bottom block in Figure 3.3. The system control block, at the left upper area in Figure 3.3, used a while-loop and an internal clock to start/end the data acquisition and adjusted the sampling rate. The sampling rate varied depending on the computer motherboard and CPU speed. In the current system at the LAMP lab, we could achieve a sampling rate as high as 50 Hz. The program also had the ability to apply a 10 measurements-based floating time-averaging filter for all signals, but it was usually set inactive to gain better data resolution during the fast transient of wafer temperature. A monitoring plot and a measurement history graph composed the right side of the GUI to display the on-going measurements during the data acquisition and the time trajectory of each signal after finishing the data collection, respectively. When the data acquisition was stopped, the program saved collected data into spreadsheet files for further analysis.

This LabVIEW platform can be expanded to do the real-time statistical analysis and order differential equation integration, and that makes it very useful for future real-time, model-based sensing and control applications and integration. However, the trade-offs between the more sophisticated implementations that require more computer CPU time and the data sampling rate have to be considered.

3.2 Lamp Control Signal Correction

In the ULVAC CVD system, the power is supplied to the tungsten lamp filaments by sending a 0 to 10 V signal from the system wafer temperature controller to the power supplies that drive the lamps. As indicated by Schaper et. al. [7], the relationship between the lamp power control signal applied to the power supplies and the power actually sent to the lamp is not necessarily linear. To understand this nonlinearity is important because it directly relates to the radiative power from the lamp bank and should be considered for future temperature controller design and improvement.

Because the power level cannot be set directly from the ULVAC control panel, a 50 ^oC step increment of the wafer temperature setpoints in the I/O mode was designed to characterize the lamp power control signal at those temperature levels. The true current through, and voltage across the lamp filaments were observed and recorded from the corresponding meters on the ULVAC control panel when the ULVAC wafer temperature came to steady state at each temperature step. A smaller decrease step of the setpoints during the temperature ramp-down period was used to verify the power values previously recorded in the temperature ramp-up phase. The ULVAC wafer temperature trajectory and the lamp bank control signal over the entire process are shown in Figure 3.4. The lamp current and voltage data are also listed in Table 3.1.

The relationship between the lamp control signal and the lamp power output, computed as the product of lamp current and voltage, is plotted in Figure 3.5, where the power factor $\cos\phi$ was omitted from the power computation [106]

$$Power = V_{rms}\ I_{rms}\ \cos\phi.$$

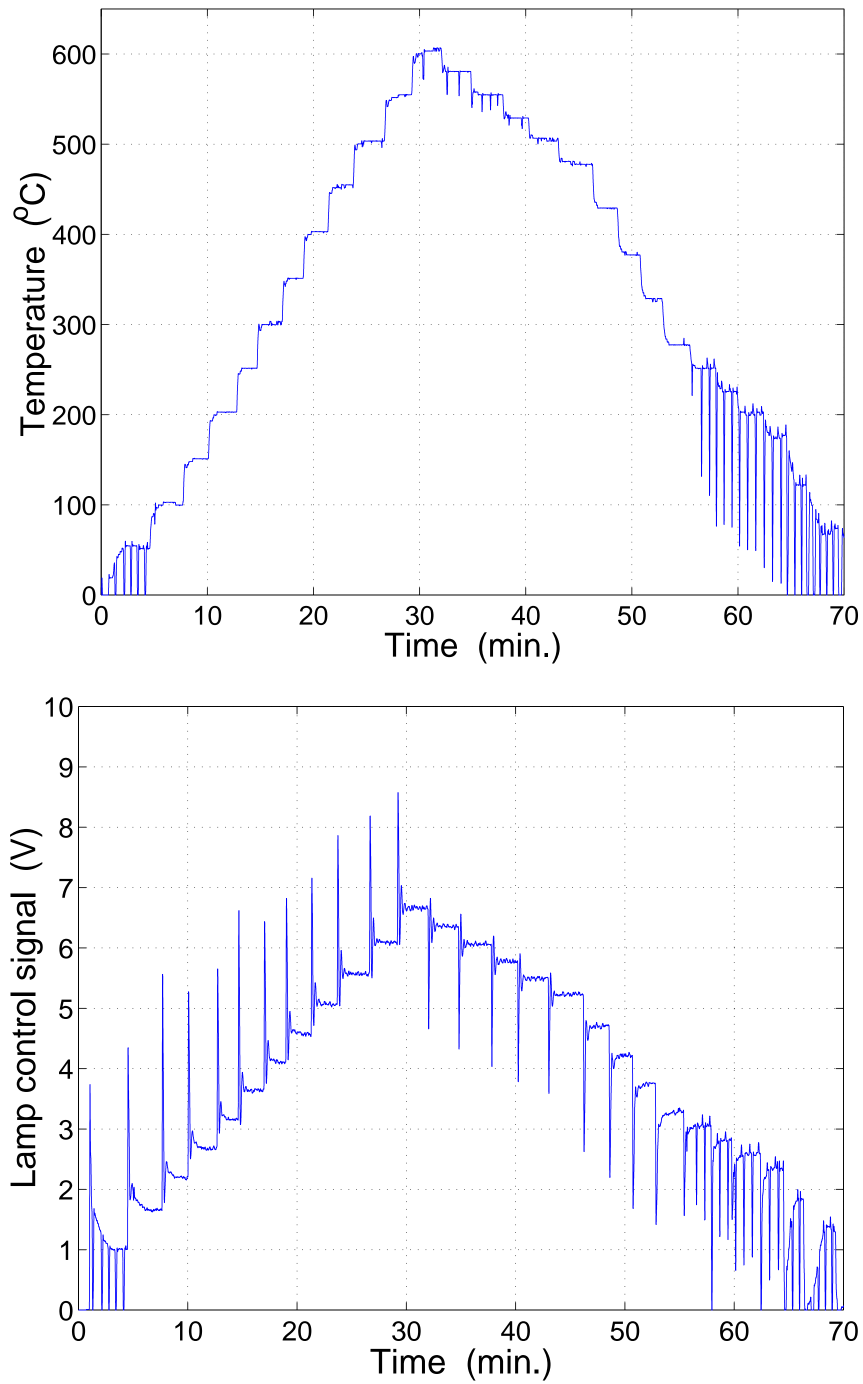

Figure 3.4: Relationship of the ULVAC wafer temperature (top) and the steady-state lamp power control signal (bottom) at 0.2 *Torr* total chamber pressure and 100 *sccm* N_2.

Table 3.1: Values of the lamp current and voltage and the lamp control signal.

Temp SP (^{o}C)	Current I (amp)	Voltage V (V)	I*V	Control Signal
19	4.2	14	58.8	1.01
50	6.05	30	181.5	1.66
100	7.34	44	322.96	2.2
150	8.34	55	458.7	2.67
200	9.28	67	621.76	3.16
250	10.18	78	794.04	3.63
300	10.9	89	970.1	4.11
350	11.68	99	1156.3	4.57
400	12.38	111	1374.2	5.06
450	13.1	122	1598.2	5.56
500	13.82	134	1851.9	6.1
550	14.56	147	2140.3	6.67
600	14.12	140	1976.8	6.35
575	13.76	133	1830.1	6.06
550	13.38	126	1685.9	5.77
525	12.98	121	1570.6	5.51
500	12.58	114	1434.1	5.23
475	11.84	103	1219.5	4.71
425	11.04	92	1015.7	4.23
375	10.34	81	837.54	3.77
325	9.49	70	664.3	3.28
275	9.07	64	580.48	3.05
250	8.6	61	524.6	2.82
225	8.17	53	433.01	2.58
200	7.64	47	359.08	2.35
175	6.48	35	226.8	1.84
125	5.14	22	113.08	1.31
75	3.8	12	45.6	0.86

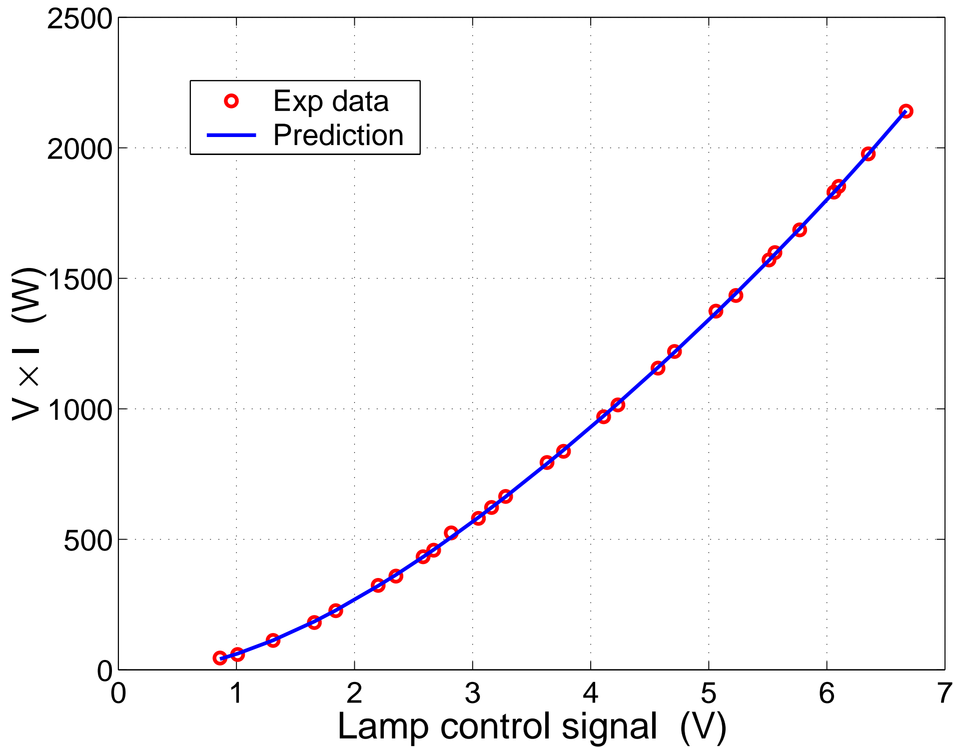

Figure 3.5: Relationship of the lamp control signal and the true lamp power (computed by the product of lamp current and voltage).

The V_{rms} and I_{rms} were the root-mean-square voltage and current as measured from the ULVAC system transducers, respectively. The true lamp power can be modeled as a nonlinear function of the control signal by a forth order polynomial

$$c_0 + c_1\ u + c_2\ u^2 + c_3\ u^3 + c_4\ u^4 = P_{V\times I}, \tag{3.1}$$

and the fitted values of the polynomial coefficient c_i are listed in Table 3.2.

The full range of the lamp power control signal is 0 to 10 V. However, because of safety concerns for the CVD reactor operations, the wafer temperature setpoints cannot be raised higher than 600 ^{o}C, thus limiting the highest available

Table 3.2: Values of the fitting coefficients c_i in Equation (3.1).

c_0	c_1	c_2	c_3	c_4
-10.8901	-14.3743	96.2330	-10.8691	0.6028

value of the steady state control signal to less than 7 V. Therefore, the use of the nonlinear function to predict radiative lamp power outputs is limited since the control signal can reach 10 V at the beginning of the wafer temperature fast ramp-up. An alternative method is to relate the maximum values of the lamp power signal in each step to corresponding voltage and current products, but the maximum lamp control signal data (Figure 3.4) did not provide consistent values as those obtained from the steady-state data.

3.3 Influence of Gas Composition on Wafer Temperature

Two sets of experiments were conducted to investigate the influence of gas composition and total flow rate on wafer temperature in the ULVAC system. The thermocouple wafer was intentionally shifted about 3.8 *cm* from susceptor center in the downstream direction, and slightly rotated so that thermocouple 5 was not located on top of the susceptor (see Figure 3.2). This shifting was designed to study the conductive heat transfer from wafer to the underlying susceptor.

The first experiment, designed to study the effect of gas mixture composition at constant total flow rate, began by changing the initial reactant gases feed rates of 100 *sccm* pure hydrogen (Case 1), to several different combinations: Case 2: 80 *sccm* H_2/20 *sccm* N_2; Case 3: 60 *sccm* H_2/40 *sccm* N_2; Case 4: 40 *sccm*

H_2/60 $sccm$ N_2; and Case 5: 100 $sccm$ N_2. The gas flow rates/composition were changed only after the instrumented wafer temperature reached steady-state in each period (approximately 20 minutes). The wafer temperature set point and chamber pressure were maintained at 500 ^oC and 500 $mTorr$ throughout the experiments. The lamp power was observed to remain constant after the initial fast ramp-up despite the true wafer temperature variations attributable to the changes in gas composition, as shown in Figure 3.6. This lack of movement of the system controller to compensate for true wafer temperature losses can be understood in terms of the following two reasons: first, the system thermocouple is located outside the reactor chamber, thus any gas composition change will have no effect on its temperature measurement; second, the fixed look-up table, designed to factor in the feed gas flows and chamber pressure when converting system thermocouple temperature to wafer temperature, was inactive in the I/O operation mode. Therefore, the system wafer temperature used as the feedback signal in the temperature control loop remained constant, producing no net set-point deviation. Detailed discussions regarding the ULVAC temperature control system can be found in [107].

The wafer temperature time histories for the first experiment are shown in Figure 3.6. The wafer temperature indicated by the ULVAC control system (measured by the lamp thermocouple) is also plotted for reference. Generally, the steady-state wafer temperature was found to be lower in pure hydrogen than for pure nitrogen, and it gradually increased with nitrogen fraction. Because the lamp power output was maintained at a constant level, these temperature differences are due to the changing gas mixture properties, most importantly the gas thermal conductivity: we note that the pure hydrogen thermal conductivity

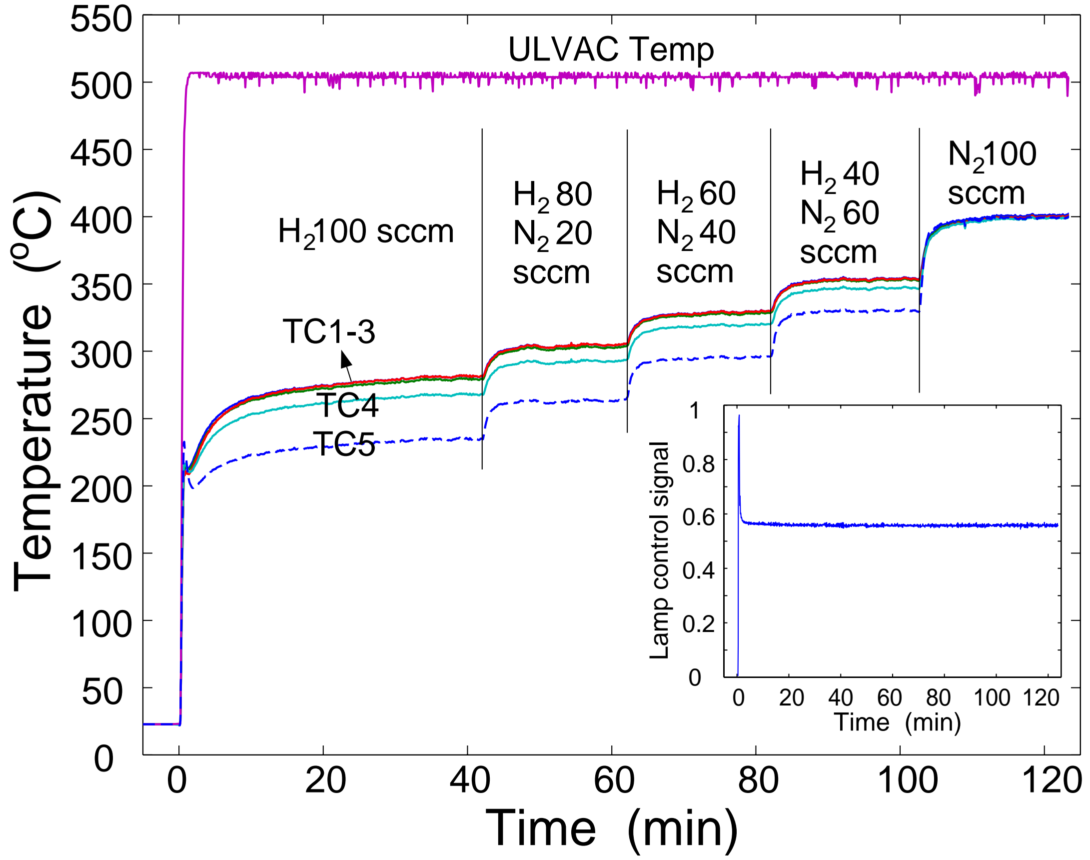

Figure 3.6: The temperature response of the wafer to reactant gas composition variations.

is about six times larger than that of nitrogen at 500 $mTorr$. This gas property-related temperature difference is more significant in the measurement of TC No. 5, where the backside of the wafer contacts reactant gas instead of the quartz susceptor. The temperature deviation of TC No. 4 from TC No. 1-3 is due to the positioning of TC No. 4, which is close to the susceptor edge and is affected by the edge heat loss of the susceptor.

The second experiment was designed to study the effect of gas bulk velocity on wafer temperature, as well as to verify the observations made in the first

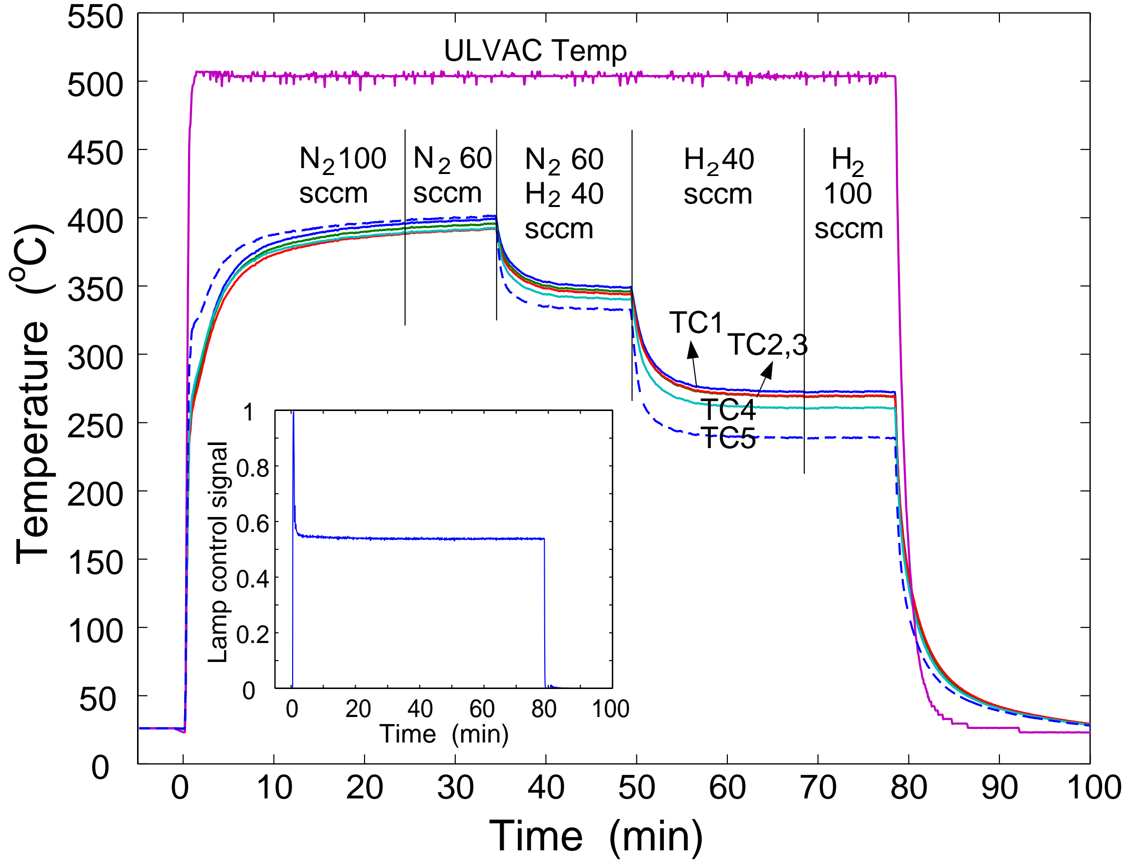

Figure 3.7: The temperature response of the wafer to reactant gas flow rate and composition changes.

experiment. In this experimental sequence, wafer heating was begun in pure nitrogen, and the compositional and total flow rates were changed according to Case 1: 100 *sccm* N_2; Case 2: 60 *sccm* N_2; Case 3: 40 *sccm* H_2/60 *sccm* N_2; Case 4: 40 *sccm* H_2; and Case 5: 100 *sccm* H_2. The experimental results are plotted in Figure 3.7. We note that when the wafer temperature responses are compared for the different flow rates of Case 1 and 2 in pure nitrogen, as well as 4 and 5 in pure hydrogen, only insignificant differences were observed. *This result indicates the gas convective heat transfer modeling terms can be neglected in the*

low pressure processing condition of the ULVAC system. Also, by comparing the temperature measurements of the second experiment to the first one at three different gas compositions (100 *sccm* N_2, 60 *sccm* N_2/40 *sccm* H_2, and 100 *sccm* H_2,) the temperature differences are found to be less than 5 ^oC for pure nitrogen gas flow and are almost equal in the other two cases, demonstrating the repeatability of the experiments.

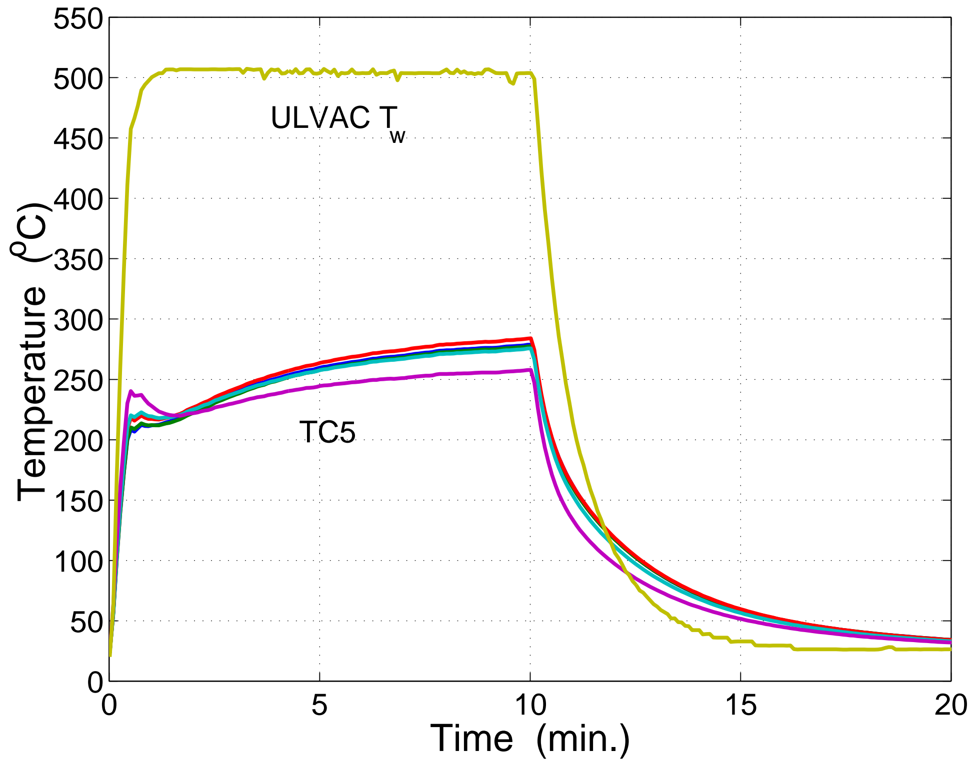

Figure 3.8: The temperature trajectory of a slightly shifted wafer during a process cycle at 0.5 *Torr* and $H_2/N_2 = 40/10$ *sccm*.

In addition, it should be noted that the TC No. 5 measurement, represented as the dashed curve, responded faster during the initial heating ramp phase while the other thermocouples, positioned in the wafer area above the susceptor,

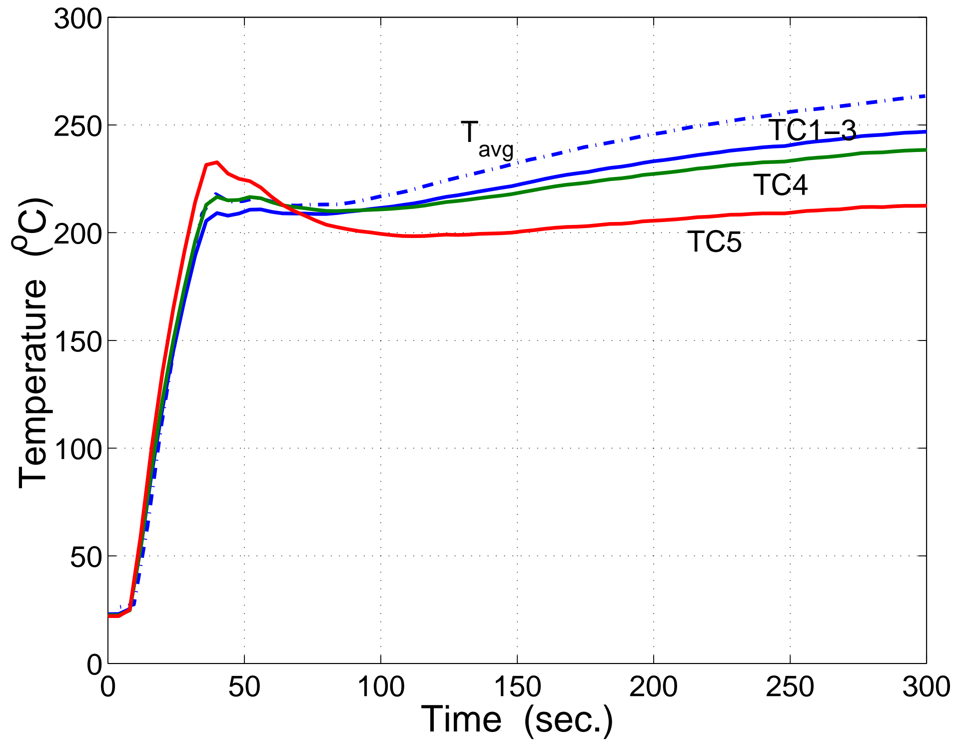

Figure 3.9: Comparison of the wafer temperature in the first five minutes at different gas composition and 0.5 *Torr*. Dash-dotted curve (from Figure 3.15) was found using H_2/N_2 = 40/10 *sccm* and the solid curves (from Figure 3.6) correspond to 100 *sccm* H_2.

showed slower temperature increases due to the additional energy absorbed by the underlying susceptor during the ramp-up phase. This phenomenon was also demonstrated by the wafer temperature response through a single processing cycle, as shown in Figure 3.8, in a hydrogen dominated environment ($H_2/N_2 =$ 40/10 *sccm*). Note that in this experiment, the wafer was only slightly shifted such that the TC4 temperature did not deviate from TC1-3 measurements. Due to the large portion of hydrogen in the gas phase, the temperature measurement

from the thermocouple No. 5 dropped to below the measurements from the remaining thermocouples after the fastest increase during the initial process. This result was consistent with our first experiment and could be explained by the stronger heat conduction from wafer to gas phase in the hydrogen rich environment provided that this effect was larger than the conductive heat transfer from the wafer backside to the susceptor during the soak phase.

It was also interesting to observe the time point when the gas conduction/convection began to impact the wafer temperature during the process. When plotted against the averaged temperature measurements of a well-positioned wafer at $H_2/N_2 = 40/10$ *sccm* in Figure 3.9, the wafer temperature from the first experiment (at 100 *sccm* H_2) showed almost identical response in the first 60 seconds ramp-up period. When the lamp power decreased and approached to a steady-state value (the SP:500 ^{o}C power curve in Figure 3.17) after 60 seconds, the large temperature gradients formed at the wafer/gas interface and the averaged wafer temperature measured in the experiment using the H_2/N_2 gas mixture began to deviate from the TC1-3 measurements obtained using pure hydrogen.

3.4 Wafer Thermal Dynamics

In addition to the steady-state study of wafer temperature responses to process parameters in Section 3.3, the dynamic wafer temperature data provide another viewpoint to observe the interactions between different heat transfer mechanisms. The influence of chamber pressure on wafer temperature is introduced in the first subsection, followed by the development of process windows that provide

constant deposition temperature. The wafer temperature dynamic responses to single and multiple heating cycles are discussed in the last subsection.

3.4.1 Influence of the Chamber Pressure

The chamber pressure was another important factor affecting wafer temperature. Two experiments were conducted at different total chamber pressures and used a 2000 *sccm* H_2 flow to magnify the gas conduction/convection heat transfer effects. Because the experiments were conducted in the I/O mode, the lamp power should have the same profiles due to the identical wafer temperature setpoints at 400 ^{O}C used in both experiments (the lamp control signal during these experiments were not recorded). The experimental results at both 0.17 and 0.5 $Torr$ are presented in Figure 3.10 and the thermocouple wafer measurements are plotted together in Figure 3.11 for comparison.

The influence of the chamber pressure were demonstrated by the lower overall wafer temperature at the higher pressure level of 0.5 $Torr$. The larger amount of energy lost from the wafer/gas conductive/connective heat transfer was believed to be responsible for the wafer temperature reduction at higher pressure because the lamp radiation should be the same for identical temperature setpoints in the I/O operation mode. At the lower pressure of 0.17 $Torr$, the wafer temperature showed a faster increase during the ramp-up phase and slower decrease during temperature ramped-down compared to the responses of wafer temperature at higher pressure, confirming that less energy was removed from the wafer by conduction/convection into the gas phase. This result is consistent with general trend found in the other CVD modeling literature listed in the Chapter 2, for example Lord [108] and Campbell et. al. [109], that the wafer temperature

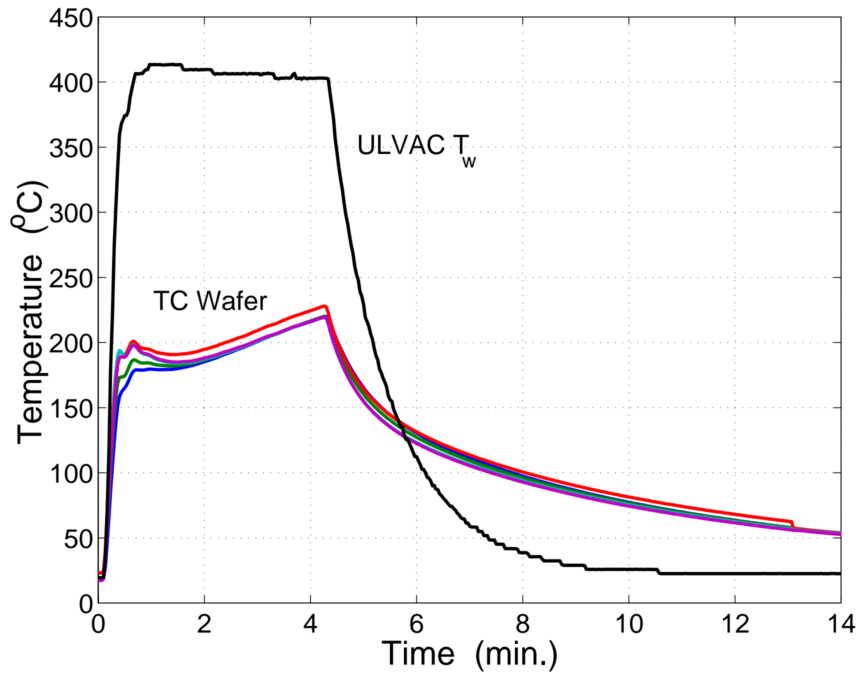

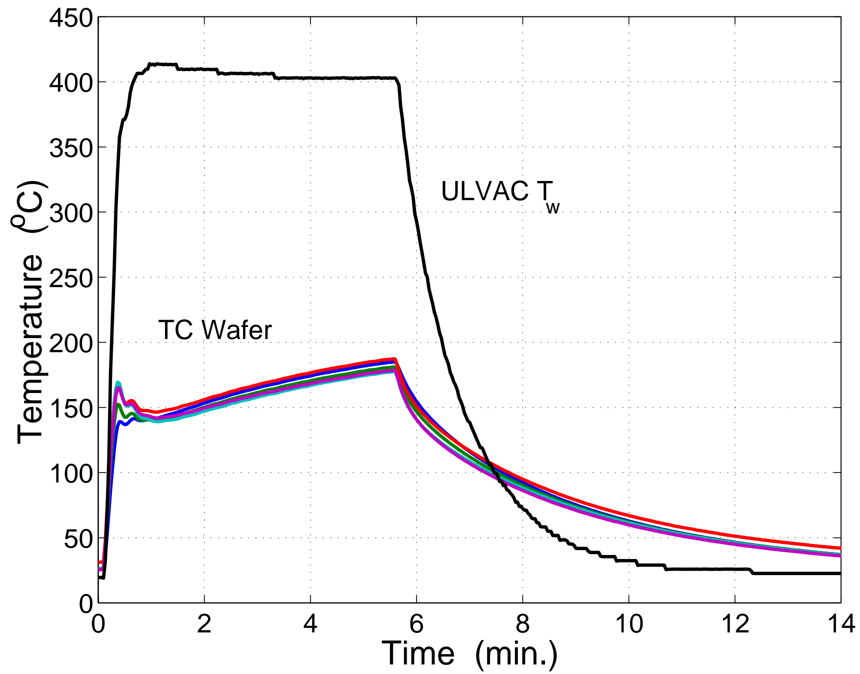

Figure 3.10: The ULVAC adjusted wafer temperature and the five thermocouple measurements of the instrumented wafer during a process cycle at (top) 0.17 $Torr$ and (bottom) 0.5 $Torr$ total chamber pressure in 2000 $sccm$ H_2.

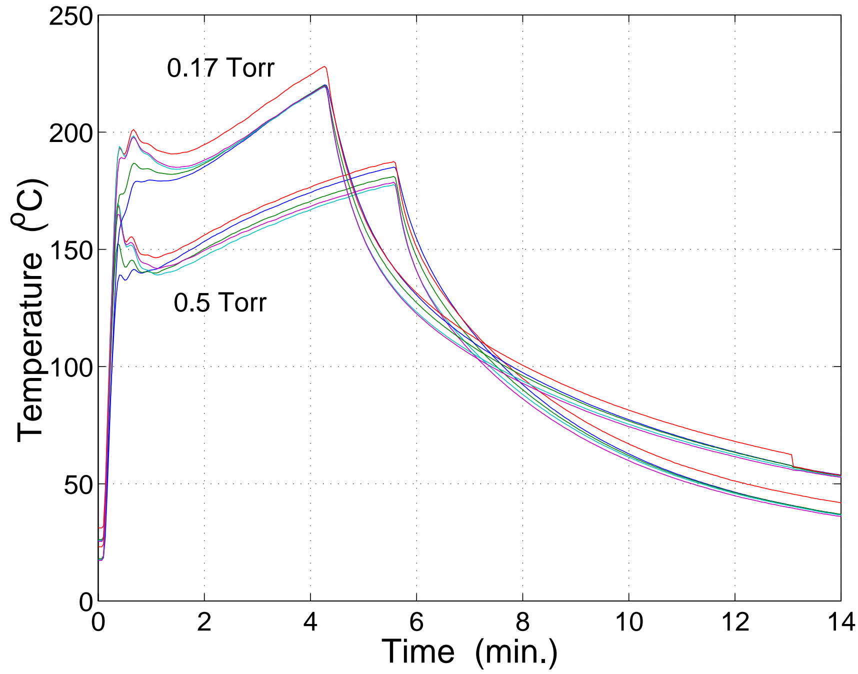

Figure 3.11: Comparison of wafer temperature at different chamber pressure from Figure 3.10.

became lower when the chamber pressure went higher.

3.4.2 Deposition Processing Window

As shown in Figure 1.1, the large temperature difference between the test wafer measurements and the ULVAC adjusted wafer temperature, especially during the ramp-up period would result less tungsten deposition than predicted based on the ULVAC system temperature. This deficiency hindered the process status metrology, for example, the detection of the process end-point using mass spectrometry. One cost-effective solution that did not require changing the equipment parameter settings or designing a new temperature controller was to develop a specific

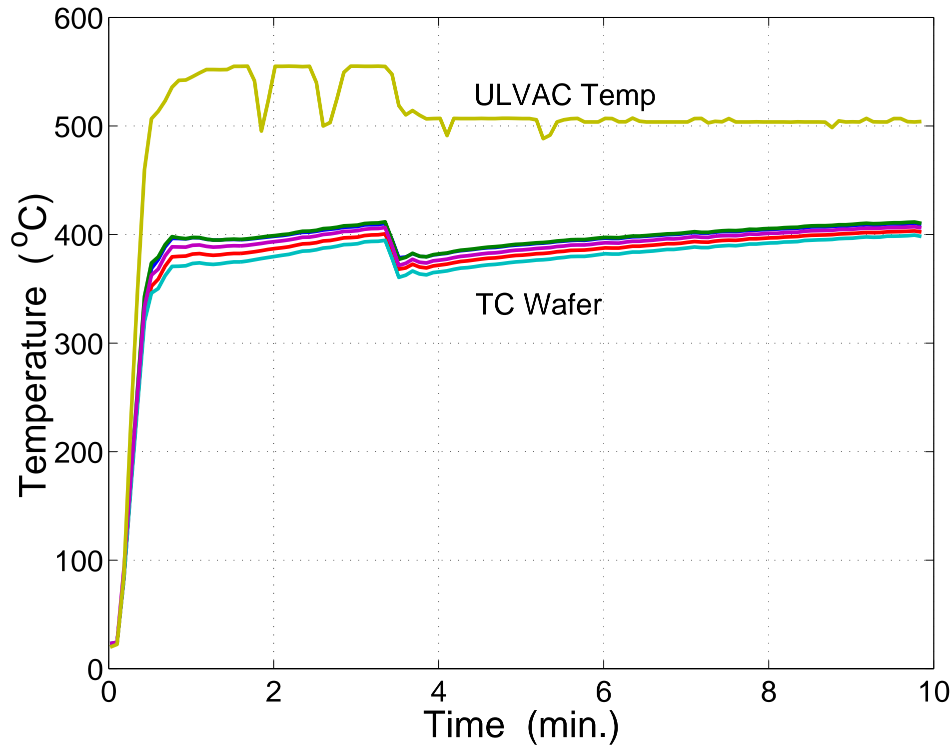

Figure 3.12: Process recipe found by adjusting initial heating sequence at 0.2 $Torr$ and $N_2 = 100$ $sccm$.

process sequence that could provide a five to ten minute processing window during which the desired wafer temperature was achieved and only varied within 5 to 10 degree Kelvin. Thus, the reactant gases are introduced into the chamber during the processing window so that a good relationship between the processing time and the total deposited film weight could be developed.

Two such processing recipes were developed and plotted in Figures 3.12 and 3.13 along with a power profile for the second recipe. In the first recipe, where the 100 $sccm$ N_2 flow and 0.2 $Torr$ pressure were used, the ULVAC wafer temperature setpoint was kept at 550 ^{o}C for the first three and half minutes to provide more energy before it was reset to 500 ^{o}C for a desired 400 ^{o}C true

wafer temperature process. The wafer temperature was measured to approach the target 400 ^oC after six minutes and had a 4 minute processing window with temperature deviations less than 10 ^oC.

A similar recipe was developed for a process at 0.5 $Torr$ and the gas mixture flow rates of $H_2/N_2 = 40/10$ $sccm$. The initial 550 ^oC heating period lasted for 5 minutes and then the system temperature was reset to 500 ^oC. This produced a relatively constant true wafer temperature profile for tungsten deposition between the sixth to thirteenth minutes. Applications using this recipe in the development of the process monitoring using spectrometer achieved successful results in the work of Gougousi et. al. [31].

3.4.3 Wafer Temperature Response of Single and Multiple Heating Cycles

For our transport model development and verification purposes, a single heating cycle process was conducted at three different system temperature setpoints of 450, 500, and 550 ^oC. The gas flow rates were chosen as $H_2/N_2 = 40/10$ $sccm$ for the comparison of the true process gas mixture of $H_2/WF_6 = 40/10$ $sccm$ used in Gougousi et. al. [31]. The wafer temperature response, along with the ULVAC system temperature, are presented in Figures 3.14, 3.16, and 3.15. To compare the temperature trajectories, we overlapped the temperatures measured at the wafer center as well as the lamp power control signals from these three experiments in Figures 3.17 and 3.18.

All three temperature trajectories showed a "dip" behavior after two initial small "bumps", and continuously increased after the "dip" in each exper-

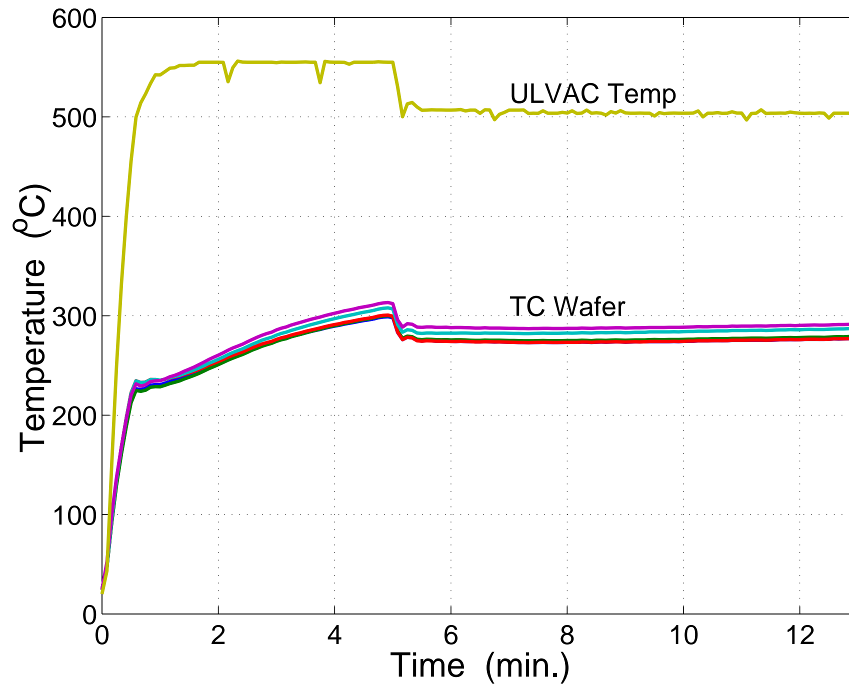

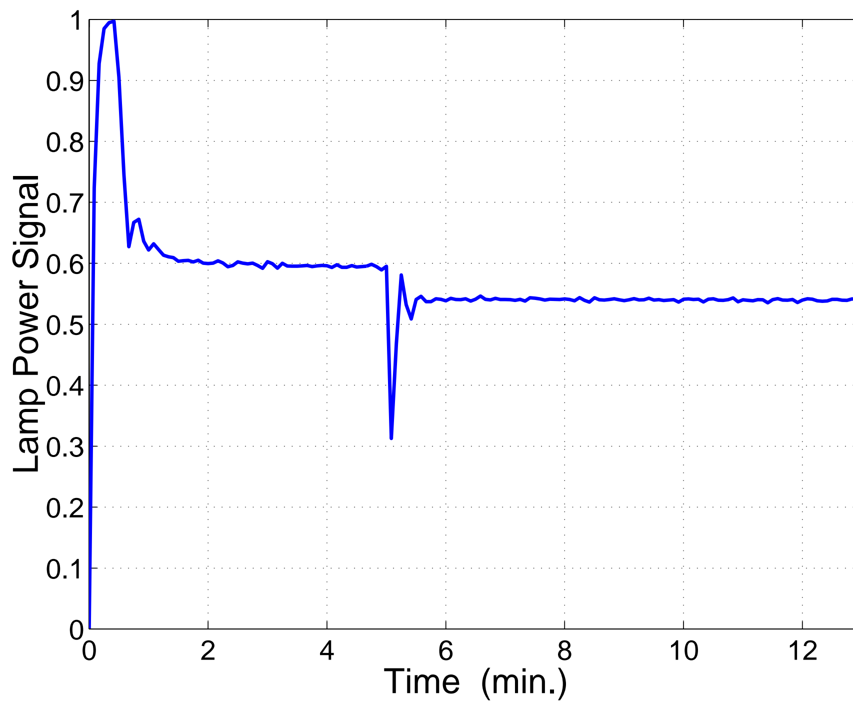

Figure 3.13: Process recipe (top) and corresponding lamp power signal (bottom) found by adjusting initial heating sequence at 0.5 $Torr$ and $H_2/N_2 = 40/10$ $sccm$.

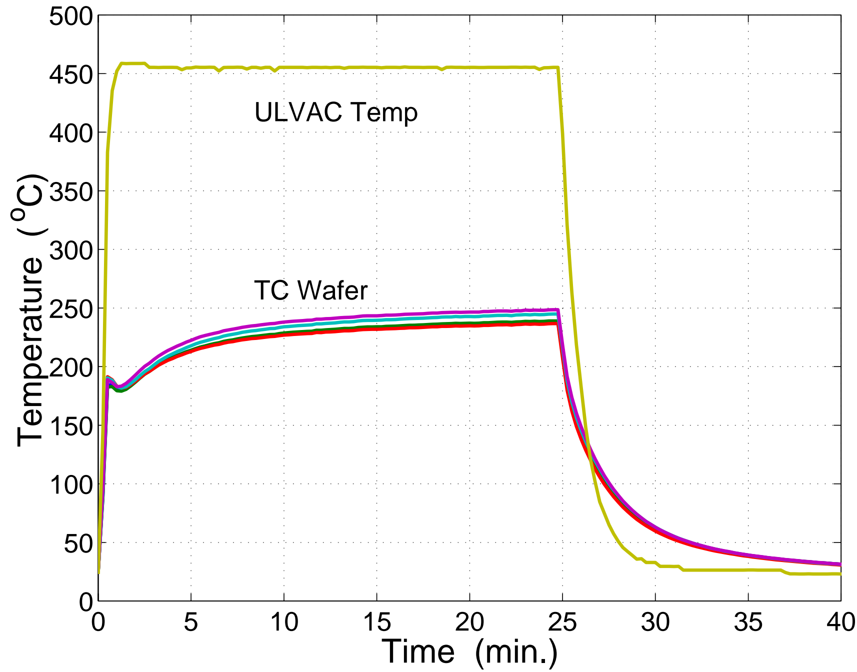

Figure 3.14: The wafer temperature responses to ULVAC temperature setpoints 450 ^{o}C at 0.5 $Torr$ and H_2/N_2 = 40/10 $sccm$.

iment. The two small temperature "bumps" were found to be related to the lamp power variations during the first two minutes of the processes as shown in the Figure 3.18. The lamp power curves in these experiments had similar profiles but differed in the length of the initial high power output periods corresponding to the wafer temperature fast ramp-up. In addition to the direct influence of the lamp radiation on the wafer temperature during the first 60 to 80 seconds, the temperatures measured by the individual thermocouples were observed intercepting each other at about the same time period (see the bottom plot of Figure 3.17), indicating that there was no net thermal conduction across the wafer regions between the corresponding thermocouples at this point in time. Therefore, we believed these initial temperature "bumps" give evidence

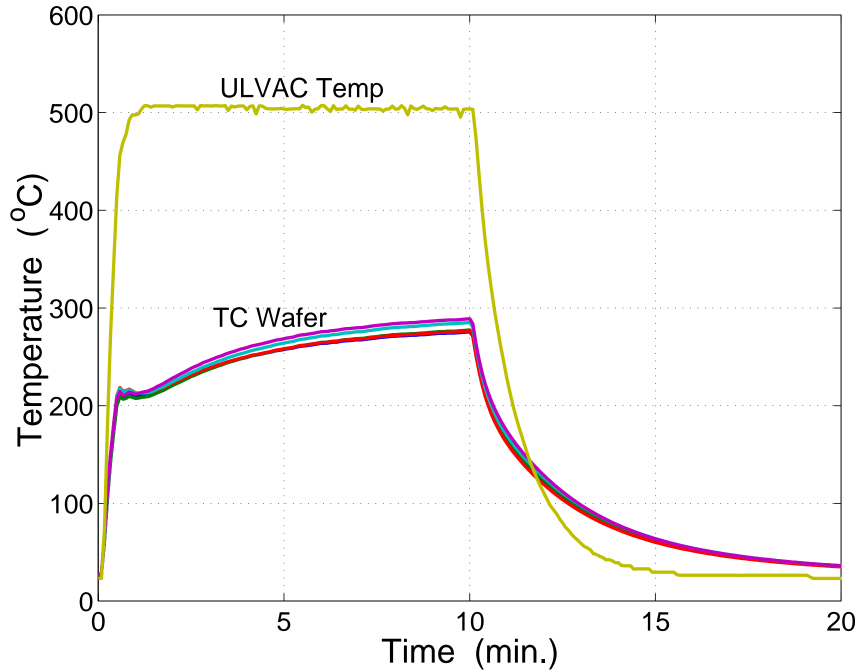

Figure 3.15: The wafer temperature responses to ULVAC temperature setpoints 500 ^{o}C at 0.5 $Torr$ and $H_2/N_2 = 40/10$ $sccm$.

of a fast thermocouple transient phase before reaching a thermal balance with the neighboring regions of the instrumented wafer.

After the first 60 to 80 seconds, the lamp powers approached the corresponding steady state values for each temperature setpoint and the measured temperature corresponding to experiments with higher setpoints increased at faster rates. The showerhead and chamber heating were also thought to contribute to the different temperature ramp-up rates. Because the showerhead also absorbed lamp radiant energy and wafer emission, the longer processing time and the higher wafer temperatures resulted in higher showerhead temperatures and less radiative energy loss from the wafer to the showerhead.

The long term heating provided by the showerhead and reactor chamber

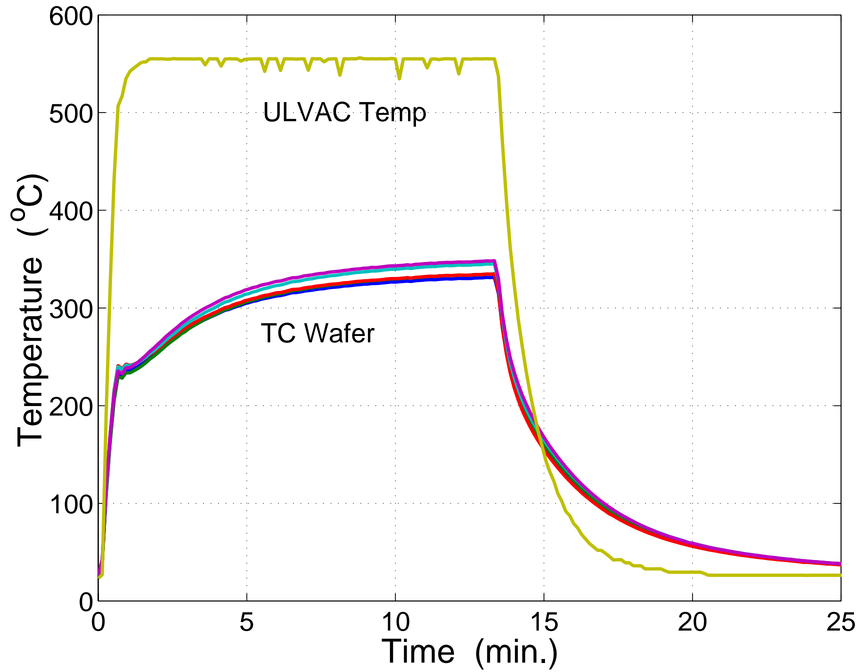

Figure 3.16: The wafer temperature responses to ULVAC temperature setpoints 550 ^{o}C at 0.5 $Torr$ and $H_2/N_2 = 40/10$ $sccm$.

components can be observed in Figure 3.19. The wafer temperature setpoints were programmed to switch between 450 and 550 ^{o}C every four minutes after the initial ramp-up period. The maximum and minimum temperature of the alternating ramp up and down processes were found to gradually increase in time and showed the same increasing rates when the experimental data from Figures 3.14 and 3.16 are superimposed as in Figure 3.19.

Figure 3.20 presents the wafer temperature response in a similar multiple heating cycles experiment. Unlike the experiment conducted in Figure 3.19, the temperature setpoints were reset to 0 ^{o}C for the ramp-down phases and the lamp power was shut down during those periods. This process recipe provided less lamp heating to the showerhead and was shown in the insignificant long-

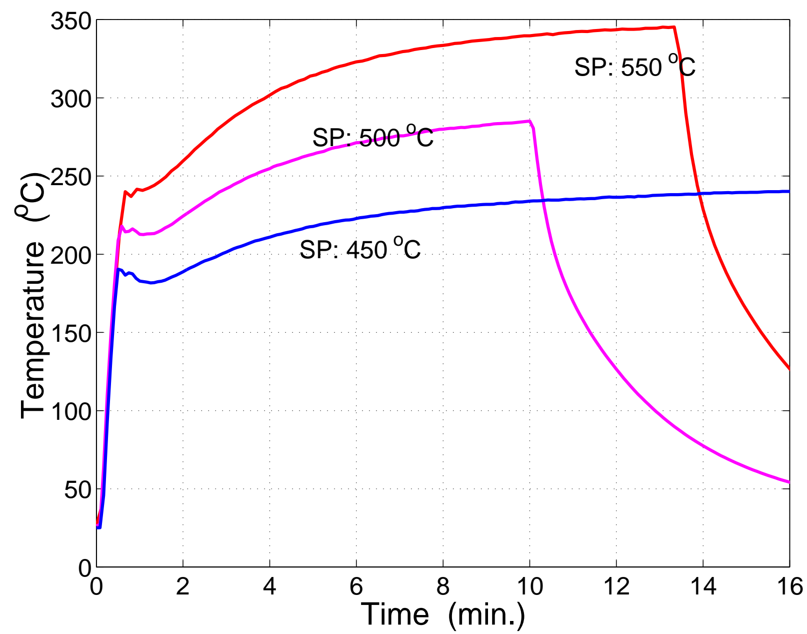

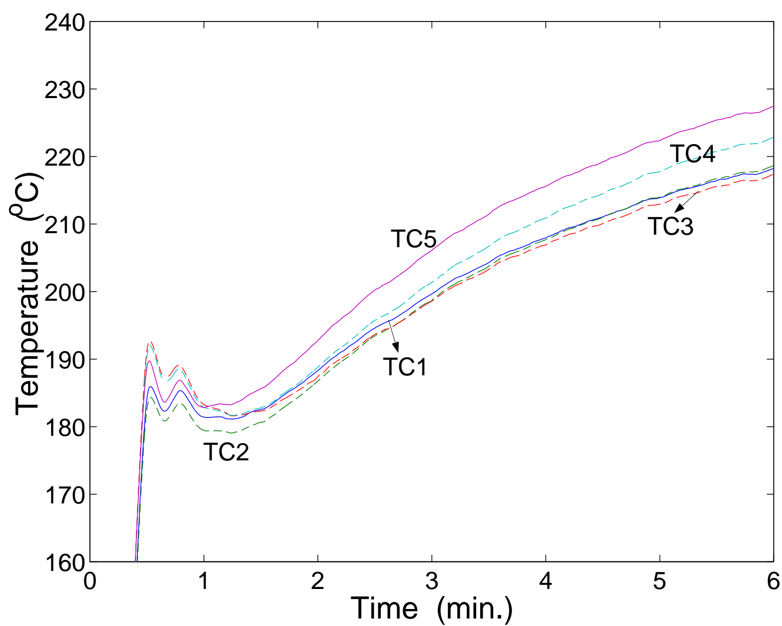

Figure 3.17: (Top) The TC wafer temperature responses to three different temperature setpoints at 0.5 $Torr$ and $H_2/N_2 = 40/10$ $sccm$. (Bottom) The temperature trajectories of each thermocouple at the beginning of the soak phase for the SP: 500 ^{o}C experiment.

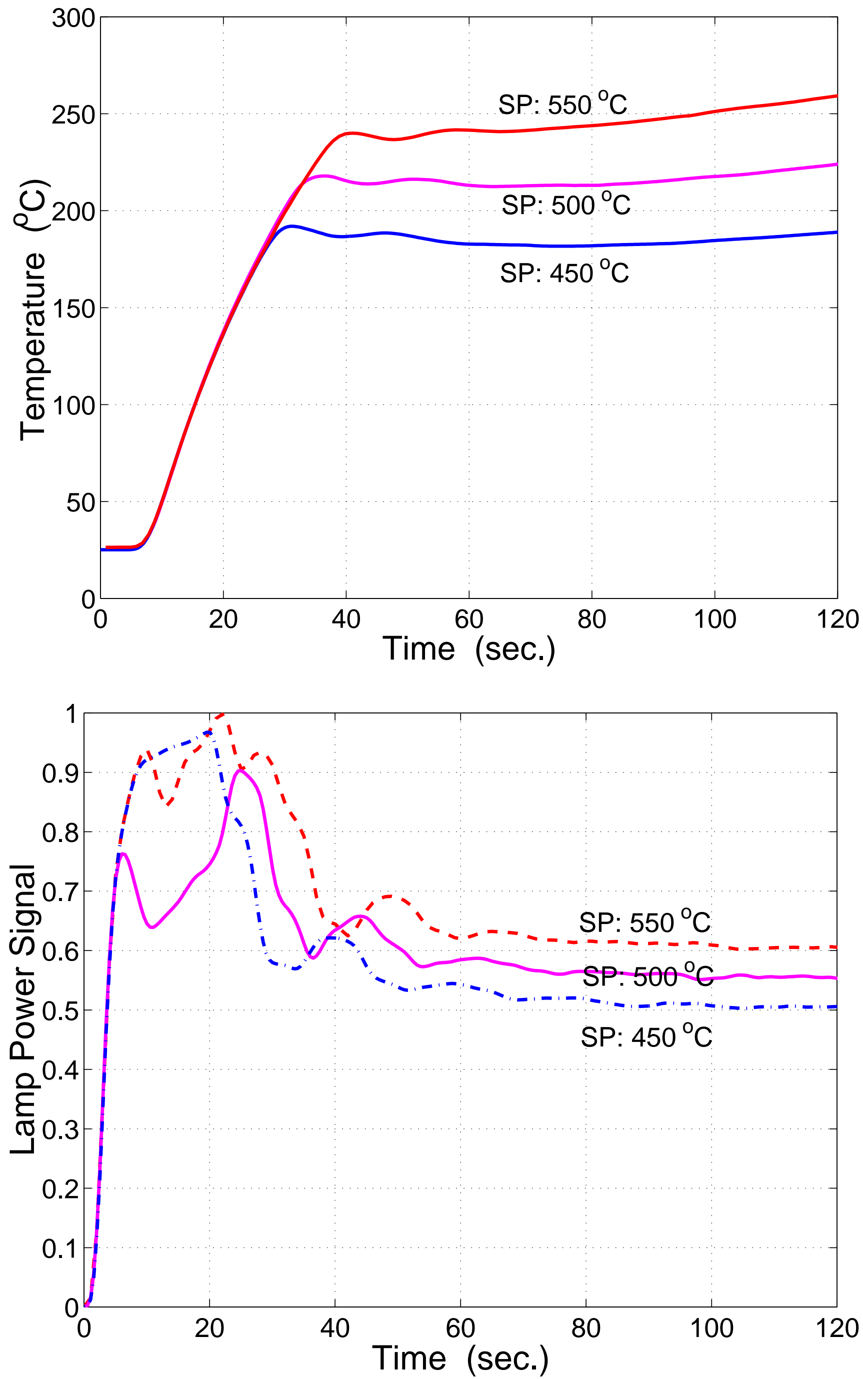

Figure 3.18: The TC wafer temperature responses during the first two minutes to three different temperature setpoints (top) and the corresponding lamp power signal (bottom) at 0.5 $Torr$ and $H_2/N_2 = 40/10$ $sccm$.

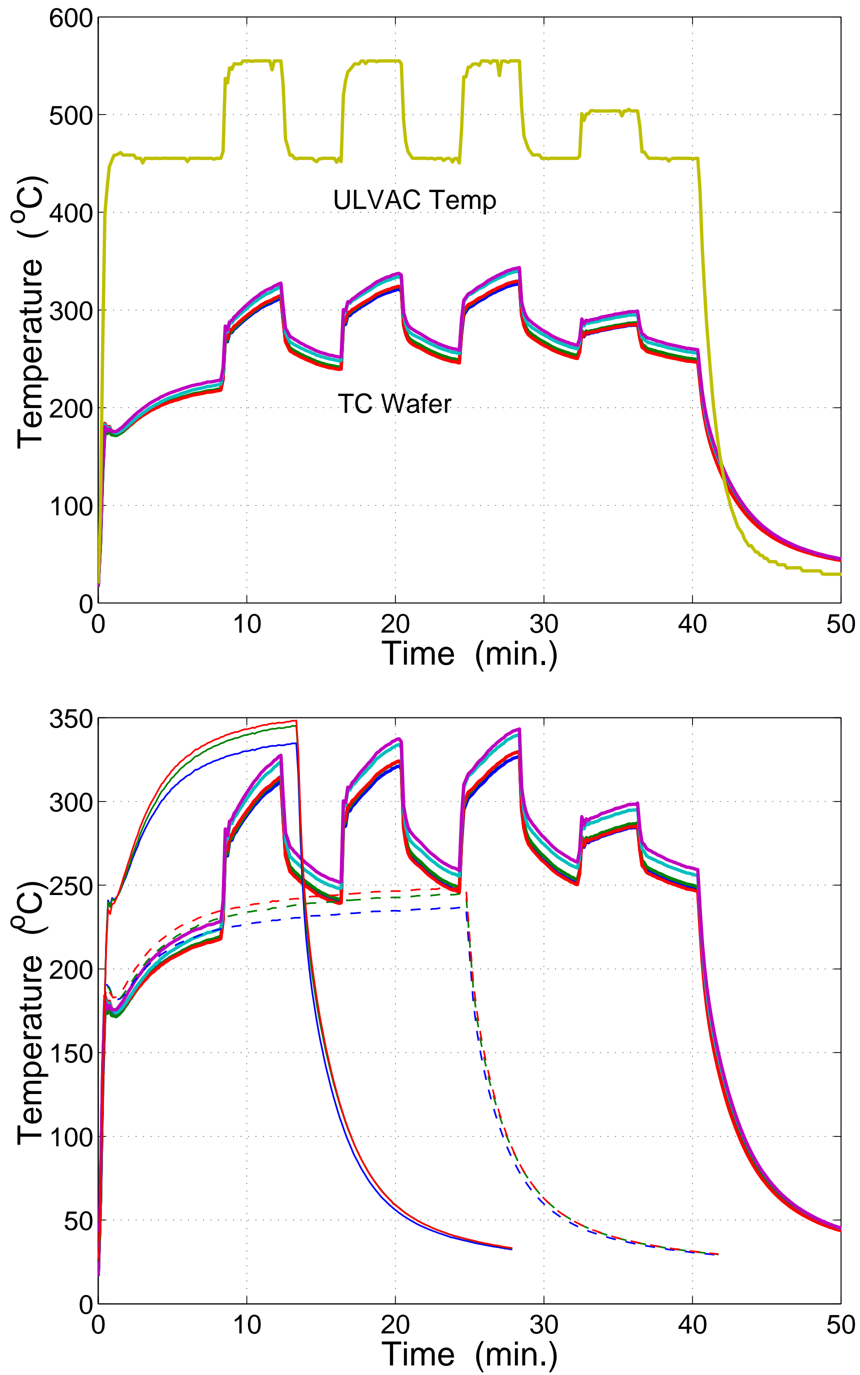

Figure 3.19: The wafer temperature identification trajectory (top) and the long term temperature drift comparison (bottom) at 0.5 $Torr$ and H_2/N_2 = 40/10 $sccm$.

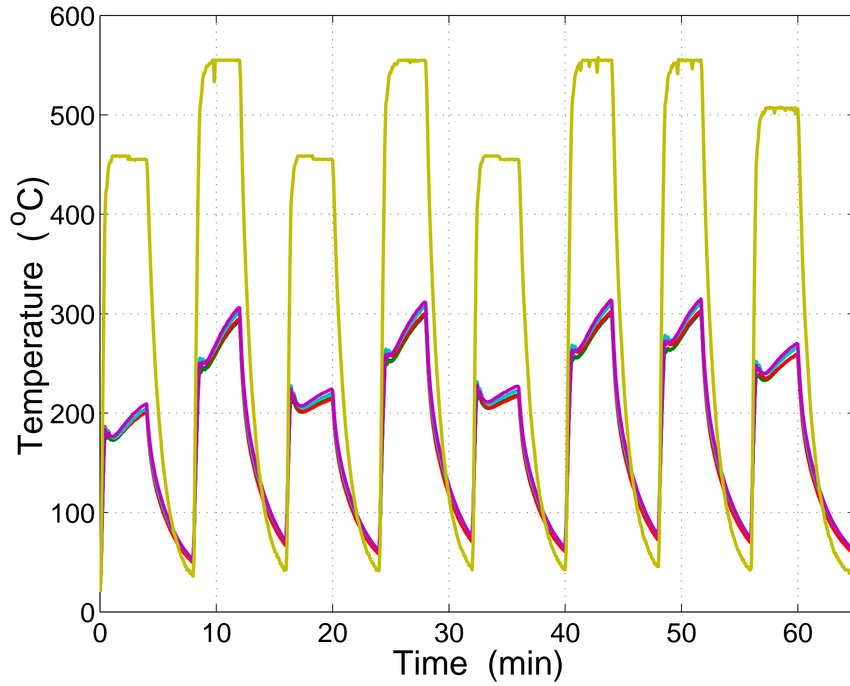

Figure 3.20: The wafer temperature responses to multiple heating cycles for model validation at 0.5 $Torr$ and $H_2/N_2 = 40/10$ $sccm$.

term heating effect where only small differences were observed between the peak temperature values.

Chapter 4

Numerical Solution Procedures

This chapter addresses the numerical solution techniques used to solve the boundary value problems (BVPs) describing the CVD reactor transport model. In general, a set of partial differential equations (PDEs) is formulated to describe the time evolution and/or the spatial distribution of the states in CVD systems. To solve these transport equations numerically, appropriate spatial discretization methods are needed to transform (semi-discretize) the PDEs into sets of ordinary differential equations (ODEs) and/or algebra equations (AEs), and then the resulting equations can be solved by the time integration methods or the Newton-Raphason method. Global weighted residual methods are adopted in this study to perform the discretization and a MATLAB-based toolbox, MWR-tools [110, 111, 112, 113], developed at the University of Maryland by Dr. Adomaitis et. al. is used for the numerical implementation of the weighted residual methods. The introduction of the method of weighted residuals and MWR-tools are presented in Sections 4.1 and 4.2, respectively. It should be noted that weighted residual methods are used both for spatial discretizations and

collocation-based time integration.

A subset of the system dependent parameter values can only be determined by fitting the experimental data to the modeling equations. The parameter estimation is formulated as a nonlinear least-squares problem in this research and the Gauss-Newton method is implemented to estimate the parameter values; they are introduced in Section 4.3.

4.1 Introduction to Method of Weighted Residuals

The method of weighted residuals (MWR) consists of methods for approximating the physics-based partial differential equation models. The solution is first approximated by a finite sum of trial functions, the combination of which approximately satisfies the governing equation and the boundary conditions. The *residual*, or the solution discretization error arises because the truncated expansion does not exactly satisfy either the equation itself or the imposed conditions on the boundaries. Different test functions are used to minimize the residual with respect to a suitable norm to ensure the approximate solution converges to the differential equation. There are two main issues to be determined when applying the weighted residual methods: which truncated sequence should be chosen for the trial functions; and what kind test functions should be employed, or equivalently, how should the expansion coefficients of the trial functions be determined. The basic principles of the computational method are summarized as follows. For details and the underlying theories, see Fletcher [114], Gottlieb and Orszag [115], MacCluer [116], or Fornberg [117].

Consider the following partial differential equation describing a physical model

$$\frac{\partial v}{\partial t} = L(v) + S(v, t)$$

with the initial and boundary condition

$$\begin{aligned} v(0, x) &= v_0 \\ M(t, 1) &= 0 \end{aligned}$$

where L is some differential operator and S is the source term. The general solution procedure begins by approximating the solution $v(x, t)$ as a sum $u(x, t)$ of basis functions, or trial functions ϕ_k:

$$u(t, x) = \sum_{k=0}^{K} a_k(t)\phi_k(x)$$

where t and x represent the time and spatial variable, respectively. In the case of time-independent problem, $v(x)$ is approximated by $u(x)$ and a_k.

There is a wide variety of trial functions ϕ_k from which to choose. Finite-difference [118, 119], finite-volume [119], and finite-element [114, 120] methods use local basis functions as trial functions that define the function values at each grid point, control volume, and element, respectively. The MWR methods implemented in this research are distinguished from those local basis functions-based discretization schemes by the use of globally based trial functions, such as polynomials (e.g. Chebyshev), sinusoidal functions (e.g. Fourier series), Bessel functions, and Legendre functions. A summary of each of these orthogonal function sequences can be found in Funaro [121].

Because the choice of the trial functions is usually problem-dependent, the generic orthogonal functions are not necessarily the optimal selection for a particular set of equations and boundary conditions. Therefore, techniques used

to find an optimal basis (the emperical eigenfunctions) have been developed based on statistical theories such as proper orthogonal decomposition (POD) or Karhunen-Loéve expansion [122, 123, 124, 125, 126] and balanced realizations [86].

Substituting the approximated solution u into the governing equation and boundary condition define the residuals $\mathcal{R}$ and $\mathcal{R}_{\partial\Omega}$, respectively,

$$\begin{aligned}\mathcal{R} &= \frac{\partial u}{\partial t} - L(u) - S(u,t) \\ \mathcal{R}_{\partial\Omega} &= M(t,1).\end{aligned}$$

These residuals are indications of how successfully the solutions satisfy the mathematical model and, in general, are not equal to zero but are functions of the spatial variables. If the trial functions are constructed such that the boundary residual $\mathcal{R}_{\partial\Omega}$ is satisfied exactly, it is called the interior method. However, if both the equation and boundary condition are not satisfied exactly by the selected trial functions, a supplementary set of trial functions is necessary to satisfy the boundary conditions exactly and is referred to as a mixed method.

The minimization of the residuals is achieved by projecting them onto the selected test functions to yield a set of ordinary differential equations/algebraic equations for time-variant problems or an algebraic equation system for steady-state problems. The resulting ODE and/or AE systems can be solved using time integration schemes such as the Runge-Kutta method or the Newton-Raphason method to find expansion coefficients of the approximated solution. This completes the solution procedure.

The projection procedure can be written as an inner product over the entire

domain if L_2-norm is adopted:

$$\langle \mathcal{R}, w_k \rangle = \int_V \mathcal{R}(x)\, w_k(x)\, dx \qquad k = 0,\, 1,\, \ldots\, ,\, \mathrm{K}$$

where V is the domain of interest and w_k is the test function, or the weighting function. The choice of the test functions is another important implementation issue and distinguishes between several method of weighted residuals schemes, namely, Galerkin, collocation, least-squares, subdomain, and moment versions. A brief review of the first three methods is given as follows and the details can be found in Flecther [114].

- **Galerkin method**

  The test functions are selected from the family of the trial functions.

  $$w_k = \phi_k(x)$$

  The Tau method is used when the trial functions do not satisfy the boundary conditions by construction.

- **Collocation method**

  In this method, the test functions are translated Dirac delta functions centered at the collocation points,

  $$w_k = \delta(x - x_k)$$

  where x_k is the k-th collocation point. The property of the Dirac delta function leads to

  $$\int_{x_k^-}^{x_k^+} f(x)\, \delta(x - x_k)\, dx = f(x_k).$$

  In the orthogonal collocation method, the collocation points are chosen as the roots of the highest-order trial function.

- **Least-Squares method**

  The weighting function is derived from the minimization of the L_2-norm of the square of residual with respect to each expansion mode coefficient, i.e.,

$$\begin{aligned} \frac{d \parallel R \parallel_2^2}{da_k} &= \frac{d}{da_k} \int_V R^2 dx \\ &= \int_V 2R \frac{dR}{da_k} dx \end{aligned}$$

$$w_k = \frac{\partial \mathcal{R}}{\partial a_k}.$$

  The least-squares projection is the optimal discretization technique for a given trial function expansion and is better suited to solving steady-state problems.

4.2 MWRtools

MWRtools [110, 111, 112, 113] is a set of MATLAB v5.x based functions developed for solving boundary-value problems using globally defined trial functions and weighted residual methods (MWR). The numerical techniques form a computational toolbox consisting of a common set of numerical tools for implementing the different MWR techniques used in the numerical solution and analysis of systems described by ordinary and partial differential equations.

The first version of the MWRtools focused on identifying the common computational modules which form a one-to-one correspondence between the MWRtools functions and the elemental steps of an MWR solution procedure [110, 111, 112, 113]. However, it only has limited computational capability to solve problems described in two or three dimensions. Improvements are made in the

following version that strongly enhance the ability to compute the higher dimensional projections and solve the heterogeneous systems, defined by multiple boundary value problems (BVPs) on one or more spatial domains [127]. This enhancement is made by implementing the object-oriented programming concepts where variables and methods are encapsulated in the hierarchical classes. The introduction of the operator/function overloading provides the computational flexibility to work with variables of different data structures and is the major reason to accomplish efficient computations for multiple dimensional systems.

A collocation method based ODE/AE system time integrator is also developed and is externally integrated with a Gauss-Newton method based minimization function for parameter estimation applications. Although there is not a single function designed specifically for model reduction purposes, the proper orthogonal decomposition and other model reduction algorithms can be implemented by some combination of the individual functions.

The current MWRtools functions are listed in Tables 4.2, 4.2, and 4.2. Three object classes, Loper, Tfun, and Sfield, are defined with individual constructors to process methods provided by the corresponding linear operator, trial function, and scalar field classes.

Table 4.1: List of current MWRtools functions used for initialization, collocation methods, and solution reconstruction.

MWR Elements	[Output] =	`Function`	(Required Input,	Optional Input)
Specify geometry	$\hat{\mathbf{x}}, \hat{\mathbf{w}}, \hat{\mathbf{A}}, \hat{\mathbf{B}}, \hat{\mathbf{Q}}$	`pd`	'geom', M	
Trial functions	Ψ	`gdf`	$\hat{x}$, 'f(x̂,p)', 'x̂'	{'p', $\mathbf{p}$}
Eigenfunctions	λ, Ψ, Φ,	`sl`	'geom', $\hat{\mathbf{A}}$, $\hat{\mathbf{x}}$, ...	$\hat{\mathbf{v}}$, $\hat{\mathbf{p}}$, $\hat{\mathbf{q}}$, $\hat{\mathbf{g}}$, ϵ, ...
	$\mathbf{w_{ef}}$, $\mathbf{w_{ad}}$		a, b, c, d, $\hat{\mathbf{w}}$	a_1, b_1, c_0, d_0
Collocation methods	$\mathbf{Q}, \mathbf{w}, \mathbf{A}, \mathbf{B}$	`colmat`	$\Phi, \mathbf{x}, \hat{\mathbf{x}}, \hat{\mathbf{w}}, \hat{\mathbf{A}}$	$\hat{\mathbf{B}}$
	$\mathbf{x}$	`colpts`	$\Phi, \hat{\mathbf{x}}$	$\hat{\mathbf{w}}, \mathbf{x_p}, \hat{\mathbf{A}}$
Solution reconstruction	$\mathbf{T}$	`sp2pd`	$\mathbf{A}$, Φ	
Spectral filter	$\mathbf{s}$	`fsf`	μ, N	

Table 4.2: List of the MWR functions especially designed for solving problems defined in higher dimensions.

MWR Elements	[Output] =	`Function`	(Input)
Projection	$\mathbf{I_p}$	`wip`	$\hat{\mathbf{F}}$, $\hat{\mathbf{G}}$, $\hat{\mathbf{w}}$
Orthogonalization	Φ	`gs`	$\hat{\Psi}$, $\hat{\mathbf{w}}$
Array multiplication	$\mathbf{C}$	`mprod`	$\mathbf{A}$, $\mathbf{B}$, p, q, r
$\mathbf{Ax} = \mathbf{B}$ Solver	$\mathbf{x}$	`msolve`	$\mathbf{A}$, b
Diagonal array	$\mathbf{B}$	`mdiag`	$\mathbf{A}$
Extract elements	$\mathbf{B}$	`extract`	$\mathbf{A}$, n
Jacobian array	$\mathbf{J}$	`makejacobian`	$\mathbf{T}$,$\mathbf{Jc}$
Operator multiplication	$\mathbf{y}$	`moper`	$\mathbf{A}$,$\mathbf{f}$,dir
Term-by-term sums	$\mathbf{C}$	`msum`	$\mathbf{A}$,$\mathbf{B}$
ODE/AE solver	[**tout**,**Y**,**Q**, **tfine**,**phi**,**dYdp**]	`odaepc`	fn, **tint**,**y0**,**param**, **ffun**,**C**,**T**,M

Table 4.3: List of classes in MWRtools and their corresponding methods.

Classes	*Methods*	[Output] =	`Method`	(Input)
Loper	Constructor	L	`loper`	v, dir
	Get fields	p, q	`get`	L
	Obj. multiplication	c	`mtimes`	L , B
Tfun	Constructor	F	`tfun`	t, dir, w
	Get fields	p, q, w	`get`	F
	tfun times loper	C	`tfunset`	F , L
	Obj. multiplication	c	`mtimes`	a , F
	Obj. dot product	S	`times`	a , F
	Inner product	c	`wip`	A , F
Sfield	Constructor	S	`sfield`	A, dir
	Get fields	p, q	`get`	S
	Inner product	c	`wip`	S, F

4.3 Introduction to Nonlinear Least-Squares Parameter Estimation

The nonlinear least squares (NLS) problems studied in this research arise from the need to estimate some of the CVD model parameter, where the objective function, defined by the sum of squares of the differences between the experimental data and model predictions, is nonlinear with respect to the parameters instead of the independent variables. The parameter estimation problem gives rise to an overdetermined system that has more observations (equations) than the parameters (variables) to be estimated. When optimization proceeds, the Jacobian matrix, the first derivatives of functions with respect to the parameters, is not a square matrix due to the overdetermined system and several optimization techniques that require square Jacobian matrix fail to apply.

There are two different approaches to solve the NLS problems based on the Newton method: the small-residual and the large-residual methods [128]. They are given these particular names because these algorithms are more efficient when small or large function residuals exist, respectively. In the small-residual algorithms, the second derivatives of objective functions are approximated by ignoring the second-order derivatives terms. The large-residual algorithms retain the second-order derivative terms but approximate them using schemes such as the Quasi-Newton updating formula. In this introduction, we only introduce the Gauss-Newton method. The detailed algorithms on nonlinear optimizations are summarized in Scales [128] or Bard [129].

4.3.1 Nonlinear Least Squares Problem Formulation and the Newton Method

The general form of a least squares problem formulated for parameter estimation is as follows,

$$\begin{aligned} & \min_{\mathbf{p}} ||\mathbf{T}(t) - \hat{\mathbf{T}}(t;\mathbf{p})||_2^2 \\ \approx & \min_{\mathbf{p}} \sum_{i=1}^{M} w_i \ \left[T(t_i) - \hat{T}(t_i;\mathbf{p})\right]^2 \\ \approx & \min_{\mathbf{p}} F(\mathbf{p}) \\ = & \min_{\mathbf{p}} \mathbf{f}(\mathbf{p})^T \ \mathbf{W} \ \mathbf{f}(\mathbf{p}) \end{aligned} \tag{4.1}$$

where $\mathbf{p}$ is parameter vector to be estimated, $\mathbf{f}(\mathbf{p}) = [f_1, f_2, \ldots, f_M]^T$, and $\mathbf{W}$ is the weighting matrix. In the ordinary least squares method, $\mathbf{W} = \mathbf{I}$. The function f_i, in general, represents the difference or the error between the expected or predicted value ($\hat{\mathbf{T}}$) and the measurement ($\mathbf{T}$):

$$f_i(\mathbf{p}) = e_i(\mathbf{x}) = T(t_i) - \hat{T}(t_i;\mathbf{p})$$

and t_i is the independent variable such as time.

Applying the Newton method to NLS objective function F in Equation (4.1), we obtain the iterative solution procedure

$$\begin{aligned} (\mathbf{J}_k^T\mathbf{J}_k + \mathbf{S}_k)\boldsymbol{\Delta}\mathbf{p}_k &= -\mathbf{J}_k^T\mathbf{f}_k \\ \mathbf{p}_{k+1} &= \mathbf{p}_k + \boldsymbol{\Delta}\mathbf{p}_k \end{aligned} \tag{4.2}$$

where the first and second derivatives $\mathbf{g}(\mathbf{p})$ and $\mathbf{G}(\mathbf{p})$, the Jacobian matrix $\mathbf{J}$,

and the matrices $\mathbf{T}, \mathbf{S}$ are defined as

$$\begin{aligned}
g_j &= 2\sum_{i=1}^{M} f_i \frac{\partial f_i}{\partial p_j} \quad \text{or} \quad \mathbf{g}(\mathbf{p}) = 2\mathbf{J}^T(\mathbf{p})\mathbf{f}(\mathbf{p}) \\
J_{ij} &= \frac{\partial f_i}{\partial p_j} \\
G_{kj} &= 2\sum_{i=1}^{M} \left[\frac{\partial f_i}{\partial p_k}\frac{\partial f_i}{\partial p_j} + f_i \frac{\partial^2 f_i}{\partial p_k \partial p_j} \right] \quad \text{or} \\
\mathbf{G}(\mathbf{p}) &= 2\mathbf{J}^T(\mathbf{p})\mathbf{J}(\mathbf{p}) + 2\sum_{i=1}^{M} f_i(\mathbf{p})\mathbf{T}_i(\mathbf{p}) \\
&= 2\mathbf{J}^T(\mathbf{p})\mathbf{J}(\mathbf{p}) + 2\mathbf{S}(\mathbf{p}) \\
\mathbf{T}_i(\mathbf{p}) &= \boldsymbol{\nabla}^2 f_i(\mathbf{p}) \\
\mathbf{S}(\mathbf{p}) &= \sum_{i=1}^{M} f_i(\mathbf{p})\mathbf{T}_i(\mathbf{p}).
\end{aligned}$$

The main problems associated with using the Newton method are its sometimes unpredictable convergence properties and the need to compute the second-order derivatives. Regarding convergence, because the objective function $F(\mathbf{p})$, in general, is not a quadratic function, the Newton algorithm will not reach the minimum in a single step. Moreover, outside the neighborhood of the minimum the Hessian matrix $\mathbf{G}(\mathbf{p})$ is not necessarily positive definite and thus the convergence is not guaranteed. Computationally, the Newton method requires evaluation of the second-order derivative $\mathbf{S}_k$ and sometimes this is numerically impractical because of the lack of analytical expressions or the computational expanse of updating $\mathbf{S}_k$ in every iteration in the complicated parameter estimation problems [128]. Therefore, the Newton method-based algorithms such as the Gauss-Newton method have been developed to neglect the second-order derivative $\mathbf{S}_k$ when either it is very small compared to the product of Jacobians or the error $f_i(\mathbf{p})$ is very small [130]. This approach that ignores the second-order terms has also been reported advantageous for parameter estimation when

the models fit badly or the data are contaminated by outlier points, a case where the second-order terms tend to destabilize the numerical procedure [130].

4.3.2 The Gauss-Newton Method

The Gauss-Newton method is one of the small-residual algorithms that approximates the Hessian matrix only with the first-order derivatives and neglects the second-order term $\mathbf{S}_k$ completely. Derived from Equation (4.2), it can be written as

$$\begin{aligned} \mathbf{J}_k^T \mathbf{J}_k \boldsymbol{\Delta} \mathbf{p}_k &= -\mathbf{J}_k^T \mathbf{f}_k \\ \mathbf{p}_{k+1} &= \mathbf{p}_k + \boldsymbol{\Delta} \mathbf{p}_k. \end{aligned} \tag{4.3}$$

The Gauss-Newton method can be implemented to a broader range of problems than the Newton scheme because the product of the Jacobians, $\mathbf{J}_k^T \mathbf{J}_k$, is always positive semi-definite, and it becomes the actual Newton scheme in the neighborhood of the minimum, achieving a quadratic convergence rate. However, away from the minimum, the objective function value $F(\mathbf{p})$ is not necessarily reduced during each iteration because the step size (=1) maybe too large due to the second-order term approximations. The convergence rate thus can be enhanced by controlling the step size h with algorithms such as doubling and halving or Box-Kanemasu (interpolation-extrapolation) method [131] in the updating equation $\mathbf{p}_{k+1} = \mathbf{p}_k + h \boldsymbol{\Delta} \mathbf{p}_k$.

When a large residual is present in the problem where the objective function value $F(\mathbf{p}^*)$ is substantially larger than zero at the minimum $\mathbf{p}^*$, the error functions $\mathbf{f}(\mathbf{p}^*)$ are not zero. The rank deficiency is expected in the Jacobian

matrix $\mathbf{J}(\mathbf{p}^*)$, or equivalently, $\mathbf{J}^T(\mathbf{p}^*)\mathbf{J}(\mathbf{p}^*)$ is singular because the first derivative $\mathbf{g}(\mathbf{p}^*) = \mathbf{J}^T(\mathbf{p}^*)\mathbf{f}(\mathbf{p}^*)$ should be zero at the minimum $\mathbf{p}^*$ [128]. When this large-residual case occurs, the convergence rate will become slow for the Gauss-Newton method discussed above. One should switch to the singular value decomposition to decompose the Jacobian and solve the problem as

$$\begin{aligned} \mathbf{J}_k &= \mathbf{U}_k \boldsymbol{\Sigma}_k \mathbf{V}_k^T \\ \boldsymbol{\Delta}\mathbf{p}_k &= -\mathbf{V}_k \boldsymbol{\Sigma}_k^{-1} \mathbf{U}_k^T \mathbf{f}_k. \end{aligned} \tag{4.4}$$

The MWRtools function `gnstep.m` is written to perform the Gauss-Newton method for the parameter estimation problems used in this research.

Chapter 5

Simulation Results

In this chapter we present several model simulation results and their comparisons with the experimental data provided in Chapter 2. A steady-state wafer temperature model is constructed in Section 5.1 to study the gas composition effects on wafer temperature and the interactive heat transfer mechanisms between the reactor chamber components. Three dimensional gas flow and temperature fields are solved to provide the information of the energy exchange at the gas/wafer interface and the heat transfer parameters are estimated and validated.

A dynamic wafer temperature simulator is built and tested in Section 5.2. Multiple modeling equations are used to accommodate the different thermal time constants observed in the experimental data. The guide values of several model parameters are identified in a linearized form and serve as the initial guesses in the nonlinear model parameter estimation procedure.

5.1 Influence of Gas Composition on Steady-State Wafer Temperature

To describe the across-wafer temperature variations observed in our experimental data, we use different steady-state modeling approaches for wafer areas located above and beyond the susceptor outer edge. For the wafer region positioned above the susceptor (TC No.1-3), the governing equation (2.7) at steady-state becomes

$$Q_{lamp} + Q_{rad} + Q_{top} + Q_{bot} = 0. \tag{5.1}$$

The value of Q_{top} is computed by numerically differentiating the gas temperature at wafer/gas boundary as described in equation (2.8). Because the wafer is not clamped against the susceptor, there is no real solid-solid contact [89], and therefore an effective heat transfer coefficient h_{eff} is used to approximate the combined heat transfer between wafer backside surface and chamber floor. This empirical, temperature-dependent heat transfer coefficient can be approximated by

$$h_{eff}(T_w) = h_{eff,0} + \alpha_0(T_w - T_{w,N_2}),$$

which includes the nominal heat transfer coefficient $h_{eff,0}$ and constant of proportionality α_0, that must be determined by fitting the experimental data to the model. Modeling the heat transfer in this form is equivalent to the Taylor series expansion of the true function, evaluated at T_{w,N_2}. The wafer thermal conduction term $\Delta_{Z_w}\kappa_w\nabla^2 T_w$ is neglected because the averaged wafer temperature measurement from thermocouples No. 1-3 is used for data analysis. However, this conduction term proves to be small compared to other energy transfer mech-

anisms when estimated for the TC No. 5 location and we should expect even smaller amount of energy conducted for measurement points above the susceptor. Temperature data from thermocouple No. 4 is not considered here because it is affected by the susceptor edge heat transfer.

In the wafer region where thermocouple No. 5 is located, the wafer backside surface is in contact with reactant gas. The steady-state model takes the form

$$Q_{cond} + Q_{lamp} + Q_{rad} + Q_{top} + Q_{bot} = 0. \tag{5.2}$$

Q_{cond} is approximated using finite-difference formula

$$Q_{cond} \approx \Delta_{Z_w} \kappa_w(T_{w,5}) \left[\frac{\overline{T}_{w,1-3} - T_{w,5}}{\Delta_R} - 0 \right] / \Delta_R$$

where Δ_R is the distance between thermocouple No. 5 and the averaged position of thermocouples No. 1-3.

Under low pressure processing conditions, the heat conduction between two parallel solid surfaces is proportional to the molecular mean free path in the gas phase. Because the gap distance between wafer and chamber floor is comparable to the gas molecular mean free path in the ULVAC system, the continuum flow model of the heat transfer must be modified and the correction of heat transfer coefficient is expressed as [89, 42]

$$h_{eff} \approx \frac{\kappa_g}{\Delta_{Z_{w,f}} + 2\beta_{w,f}\lambda} \tag{5.3}$$

where κ_g is the mean thermal conductivity evaluated at $\overline{T}_{w,f} = (T_w + T_f)/2$, $\Delta_{Z_{w,f}}$ is the wafer-floor gap distance, and λ is the mean free path defined by gas mixture molecular weight M, viscosity, and pressure p [96] as

$$\lambda = 3.2 \frac{\mu}{p} \left(\frac{R\overline{T}_{w,f}}{2\pi M} \right)^{1/2}.$$

The constant $\beta_{w,f}$ is defined by thermal accommodation coefficient α and the ratio of specific heats $\gamma = C_p/C_v$ at constant pressure and volume [89, 42]

$$\beta_{w,f} = \frac{2-\alpha}{\alpha} \frac{9\gamma - 5}{2\gamma + 2},$$

and is on the order of unity.

5.1.1 Parameter Estimation

There are several parameters in the wafer energy balance model for which values are difficult to compute accurately using published correlations or other *a priori* approaches. The lamp radiant flux intensity at the wafer surface, Q_{lp}, depends on the true emissive power of the heating lamps, the geometry of the reactor and chamber walls, and the adsorption characteristics of the quartz showerhead window. The upper limit of Q_{lp} of the ULVAC system, however, can be estimated by dividing the product of measured maximum lamp current and voltage by an approximated 0.3 m diameter circular area of the chamber floor.

The thermal accommodation coefficient α, used to define the constant $\beta_{w,f}$ in the conductive flux relation for the thin gas gap between the wafer and chamber floor, can deviate from the theoretical value calculated using the hard sphere molecular collision assumption [89]. Here we take the approach of Kleijn and Werner [42] to estimate the value of $\beta_{w,f}$ instead. As discussed in the previous section, the temperature dependent heat transfer coefficient h_{eff} must also be identified by using experimental measurement to accommodate the overall heat transfer coefficient that combines thermal conduction from wafer to susceptor, thermal conduction across the susceptor, and reactant gas thermal conduction between susceptor and chamber floor. The representative guide values of the

system parameters to be estimated are listed in Table 5.1 for reference.

5.1.2 Solution Procedure

To estimate the system parameters Q_{lp}, $\beta_{w,f}$, $h_{eff,0}$, and α_0, we developed an iterative solution procedure that solves equations (2.12)-(2.8) to resolve the interactions at the wafer/gas phase boundary. The overall solution algorithm begins by using the gas composition and measured wafer temperature to compute corresponding physical properties and to set the flow velocity and temperature field boundary conditions. The gas flow velocity field is computed using a Galerkin discretization technique [132] based on globally defined eigenfunctions; this solution approach determines the flow velocity component v_x and the pressure drop term β_{gt}.

By defining the gas temperature as a linear combination of gas temperature inside the gas domain (T_Ω) and at the chamber top and bottom boundaries ($T_{\partial\Omega,t}$, $T_{\partial\Omega,b}$),

$$\begin{aligned} T_g &= T_\Omega + T_{\partial\Omega,t} + T_{\partial\Omega,b} \\ &= \sum_{l,m,n=1}^{L,M,N} b_{lmn}\phi_l(x)\psi_m(y)\zeta_n(z) + \sum_{l,m=1}^{L,M} a_{lm}\phi_l(x)\psi_m(y)z \\ &\quad + \sum_{l,m=1}^{L,M} d_{lm}\phi_l(x)\psi_m(y)(1-z), \end{aligned} \tag{5.4}$$

we can formulate the residual of the gas temperature equation by substituting the corresponding trial function expansions into equation (2.13) to define the residual function

$$\mathcal{R} = \mathcal{L}T_\Omega + \mathcal{L}(T_{\partial\Omega,t} + T_{\partial\Omega,b}) - v_x\frac{\partial T_g}{\partial x}. \tag{5.5}$$

In equation (5.4) the b_{lmn}, a_{lm}, and d_{lm} are mode amplitude coefficients, and ϕ_l, ψ_m, and ζ_n are eigenfunctions in the three physical directions that satisfy $\mathcal{L}\phi\psi\zeta = \lambda\phi\psi\zeta$ and the homogeneous form of boundary conditions (2.14). The values of a_{lm} and d_{lm} are computed by projecting the gas temperature boundary conditions at $z = 0, 1$ onto (5.4). The residual function (5.5) is then projected onto the eigenfunctions using Galerkin's method. Because the eigenfunctions are defined by the eigenvalue problem $\mathcal{L}\phi\psi\zeta = \lambda\phi\psi\zeta$, we simplify the first term in (5.5) by replacing it with $\sum_{l,m,n=1}^{L,M,N} \lambda_{lmn} b_{lmn} \phi_l \psi_m \zeta_n$.

Because of the relative minor contribution of the convective term $v_x\ \partial T_g/\partial x$, the mode amplitude coefficients can be determined by the convergent, iterative algorithm:

$$b_{i,j,k} = \left\langle \mathcal{L}(T_{\partial\Omega,t} + T_{\partial\Omega,b}) - v_x \frac{\partial T_g}{\partial x}, \phi_i \psi_j \zeta_k \right\rangle / \lambda_{i,j,k}. \tag{5.6}$$

The weighted inner product is defined as

$$< f, g >= \int_0^1 \int_0^1 \int_0^1 f\ g\ \ dxdydz.$$

The representative gas temperature contours and wafer/gas energy transfer rate are displayed in Figure 5.1 for the simulation condition corresponding 100 *sccm* N_2.

Taking the wafer-average gas/wafer heat transfer rate (Figure 5.1(b)) as the Q_{top} in equation (2.8), we compute the wafer temperature using Newton's method to solve equation (5.1) for the TC No. 1-3 region and (5.2) for the TC No. 5 region. The updated wafer temperature is then fed back to the gas temperature computation as a new boundary condition at the chamber floor, and the entire computation is performed again. This iterative wafer temperature

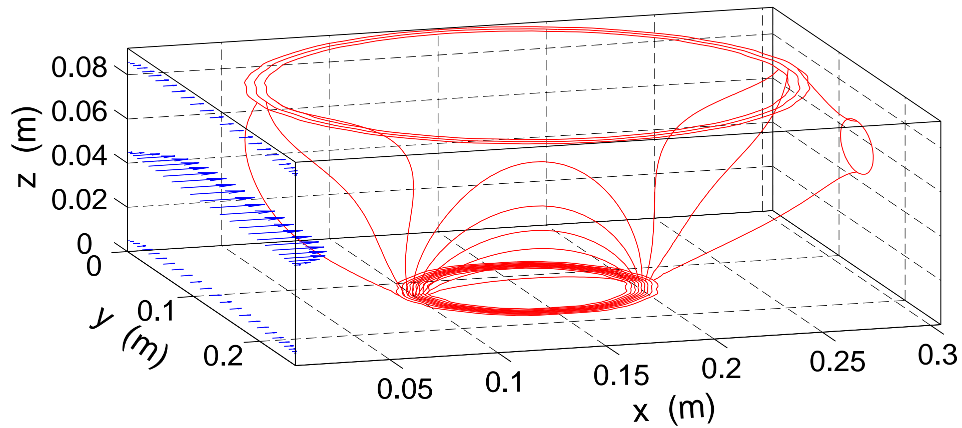

(a)

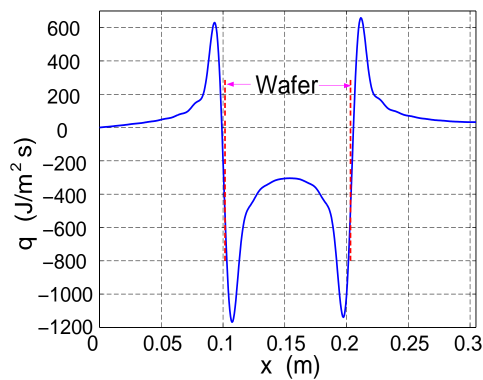

(b)

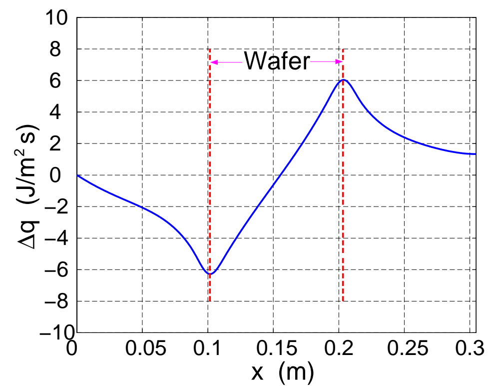

(c)

Figure 5.1: (a) Gas flow field and temperature contours where each contour represents 50 K temperature difference. (b) Wafer/gas heat transfer rate at centerline of the reactor chamber. Simulation performed at N_2 = 100 $sccm$ and 500 $mTorr$. (c) Difference of heat flux across wafer/gas boundary between N_2 = 100 and 60 $sccm$, where $\Delta q = q_{N_2=100} - q_{N_2=60}$.

computation scheme stops when a pre-specified temperature error tolerance is satisfied.

The parameter estimation procedure is based on minimizing the sum of the squared errors (SSE), where the error is defined by the difference between the experimentally measured and predicted wafer temperature at each gas composition. A MATLAB optimization toolbox function `minsearch.m` is used for this parameter identification method. The total identification procedure consists of the two optimization substeps:

1. Estimate the values of Q_{lp} and $\beta_{w,f}$ by minimizing the objective function defined by temperature data from TC No. 5.

2. Using the value of Q_{lp} estimated in first step, calculate the effective heat transfer coefficient parameters $h_{eff,0}$ and α_0 based on the minimizing the objective function defined by mean temperature measurement of TC No. 1-3.

The empirical showerhead temperature T_{sh} and floor temperature under the wafer T_f are assumed to be a constant 150 ^oC and 60 ^oC at steady-state, respectively. These values were obtained after a number of parameter identification runs and are consistent with observations made during the experiments. Figure 5.2 shows the steady-state temperature measurements taken from Figure 3.6; an extra wafer temperature point at 20% hydrogen was interpolated and used along with these measurements in the parameter estimation procedure. The estimated results are listed in Table 5.1.

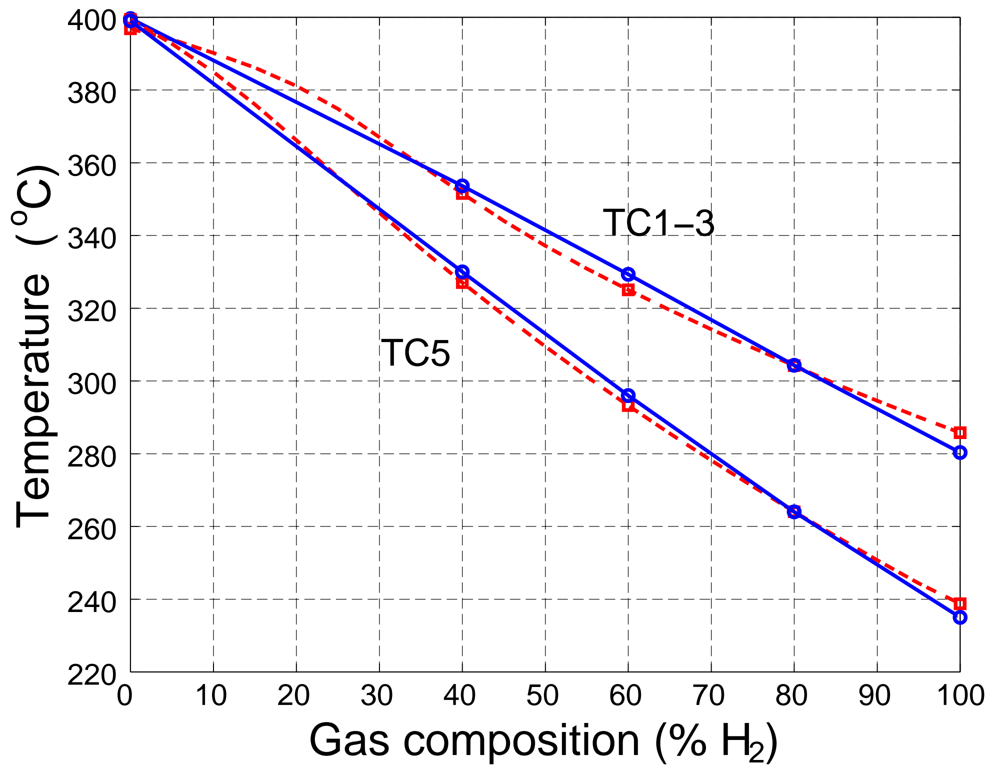

Figure 5.2: Wafer temperature from experimental data (solid curves with circles at data points) and model prediction (dot-dash curves and squares).

5.1.3 Model Validation and Discussion

We approach the problem of assessing the validity of our CVD simulator from two directions. The first test consists of a direct comparison of the model predictions over the entire gas composition range to the interpolated experimental data curves. Because the observed wafer temperatures demonstrate a nearly linear correlation with gas H_2 fraction, this test provides a good indication of whether the model structure and parameter values correctly reflect the balance between the highly nonlinear contributions of radiative heat transfer terms and the composition-dependent heat transfer mechanisms. Comparing the model predictions and experimental data reveals a mean model prediction error of less than 3 K for each data set (Figure 5.2). The heat transfer contributions from each terms in equation (2.8) are plotted in Figure 5.3. In both wafer regions, the radiative heat fluxes (Q_{lamp} and Q_{rad}) dominate in the high temperature range ($> 300\ ^oC$) and show nonlinear variations relative to the other heat transfer mechanisms because of the temperature dependency of wafer emissivity (absorptivity). The heat loss from Q_{bot}, which is more significant in the wafer area outside the susceptor (Figure 5.3(b)), increases in higher hydrogen fractions due to gas thermal conductivity increases and becomes equivalent to wafer irradiation around 300 ^oC (corresponding to 80% H_2 in Figure 5.3(a) and 60% H_2 in (b)). The thermal conduction through the wafer resulting from wafer temperature nonuniformity is negligible (Figure 5.3(b)), justifying our decision to ignore this term in the more temperature-uniform wafer interior region.

As the second test of model validity, we compare identified parameter values to values used in other studies, or compare our identified values to a range of values that can be theoretically justified. The guide and identified parameter

Table 5.1: A list of model parameter values, their estimated values or range, and the final values obtained from the identification procedure.

Variables	Guide values	Reference	Values identified
Q_{lp}	46740 W/m^2	Maximum value	30341.6 W/m^2
$\beta_{w,f}$	≈ 1	[42] (Theoretical value)	17.820
	30	[42] (Estimated value)	
$h_{eff,0}$	> 0		3.409 $W/(m^2K)$
α_0	$\alpha_0 < h_{eff,0}/(120K)$		-0.048 $W/(m^2K^2)$

values are compared in Table 5.1. The system dependent maximum incident lamp radiant flux Q_{lp}, as computed in previous section, is found to be about 1.5 times the value we estimated. The constant parameter $\beta_{w,f}$, on the other hand, is an order of magnitude larger than the theoretical value, but it is close to the value that was identified by Kleijn and Werner [42] using data obtained from their low pressure CVD reactor. Finally, the overall wafer/chamber floor heat transfer coefficient must be positive. Because $T_w - T_{w,N_2} < 0$, the requirement $h_{eff} > 0$ translates into an upper limit of α_0 as defined in Table 5.1; we note that the identified value satisfies this condition.

Solution Insensitivity to Flow Field

In Figure 5.1(c), we compare predicted gas/wafer heat transfer rates at 100 and 60 *sccm* nitrogen gas flows, corresponding to the experimental conditions used in Figure 3.7. While these simulations are computed based on the averaged

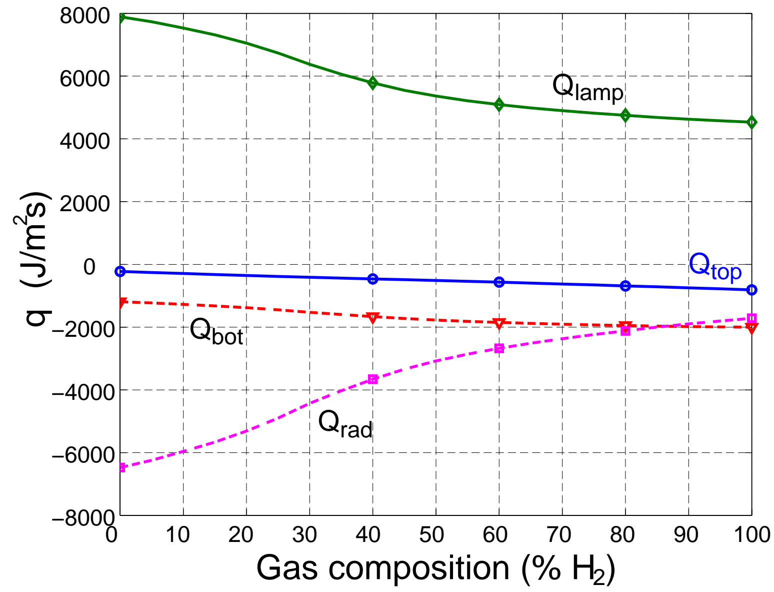

(a)

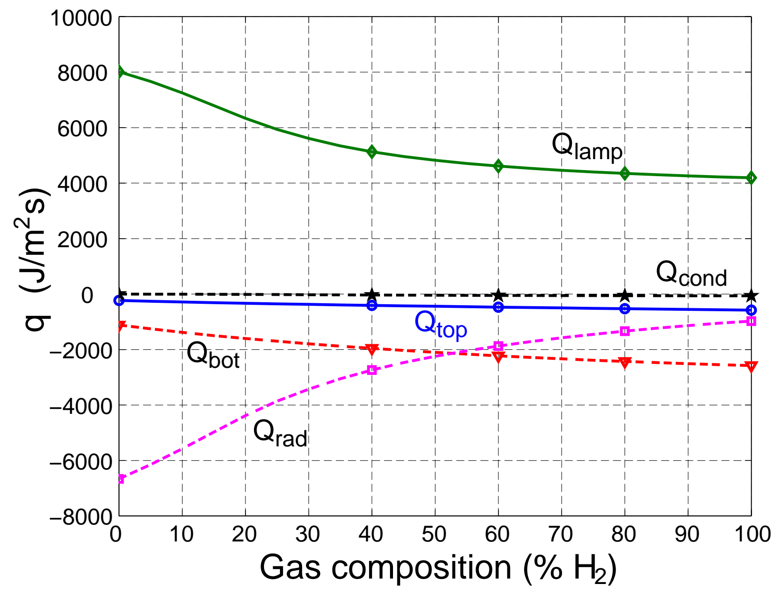

(b)

Figure 5.3: Contributions of individual heat transfer mechanisms for (a) interior region, and (b) region outside the susceptor.

thermocouple temperature measurements of TC No. 1-3, similar results are obtained when TC No. 5 measurements are used in the computation. The differences of the energy flux across the wafer/gas boundary of both gas flow cases are less than 7 $W/(m^2 K)$ and are small compared to the magnitude of the gas heat transfer rate itself. These simulation results corroborate with our experimental observations that the convective heat transfer effects are negligible when compared to gas conduction. The combination of the model predictions and experimental observations of the relative insensitivity of the wafer temperature to the gas velocity field justifies our omission of detailed fluid flow simulations of the combined side inlet and showerhead inlet streams.

Extrapolation of Model Predictions

The validated model predictions can be directly or indirectly extrapolated to actual processing condition. For example, because the convective heat transfer has only an insignificant effect on the wafer temperature, we can expect our wafer temperature predictions will not be affected by the 4 rpm wafer rotation used during process operation.

The use of the instrumented wafer limited experimental observations to tests only with non-reacting gas species. However, because wafer temperature was directly correlated to gas thermal conductivity in our modeling work, the results can be directly extrapolated to process gases containing WF_6 and H_2 and/or SiH_4 with adjustments made to wafer emissivity due to the deposited tungsten film. Our current blanket tungsten deposition processing recipe [31] consists of 10 $sccm$ WF_6 and 40 $sccm$ H_2 with a 15 to 20 minutes pre-conditioning period; our simulation predicts $T_w = 322\ ^oC$ at the start of deposition.

5.2 Wafer Thermal Dynamical Simulation

One of the motivations and main topics of this research is to improve the large wafer temperature difference between the system readings and the temperature measurements from the test TC wafer. Although alternative methods such as the experimentally developed processing window described in Section 3.4 can provide relatively constant steady-state wafer temperature during a limited time period for the tungsten deposition, a validated wafer temperature model that can predict the true wafer transient behavior is required to improve or redesign the temperature control system.

The wafer thermal dynamics model presented in this section is developed based on the heat transfer mechanisms studied for a steady-state model in Section 5.1 and the dynamic wafer temperature experimental data shown in Section 3.4.

5.2.1 Single Equation Wafer Temperature Model

Because the wafer energy balance model developed in Section 5.1 was based on steady-state data and ignored the transient term in Equation (2.7), the corresponding thermal mass M_w, originally defined as the product of wafer mass and the heat capacity, $(A_w \Delta_{z_w} \rho_w) C_{p_w}$, for the wafer temperature equation had to be determined from the dynamic experimental data for unmodeled fast transient effects.

We also noted (Section 3.2) that the true lamp power was not a linear function with respect to the lamp control signal recorded from the experiments during the fast transient conditions. Moreover, the lamp radiation actually emitted from

the lamp bank varied with lamp tungsten filament temperature. Therefore, an additional scaling factor $\alpha_{w,ref}$ was used in the lamp heating term to correct the lamp power level, giving the wafer temperature modeling equation

$$\begin{aligned} M_w \frac{\partial T_w}{\partial t} &= \alpha_{w,ref}\alpha_w(T_w)Q_{lp}u(t) + F_{\epsilon,top}F_{A,top}\sigma\left(T_{sh}^4 - T_w^4\right) \\ &\quad F_{\epsilon,bot}F_{A,bot}\sigma\left(T_f^4 - T_w^4\right) + h_g(T_w)(T_g - T_w) \\ &\quad + h_{w,f}(T_w)(T_w - T_f). \end{aligned} \tag{5.7}$$

A linear model of the form

$$\frac{d\,T_w}{d\,t} = A_{lin,w}\,T_w + B_{lin,w}\,u(t) \tag{5.8}$$

is used to find the guide values of M_w and $\alpha_{w,ref}$. It can be derived by using the Taylor series expansion of the nonlinear wafer energy balance equation (5.7) subject to the reference wafer temperature $T_{w,ref}$ and power signal u_{ref} and truncating after the first term. The linear model parameter $A_{lin,w}$ and $B_{lin,w}$ were given as

$$\begin{aligned} A_{lin,w}(T_{w,ref}) &= \left\{ -\left[\frac{\partial F_{\epsilon,top}F_{A,top}\sigma T_w^4}{\partial T_w}\right]_{T_{w,ref}} - \left[\frac{\partial F_{\epsilon,bot}F_{A,bot}\sigma T_w^4}{\partial T_w}\right]_{T_{w,ref}} \right. \\ &\quad \left. - \left[\frac{\partial h_{w,g}T_w}{\partial T_w}\right]_{T_{w,ref}} + \left[\frac{\partial h_f T_w}{\partial T_w}\right]_{T_{w,ref}} \right\} \frac{1}{M_w} \\ &= \left\{ -4F_{\epsilon,top}(T_{w,ref}, T_{sh,ref})F_{A,top}\sigma T_{w,ref}^3 \right. \\ &\quad -4F_{\epsilon,bot}(T_{w,ref}, T_f)F_{A,bot}\sigma T_{w,ref}^3 \\ &\quad \left. -h_{w,g}(T_{w,ref}) + h_f(T_{w,ref}) \right\} \frac{1}{M_w} \end{aligned}$$

$$\begin{aligned} B_{lin,w}(T_{w,ref}, u_{ref}) &= \frac{1}{M_w}\left[\frac{\partial \alpha_{w,ref}\;\alpha_w Q_{lp}\;u}{\partial u}\right]_{T_{w,ref},u_{ref}} \\ &= \frac{\alpha_{w,ref}\;\alpha_w(T_{w,ref})\;Q_{lp}}{M_w}. \end{aligned}$$

The solution to the linear equation is given by

$$T_w(t) = e^{A_{lin,w} t} \; T_w(0) + \int_0^t e^{A_{lin,w}(t-\xi)} \; B_{lin,w} \; u(\xi) \; d\xi \tag{5.9}$$

where $T_w(0)$ is the initial condition. In this single equation model, the model parameter $A_{lin,w}$ is the process eigenvalue that characterizes the system temperature dynamics and $B_{lin,w}$ represents the lamp controller gain.

The computations for the parameters $A_{lin,w}$ and $B_{lin,w}$ were performed in two steps. By using only the ramp down wafer temperature data in Figure 3.16 where the lamp was shut down, the process eigenvalue $A_{lin,w}$ can be estimated by solving the linear least-squares problem formed by multiple measurement points. The lamp power gain constant $B_{lin,w}$ was then approximated using the steady-state wafer temperature data

$$B_{lin,w} \approx A_{lin,w} \frac{T_{w,ss}}{u_{ss}}$$

because for constant u in Equation (5.8),

$$T_w(\infty) = -\frac{B_{lin,w}}{A_{lin,w}} \; u.$$

The thermal mass M_w was then estimated from $A_{lin,w}$ at the reference temperature and the scaling factor $\alpha_{w,ref}$ was obtained using $B_{lin,w}$ and M_w. The values of M_w and $\alpha_{w,ref}$ were used as guide values in the nonlinear model and several model prediction results for a multiple heating cycles process (from Figure 3.19) were compared in Figure 5.4.

There were three predicted temperature curves with the scaling factor, or the power gain, adjusted such that the model predictions fit the averaged experimental temperature trajectory during the ramp-up or ramp-down periods

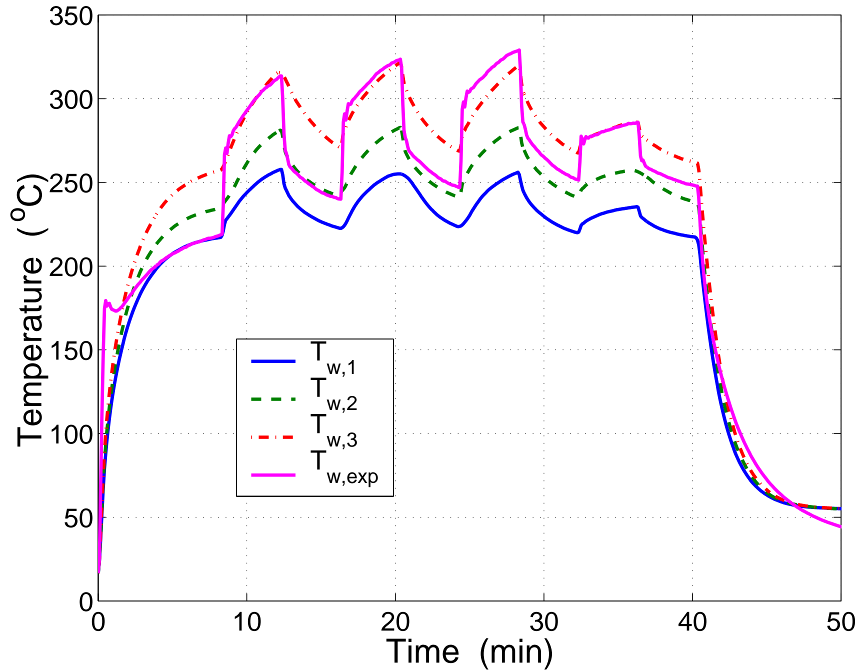

Figure 5.4: Comparison of the wafer temperature between the experimental measurements $T_{w,exp}$ (from Figure 3.19) and the single equation nonlinear wafer temperature model predictions $T_{w,1}, T_{w,2}$ and $T_{w,3}$ for a multiple heating cycles process.

around the first and second setpoints change in Figure 5.4. Although the models predicted the temperature response relatively accurately in the ramp-down phase, the wafer temperatures in these three cases failed to capture the true thermal dynamics when lamp heating was used in the process.

There were two other physical phenomena observed in the experimental data that cannot be predicted by the single equation wafer temperature model. The fast transient response, shown as the initial temperature "bump", was ignored by the wafer model. This was understandable because, as discussed in Section 3.4

for Figure 3.17, the initial "bump" behavior mainly resulted from the thermocouple heating that reflected the immediate lamp power variations. These fast thermocouple responses to the lamp radiation could also been observed experimentally in the subsequent setpoint changes, such as those shown in Figure 5.5 from the experimental data provided in Figure 3.19.

The second phenomena that the single wafer model failed to predict was the long term temperature increase from the slow reactor chamber heating, especially the temperature increase of the transparent quartz showerhead, as discussed in Section 3.4. Therefore, a new model that included the thermocouple and showerhead energy balance equations was developed as the new temperature simulator.

5.2.2 The Three Equation Temperature Simulator

In the new temperature simulator, the measurements from the instrumented wafer were compared to the thermocouple temperature predictions. The thermocouple and showerhead equations (2.10), (2.11) were rearranged to the following forms

$$\begin{aligned} M_{sh}\frac{\partial T_{sh}}{\partial t} &= \alpha_{sh,ref}\alpha_{sh}(T_{sh})Q_{lp}u(t) + F_{\epsilon,sh-w}F_{A,sh-w}\sigma\left(T_w^4 - T_{sh}^4\right) \\ & \quad F_{\epsilon,sh-f}F_{A,sh-f}\sigma\left(T_f^4 - T_{sh}^4\right) + h_{sh}(T_{sh})(T_g - T_{sh}) \end{aligned} \tag{5.10}$$

$$\frac{\partial T_{TC}}{\partial t} = \frac{\alpha_{TC0} + \alpha_{TC1}(u(t) - u_{ss})}{M_{TC}}Q_{lp}u(t) + \frac{h_{TC}}{M_{TC}}(T_w - T_{TC}) \tag{5.11}$$

where u_{ss} was the reference power level and was set to the steady state value of 0.56 used in the gas composition experiments from Section 5.1.

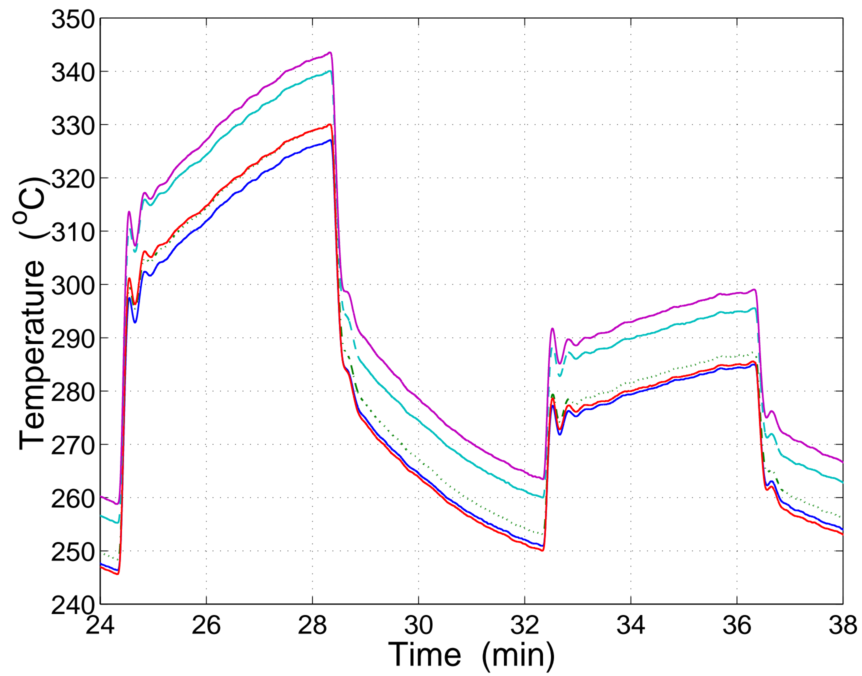

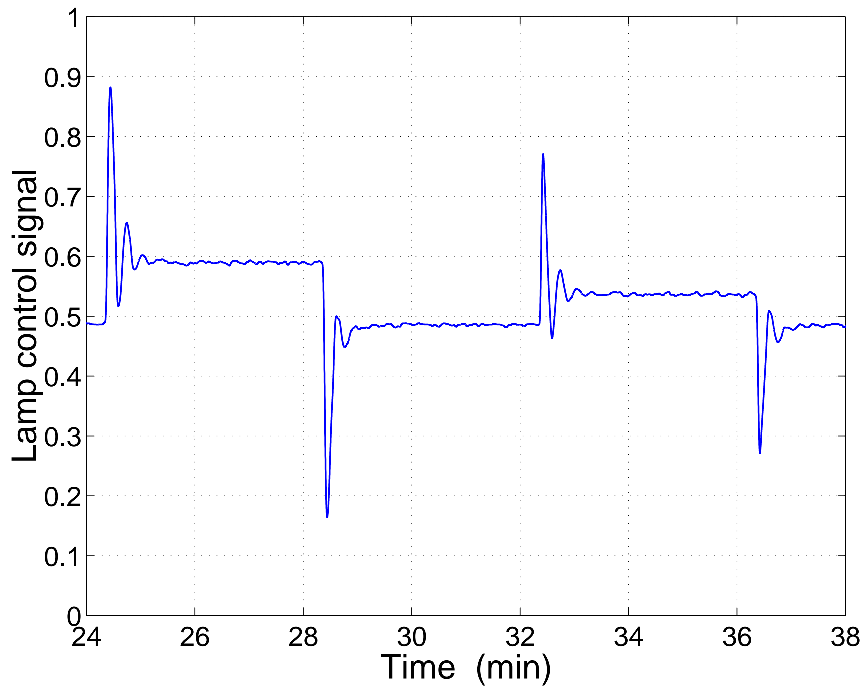

Figure 5.5: The wafer temperature (thermocouples) fast response to the lamp power variations during setpoint changes. Data are taken from Figure 3.19.

Several model parameters from all three equations had to be estimated using the experimental data. We chose to identify the power scaling factors for wafer $\alpha_{w,ref}$ and showerhead $\alpha_{sh,ref}$, the showerhead conductive/convective heat transfer coefficient h_{sh}, and the three thermocouple absorptivity and conductive heat transfer parameters divided by the thermocouple thermal mass, α_{TC0}/M_{TC}, α_{TC1}/M_{TC}, and h_{TC}/M_{TC}.

The identification of the wafer power scaling factor was needed because the nonlinear behavior of the true lamp radiant power and the control signal as well as the constant showerhead temperature used in the steady-state model, while the showerhead power scaling factor was mainly used to model the true nonlinear lamp power output. Although the showerhead heat transfer coefficient could be computed from the gas temperature gradients near the gas/showerhead interface in a similar procedure used to compute the heat transfer coefficients for wafer, we chose to estimate its value because the hydrogen gas used in our dynamic experiments passed through the showerhead and added an additional cooling effect.

The wafer thermal mass M_w used the value identified from the linearized model while the empirical showerhead thermal mass M_{sh} was estimated from the numerical experimental studies.

The parameter estimation problem was formulated as in equation (4.1) with parameter vector $\mathbf{p}$ containing six elements described in above paragraphs. The averaged temperature measurements in Figure 3.19 was used for the identification procedure and interpolated at total 60 nonequally distributed time points. Thermocouple temperature predictions were used to compare with the experimental data in the nonlinear least-squares problem.

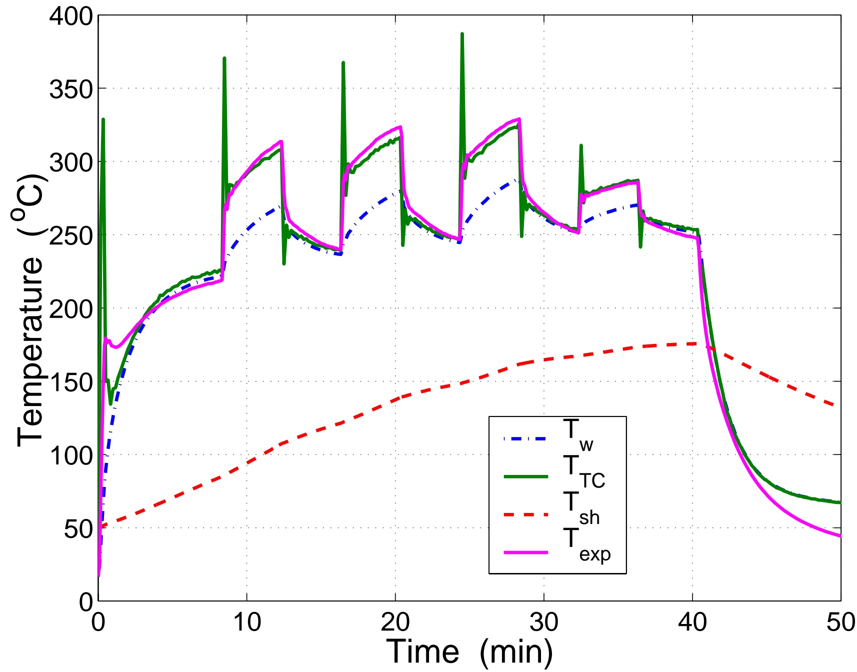

Figure 5.6: The wafer temperature prediction from the identified model. Results are compared with experimental data shown in Figure 3.19.

The identified parameter values and the wafer and showerhead empirical thermal masses were listed in Table 5.2 and the model prediction was plotted along with experimental data in Figure 5.6. The initial condition used in the simulation for the thermocouple temperature was the same with the initial wafer temperature and 50 ^{o}C was used for the showerhead temperature from experimental experience. The predicted wafer temperature (dash-dotted curve in Figure 5.6) had good agreement with the experimental data during the ramp-down period in each heating cycle but had large temperature differences in the ramp-up phase. The long-term wafer temperature heating phenomena was successfully captured by the addition of the slowly increased showerhead temperature.

On the other hand, the thermocouple temperature successfully predicted the

Table 5.2: A list of identified model parameter values.

Parameters	Values identified
$\alpha_{w,ref}$	1.13
$\alpha_{sh,ref}$	0.05
h_{sh}	3.56 $W/(m^2K)$
α_{TC0}/M_{TC}	0.0018
α_{TC1}/M_{TC}	0.0224
h_{TC}/M_{TC}	1.20
M_w	2500 $J/(m^2K)$
M_{sh}	13332 $J/(m^2K)$

TC wafer measurement data over the entire process. Large temperature oscillations were generated at the beginning of each setpoint change due to the lamp power amplification, where large values of the lamp control signals were amplified more by the lamp power signal squares $(u(t)^2)$ of the lamp radiation absorption term when compared to its small steady-state values. However, it should be noted that good agreements achieved between the data and predictions in the remaining process were more important for the simulator applications.

5.2.3 Model Validation and Simulation Results

The three equation temperature model was validated by comparing the model predictions with the instrumented wafer measurements in another process with

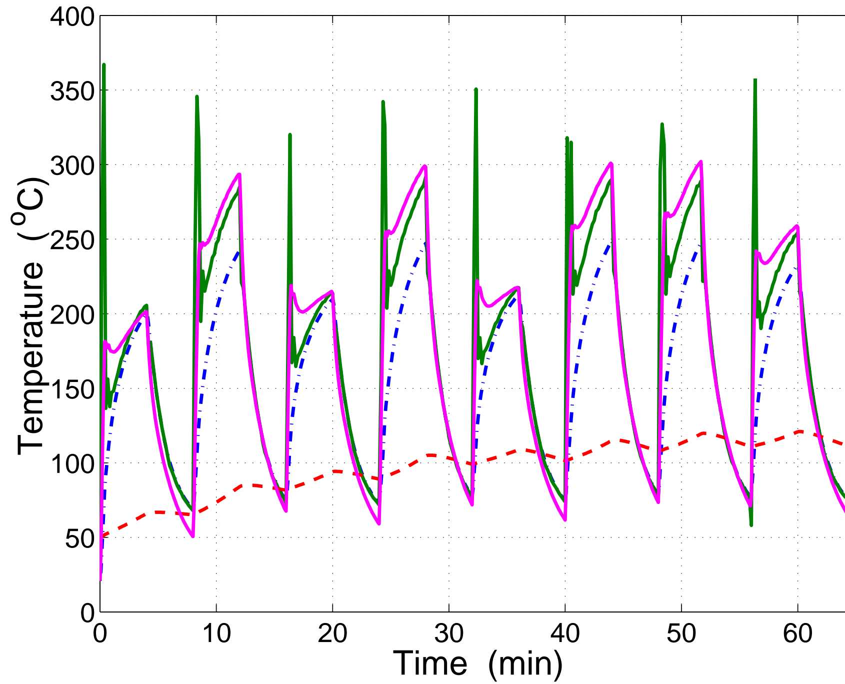

Figure 5.7: The wafer temperature prediction from the identified model. Results are compared with experimental data shown in Figure 3.20.

multiple heating cycles (see Figure 3.20). Although the high temperature setpoints were the same with those used in the identification experiment that switched between 450, 500, and 550 ^oC, they were reset to zero instead of 450 ^oC for the ramp-down periods and thus reduced the overall heating to the showerhead. This difference of energy transfer to the showerhead between these two experiments provided a good test for the showerhead temperature model and the difference was showed both in the slower temperature increase in Figure 5.7 compared to Figure 5.6 and the waving behavior between ramp-up and down phases of the showerhead temperature. Except the consistent underpredictions of the thermocouple responses to all 550 ^oC setpoints, the slow increase of the showerhead temperature proved to successfully capture the long term heating dynamics

of this process and explained the small increases of the peak temperature values in the experimental data over the entire process.

Because the temperature was relatively low at the beginning of each small heating cycle, the large temperature "bumps" can only qualitatively predicted by the current model. Peak temperatures for the 450 ^{o}C setpoints were predicted accurately, and the differences of peak temperature for the 500 and 550 ^{o}C setpoints were about 4 and 10 ^{o}C, respectively. Those differences mainly resulted from the current form of the thermocouple absorptivity and the selection of the steady-state lamp control signal value, and could be improved should more accurate absorptivity model developed.

Process Simulation

The simulation results for the three single heating cycle processes with temperature setpoints at 450, 500, and 550 ^{o}C were shown in Figures 5.8, 5.9, and 5.10, respectively. The model predictions of the thermocouple temperature had good agreements with the temperature data in the 450 ^{o}C case but showed differences in other two processes, as those differences found in the predictions of the validation experiment.

When compare the difference between the thermocouple and wafer temperature predictions, the predicted wafer temperature was almost the same with the thermocouple temperature in the 450 ^{o}C process. However, there were 10 to 25 ^{o}C differences when the processes approaching the end of ramp-up periods in the other two cases and also differed from the measurement data. These offsets can be explained by the structure of the thermocouple modeling equation (5.11) that when the process approached the steady-state, there were always some dif-

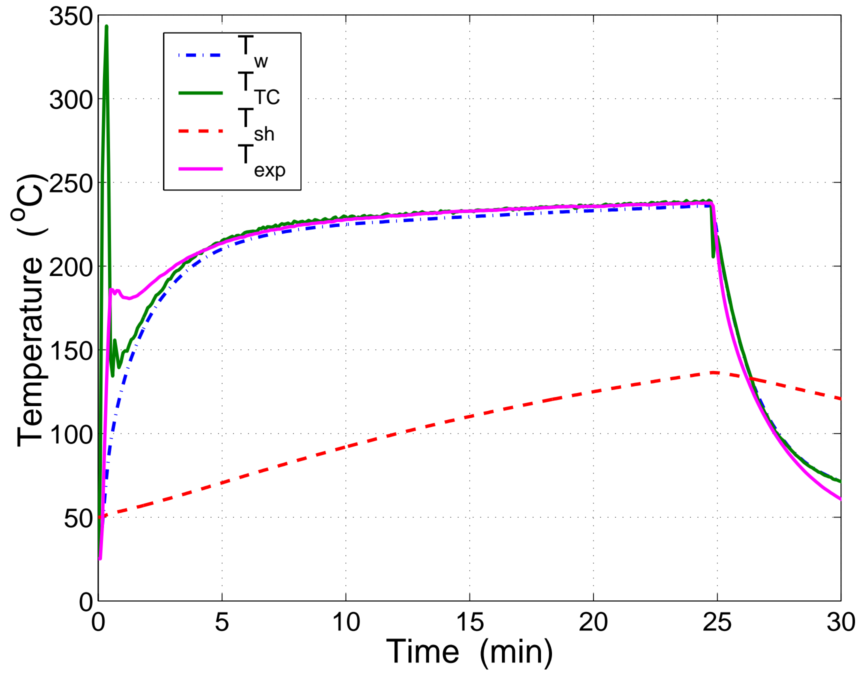

Figure 5.8: The wafer temperature prediction from the identified model. Results are compared with experimental data shown in Figure 3.14.

ferences between the wafer and thermocouple temperatures if the lamp power signal was different from the reference value u_{ss} at the steady-state.

The simulation of the process window which discussed in Section 3.4 was presented in Figure 5.11. The steady-state deposition period was predicted with about 4 to 7 ^{o}C difference with the experimental data during the constant temperature deposition period.

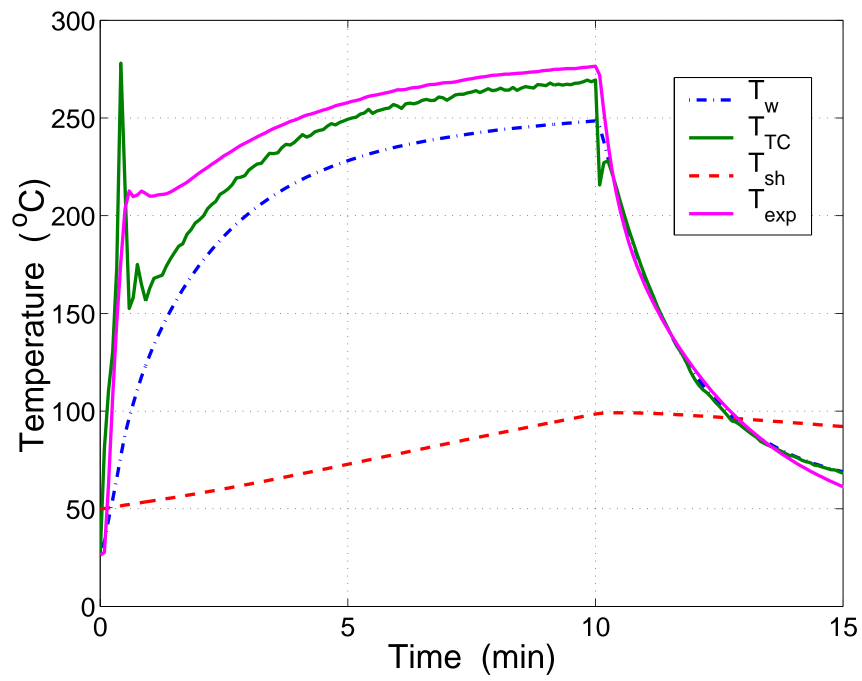

Figure 5.9: The wafer temperature prediction from the identified model. Results are compared with experimental data shown in Figure 3.15.

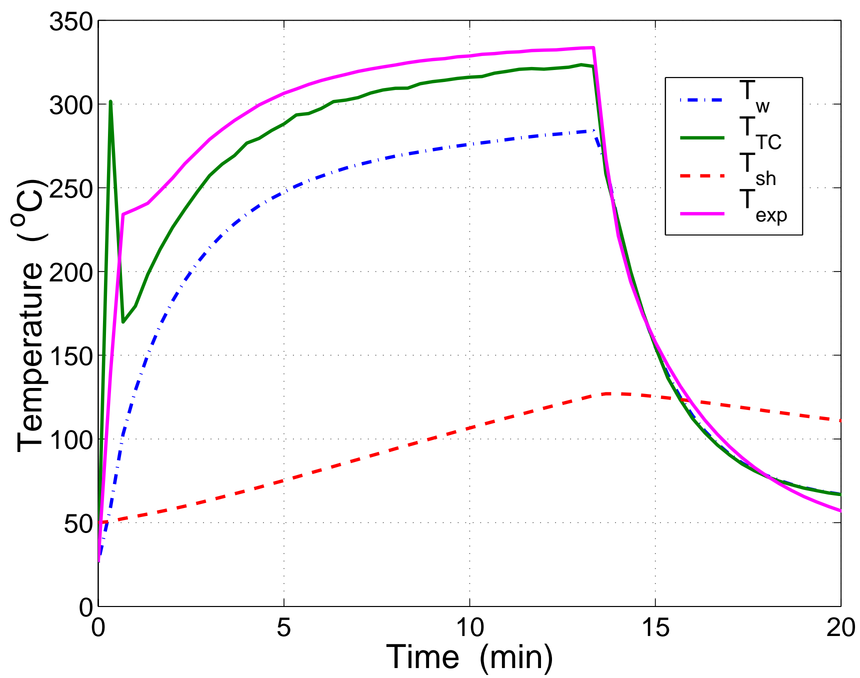

Figure 5.10: The wafer temperature prediction from the identified model. Results are compared with experimental data shown in Figure 3.16.

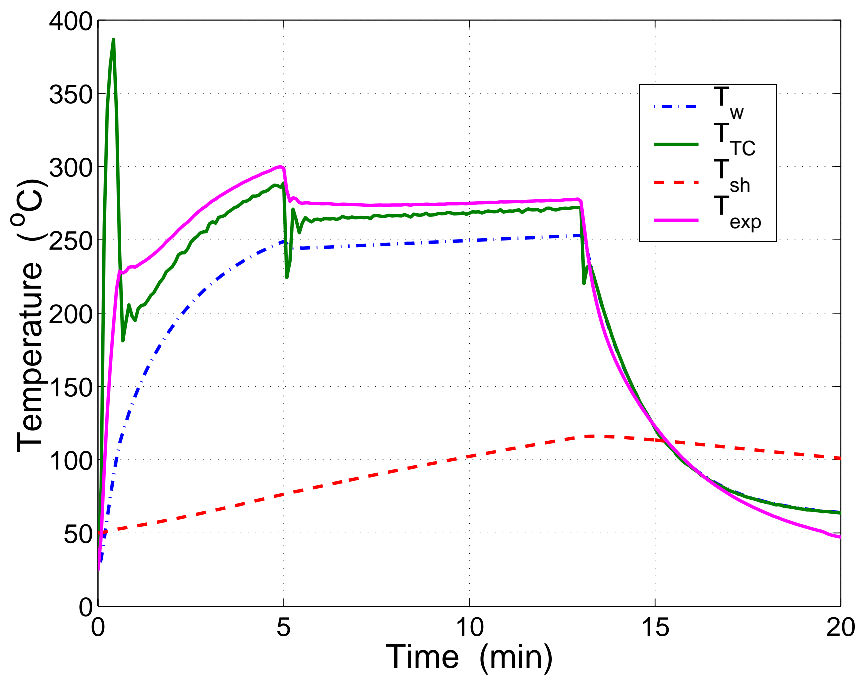

Figure 5.11: The wafer temperature prediction from the identified model for processing window shown in Figure 3.13.

Chapter 6

Conclusions and Future Work

6.1 Concluding Remarks

In this thesis, the fundamentals of chemical vapor deposition equipment modeling were reviewed and a mathematical model for the ULVAC ERA-1000 tungsten chemical vapor deposition reactor was developed. A data acquisition system was built for the tungsten CVD system and several sets of experiments were conducted to investigate the effects of process parameters such as gas composition and chamber pressure on the wafer temperature. A large temperature difference was found during the process between the system reported wafer temperature and measurements from a thermocouple instrumented wafer placed inside the reactor. Recipes providing constant wafer temperature for tungsten deposition in finite time periods were experimentally developed.

A three dimensional steady-state gas flow and temperature model was developed and used to compute the energy transferred across the gas/wafer interface. Several weighted residual methods based on globally defined basis functions were

used for the discretizations of the PDE modeling equations. Parameter estimation techniques were implemented to identify the system dependent wafer heat transfer parameters from the experimental data in an iterative computational scheme that considering the interactive energy exchanges between the wafer and gas temperature fields. Good agreement was found between the model predictions and experimental measurements at various gas compositions while estimated parameter values were comparable to those published in the literature. Wafer temperature was found to be a strong function of the gas compositions indicating the model predictions could be extended to the processes with reactive gases. Both experimental and simulation studies showed the gas flow field had little effect on wafer temperature at the low chamber pressure.

A dynamic temperature simulator was built based on the steady-state wafer temperature model that uses only the experimentally recorded lamp control signals to predict the temperature trajectories. Empirical wafer thermal mass and lamp controller gain were estimated using a linearized wafer temperature model from a single heating cycle experiment. A three-equations model was developed to represent the fast transient temperature dynamics and long-term showerhead/chamber heating phenomena. Several heat transfer parameters of the model were identified using the Gauss-Newton method and the simulator successfully predicted the temperature trajectories for several single or multiple heating cycles experiments.

6.2 Suggested Future Work

The dynamic wafer temperature model presented in this thesis provides valuable information on the heat transfer mechanisms and can be used to improve the temperature control system. Several research topics that can be built on this work are suggested as follows:

Thermocouple Model Refinement

The current thermocouple modeling equation only considers heat conduction from surrounding wafer regions to the thermocouples and the lamp radiation absorption. The absorptivity used in the model is a linearized function of the lamp power control signal and the deviations between the wafer and thermocouple temperature predictions will arise when process has different steady-state power level from the reference value used in the linearization. Improvements to reduce temperature offset and the temperature oscillations at the beginning of setpoint changes could be made by developing better absorptivity model and/or the addition of thermocouple emission heat transfer term.

Model Extension to True Process Conditions

The models developed and validated in this research are based on the experimental data obtained in processes using non-reacting gases due to the limitation of the instrumented wafer. Although research results indicate the model predictions can be extended to the true process conditions, effects of the wafer emissivity and absorptivity changes due to the deposited tungsten films has yet to be analyzed. To extend model for processes with reactive gases, experiments should

be conducted to quantify the temperature differences resulted from emissivity changes.

Model Reduction Studies

Model reduction is a means to arrive at simplified descriptions of the behavior of a complex system that is computationally inefficient for real-time simulation applications. Optimal trial functions can be obtained by applying the statistical based methods to either simulation results or experimental data. The three dimensional gas temperature filed computation can be simplified and accelerated if the optimal trial functions are obtained and used.

Wafer Temperature Control Improvement

The developed dynamic temperature simulator can be integrated with the data acquisition system using LabVIEW interface, the predicted wafer temperature thus can be used to replace the ULVAC adjusted wafer temperature as the feedback signal for the system temperature controller. After fine tuning the PID controller parameters, the new system could provide better control of the wafer temperature. However, the implementation issues such as inaccurate temperature information given by the simulator due to process drifts should be carefully studied.

Bibliography

[1] Y. K. Chae, Y. Egashira, Y. Shimogaki, K. Sugawara, and H. Komiyama. Chemical vapor deposition reactor design using small-scale diagnostic experiments combined with computational fluid dynamics simulations. *Journal of Electrochemical Society*, 146(5):1780–1788, 1999.

[2] A. Hasper, J. Holleman, J. Middlehoek, C. R. Kleijn, and C. J. Hoogendoorn. Modeling and optimization of the step coverage of tungsten LPCVD in trenches and contact holes. *J. Electrochem. Soc.*, 138(6):1728–1738, 1991.

[3] B. Peuse, G. Miner, M. Yam, and C. Elia. Advances in RTP temperature measurement and control. In M. C. Ozturk, F. Roozeboom, P. T. Timans, and S. H. Pas, editors, *Rapid Thermal and Integrated Processing VII*, volume 525 of *Mat. Res. Soc. Symp. Proc.*, pages 71–85, Warrendale, PA, 1998. Materials Research Society.

[4] P. Vandenabeele and W. Renken. Model based temperature control in RTP yielding $\pm 0.1^oC$ accuracy on a 1000^oC, 2 second, 100 $^oC/s$ spike anneal. In M. C. Ozturk, F. Roozeboom, P. T. Timans, and S. H. Pas, editors, *Rapid Thermal and Integrated Processing VII*, volume 525 of *Mat.*

Res. Soc. Symp. Proc., pages 109–114, Warrendale, PA, 1998. Materials Research Society.

[5] K. Tsakalis and K. Stoddard. Integrated identification and control for diffusion/CVD furnaces. In *6th IEEE Int. Conference on Emerging Technologies and Factory Automation*, pages 514–519, 1997.

[6] T. S. Cale, P. E. Crouch, L. Song, and K. S. Tsakalis. Increasing throughput in low pressure chemical vapor deposition: An optimal control approach. In *Proceedings of American Control Conference*, pages 1289–1293, Seattle, WA, June 1995.

[7] C. D. Schaper, M. M. Moslehi, K. C. Sarawat, and T. Kailath. Modeling, identification, and control of rapid thermal processing system. *J. Electrochem. Soc.*, 141(11):3200–3209, 1994.

[8] J. D. Stuber, I. Trachtenberg, T. F. Edgar, J.K. Elliott, and T. Breedijk. Model-based control of rapid thermal processes. In *Proceedings of the 33rd Conference on Decision and Control*, pages 79–85, Lake Buena Vista, FL, December 1994.

[9] C. R. Kleijn. Chemical vapor deposition processes. In M. Meyyappan, editor, *Computational Modeling in Semiconductor Processing*, chapter 4. Artech House, Boston, 1995.

[10] K. F. Jensen, T. P. Merchant, J. V. Cole, J. P. Hebb, K. L. Knutson, and T. G. Mihopoulos. Modeling strategies for rapid thermal processing: Finite element and Monte Carlo methods. In F. Roozeboom, editor, *Advances*

in Rapid Thermal and Integrated Processing, chapter 10, pages 265–304. Kluwer Academic Publisher, Netherlands, 1996.

[11] T. A. Badgwell, T. Breedijk, S. G. Bushman, S. W. Butler, S. Chatterjee, T. F. Edgar, A. T. Toprac, and I. Trachtenberg. Modeling and control of microelectronics materials processing. *Comput. Chem. Engng.*, 19(1):1–41, 1995.

[12] H. Rouch, M. Pons, A. Benezech, C. Bernard, and R. Madar. Thermodynamic equilibrium and mass transport coupled modeling of the chemical vapour deposition process. *Thin Solid Films*, 281-282:64–67, 1996.

[13] T. J. Burns, R. W.Davis, and E. F. Moore. Dynamical systems approach to particle transport modeling in dilute gas-particle flows with application to a chemical vapor deposition reactor. *Aerosol Science and Technology*, 27:1–21, 1997.

[14] T. S. Cale and G. B. Raupp. A unified line-of-sight model of deposition in rectangular trenches. *J. Vac. Sci. Technol. B*, 8(6):1242–1248, 1990.

[15] T. S. Cale, T. H. Grandy, and G. B. Raupp. A fundamental feature scale model for low pressure deposition processes. *J. Vac. Sci. Technol. A*, 9(3):524–529, 1991.

[16] H. K. Moffat and K. F. Jensen. Three-dimensional flow effects in silicon CVD in horizontal reactors. *J. Electrochem. Soc.*, 135(2):459–471, 1988.

[17] C. R. Klijn, C. J. Hoogendoorn, A. Hasper, J Holleman, and J. Middelhoek. Transport phenomena in tungsten LPCVD in a single-wafer reactor. *J. Electrochem. Soc.*, 138(2):509–517, 1991.

[18] P. Duverneuil and J. P. Couderc. Two-dimensional modeling of low-pressure chemical vapor deposition hot wall tubular reactor. *J. Electrochem. Soc.*, 139(1):296–304, 1992.

[19] C. Y. Chang and S. M. Sze, editors. *ULSI Technology.* McGraw-Hill, New York, 1996.

[20] A. Sherman. *Chemical Vapor Deposition for Microelectronics Principles, Technology, and Applications.* Noyes Publications, New Jersey, 1987.

[21] S. Sivaram. *Chemical Vapor Deposition : Thermal and Plasma Deposition of Electronic Materials.* Von Nostrand Reinhold, New York, 1995.

[22] M. M. Moslehi, L. Velo, A. Paranjpe, J. Kuehne, S. Huang, R. Chapman ahd C. Schaper, T. Breedijk, H. Najm, D. Yin, Y. J. Lee, D. Anderson, and C. Davis. Fast-cycle-time single-wafer IC manufacturing. *Microelectronic Engineering*, 25:93–130, 1994.

[23] J. P. Hebb and K. F. Jensen. The effect of patterns on thermal stress during rapid thermal processing of silicon wafers. *IEEE Transactions on Semiconductor Manufacturing*, 11(1):99–107, 1998.

[24] D. Peyton, H. Kinoshita, G. Q. Lo, and D. L. Kwong. System-oriented survey of non-contact temperature measurement techniques for rapid thermal processing. In R. Singh and M. M. Moslehi, editors, *Rapid Thermal and Related Processing Techniques*, volume 1393 of *SPIE Proceedings*, pages 295–308. SPIE, 1990.

[25] R. B. Fair. Rapid thermal processing - a justification. In *Rapid Thermal Processing: Science and Technology*, chapter 1, pages 1–11. Academic Press, Boston, MA, 1993.

[26] F. Roozeboom. Rapid thermal processing: Status, problems and options after the first 25 years. In *Rapid Thermal and Integrated Processing II*, volume 303 of *Mat. Res. Soc. Symp. Proc.*, pages 149–164. Materials Research Society, Pittsburgh, PA, 1993.

[27] K. C. Saraswat. Rapid thermal multiprocessing for a programmable factory for manufacturing of ICs. In F. Roozeboom, editor, *Advances in Rapid Thermal and Integrated Processing*, chapter 13, pages 375–413. Kluwer Academic Publishers, 1996.

[28] R. P. S. Thakur, P. J. Timans, and S. P. Tay. RTP technology for tomorrow. *Solid State Technology*, 38(6):171–183, 1998.

[29] T. Ohba. Chemical-vapor-deposited tungsten for vertical wiring. *MRS Bulletin*, pages 46–52, November 1995.

[30] P. J. Ireland. High aspect ratio contacts: A review of the current tungsten plug process. *Thin Solid Films*, 304:1–12, 1997.

[31] T. Gougousi, Y. Xu, Jr. J. N. Kidder, G. W. Rubloff, and C. R. Tilford. Process diagnostics and thickness metrology for the chemical vapor deposition of W from H_2/WF_6 using in-situ mass spectrometry. *J. Vac. Sci. Technol. B*, 18(3):1352–1363, 2000.

[32] J. A. M. Ammerlaan. *Kinetics and Characterization of Tungsten CVD Processes*. Delft University Press, Netherlands, 1994.

[33] E. K. Broadbent and C. L. Ramiller. Selective low pressure chemical vapor deposition of tungsten. *J. Electrochem. Soc.*, 131(6):1427–1433, 1984.

[34] C. M. McConica and K. Krishnamani. The kinetics of LPCVD tungsten deposition in a single wafer reactor. *J. Electrochem. Soc.*, 133(12):2542–2548, 1986.

[35] J. J. Hsieh. Kinetic model for the chemical vapor deposition of tungsten in the silane reduction process. *J. Vac. Sci. Technol. A*, 11(6):3040–3046, 1993.

[36] R. S. Rosler, J. Mendonca, and Jr. M. J. Rice. Tungsten chemical vapor deposition characteristics using SiH_4 in a single wafer system. *J. Vac. Sci. Technol. B*, 6(6):1721–1727, 1988.

[37] R. V. Joshi, V. Prasad, L. Krusin-Elbaum, M. Yu, and M. Norcott. Mechanisms controlling temperature dependent mechanical and electrical behavior of SiH_4 reduced chemically vapor deposited W. *Journal of Applied Physics*, 68(11):5625–5629, 1990.

[38] R. B. Bird, W. E. Stewart, and E. N. Lightfoot. *Transport Phenomena.* John Wiley & Sons, Inc., Singapore, 1965.

[39] M. E. Coltrin, R. J. Kee, and J. A. Miller. A mathematical model of the coupled fluid mechanics and chemical kinetics in a chemical vapor deposition reactor. *J. Electrochem. Soc.*, 131(2):425–434, 1984.

[40] H. K. Moffat and K. F. Jensen. Complex flow phenomena in MOCVD reactors: I. horizontal reactors. *J. Crystal Growth*, 77:108–119, 1986.

[41] S. Middleman and A. Hochberg. *Process Engineering Analysis in Semiconductor Device Fabrication*, chapter 12, pages 478–573. McGraw-Hill, New York, 1993.

[42] C. R. Kleijn and C. Werner. *Modeling of Chemical Vapor Deposition of Tungsten Films*. Birkhauser Verlag, Boston, MA, 1993.

[43] D. I. Fotiadis, M. Boekholt, K. F. Jensen, and W. Richter. Flow and heat transfer in CVD reactors: Comparison of Raman temperature measurements and finite element model predictions. *J. Crystal Growth*, 100:577–599, 1990.

[44] D. I. Fotiadis, S. Kieda, and K. F. Jensen. Transport phenomena in vertical reactors for metalorganic vapor phase epitaxy. I. effects of heat transfer characteristics, reactor geometry, and operating conditions. *J. Crystal Growth*, 102:441–470, 1990.

[45] K. F. Jensen. Transport phenomena and chemical reaction issues in OMVPE of compound semiconductors. *J. Crystal Growth*, 98:148–166, 1989.

[46] N. K. Ingle and T. J. Mountziaris. The onset of transverse recirculations during flow of gases in horizontal ducts with differentially heated lower walls. *J. Fluid Mech.*, 277:249–269, 1994.

[47] K.-C. Chiu and F. Rosenberger. Mixed convection between horizontal plates - I. entrance effects. *Int. J. Heat Mass Transfer*, 30(8):1645–1654, 1987.

[48] K.-C. Chiu, J. Ouazzani, and F. Rosenberger. Mixed convection between horizontal plates - II. fully developed flow. *Int. J. Heat Mass Transfer*, 30(8):1655–1662, 1987.

[49] T. J. Mountziaris, S. Kalyanasundaram, and N. K. Ingle. A reaction-transport model of GaAs growth by metalorganic chemical vapor deposition using trimethyl-gallium and tertiary-butyl-arsine. *J. Crystal Growth*, 131:283–299, 1993.

[50] W. L. Holstein and J. L. Fitzjohn. Effect of buoyancy forces and reactor orientation of fluid flow and growth rate uniformity in cold-wall channel CVD reactors. *J. Crystal Growth*, 94:145–158, 1989.

[51] G. Evans and R. Greif. A study of traveling wave instabilities in a horizontal channel flow with applications to chemical vapor deposition. *Int. J. Heat and Mass Transfer*, 32(5):895–911, 1989.

[52] G. Evans and R. Greif. A numerical model of the flow and heat transfer in a rotating disk chemical vapor deposition reactor. *Journal of Heat Transfer*, 109:928–935, 1987.

[53] H. Habuka, M. Katayama, M. Shimada, and K. Okuyama. Numerical evaluation of silicon-thin film growth from $SiHCl_3$-H_2 gas mixture in a horizontal chemical vapor deposition reactor. *Jpn. J. Appl. Phys.*, 33(4A):1977–1985, 1994.

[54] H. Habuka, T. Nagoya, and M. Katayama. Modeling of epitaxial silicon thin-film growth on a rotating substrate in a horizontal single-wafer reactor. *J. Electrochem. Soc.*, 142(12):4272–4278, 1995.

[55] K. F. Jensen and D. B. Graves. Modeling and analysis of low pressure CVD reactors. *J. Electrochem. Soc.*, 130:1950, 1983.

[56] T. A. Badgwell, T. F. Edgar, I. Trachtenberg, G. Yetter, J. K. Elliott, and R. L. Anderson. In situ measurement of wafer temperature in a low pressure chemical vapor deposition furnace. *IEEE Transactions on Semiconductor Manufacturing*, 6(1):65–71, 1993.

[57] T. A. Badgwell, T. F. Edgar, and I. Trachtenberg. Modeling the wafer temperature profile in a multiwafer LPCVD furnace. *J. Electrochem. Soc.*, 141:161, 1994.

[58] K. J. Kuijlaars, C. R. Kleijn, and H. E. A. van den Akker. Multi-component diffusion phenomena in multi-wafer chemical vapour deposition reactors. *The Chemical Engineering Journal*, 57:127–136, 1995.

[59] J. Holleman, A. Hasper, and C. R. Kleijn. Loading effects on kinetical and electrical aspects of silane-reduced low-pressure chemical vapor deposited selective tungsten. *J. Electrochem. Soc.*, 140(3):818–825, 1993.

[60] K. J. Kuijlaars, C. R. Kleijn, and H. E. A. van den Akker. A detailed model for low-pressure CVD of tungsten. *Thin Solid Films*, 270:456–461, 1995.

[61] K. J. Kuijlaars, C. R. Kleijn, and H. E. A. van den Akker. Modeling of selective tungsten low-pressure chemical vapor deposition. *Thin Solid Films*, 290-291:406–410, 1996.

[62] K. J. Kuijlaars, C. R. Kleijn, and H. E. A. van den Akker. Simulation of selective tungsten chemical vapour deposition. *Materials Science in Semiconductor Processing*, 1:43–54, 1998.

[63] A. Kersch, H. Schafer, and C. Werner. Improvement of thermal uniformity of PTR-CVD equipment by application of simulation. In *IEDM 91*, pages 883–886, 1991.

[64] C. Werner, J. I. Ulacia F, C. Hopfmann, and P. Flynn. Equipment simulation of selective tungsten deposition. *J. Electrochem. Soc.*, 139(2):566–574, 1992.

[65] R. Arora and R. Pollard. A mathematical model for chemical vapor deposition processes influenced by surface reaction kinetics: Application to low-pressure deposition of tungsten. *J. Electrochem. Soc.*, 138(5):1523–1537, 1991.

[66] Y.-F. Wang and R. Pollard. A mathematical model for CVD of tungsten from tungsten hexafluoride and silane. In T. S. Cale and F. S. Pintchovski, editors, *Advanced Metalization for ULSI Applications*, pages 169–175. Materials Research Society, Pittsburgh, PA, 1993.

[67] K.-H. Lie, T. P. Merchant, and K. F. Jensen. Simulation of rapid thermal processing equipment and processes. In J. C. Gelpey, editor, *Rapid Thermal and Integrated Processing II*, volume 303 of *Mat. Res. Soc. Symp. Proc.*, pages 197–209. Materials Research Society, Pittsburgh, PA, 1993.

[68] K. F. Jensen, H.Simka, T. G. Mihopoulos, P. Futerko, and M. Hierlemann. Modeling approaches for rapid thermal chemical vapor deposition: Com-

bining transport phenomena with chemical kinetics. In F. Roozeboom, editor, *Advances in Rapid Thermal and Integrated Processing*, chapter 11, pages 305–331. Kluwer Academic Publisher, Netherlands, 1996.

[69] T. P. Merchant, J. V. Cole, K. L. Knutson, J. P. Hebb, and K. F. Jensen. A systematic approach to simulating rapid thermal processing systems. *J. Electrochem. Soc.*, 143(6):2035–2043, 1996.

[70] S. Chatterjee, I. Trachtenberg, and T. F. Edgar. Mathematical modeling of a single-wafer rapid thermal reactor. *J. Electrochem. Soc.*, 139(12):3682–3689, 1992.

[71] A. J. Toprac, T. F. Edgar, and I. Trachteberg. Modeling of gas-phase chemistry in the chemical vapor deposition of polysilicon in a cold wall system. *J. Electrochem. Soc.*, 140(6):1809–1813, 1993.

[72] A. J. Toprac, I. Trachtenberg, and T. F. Edgar. A predictive model for the chemical vapor deposition of polysilicon in a cold wall, rapid thermal system. *J. Electrochem. Soc.*, 141(6):1658–1663, 1994.

[73] Y. M. Cho, C. D. Schaper, and T. Kailath. In-situ temperature estimation in rapid thermal processing systems using extended Kalman filtering. In *Rapid Thermal and Integrated Processing*, volume 224 of *Mat. Res. Soc. Symp. Proc.*, pages 39–46, Pittsburgh, PA, 1991. Materials Research Society.

[74] C. D. Schaper, Y. M. Cho, and T. Kailath. Low-order modeling and dynamic characterization of rapid thermal processing. *Appl. Phys. A*, 54:317–326, 1992.

[75] Y. M. Cho and T. Kailath. Model identification in rapid thermal processing systems. *IEEE Transactions on Semiconductor Manufacturing*, 6(3):233–245, 1993.

[76] Y. M. Cho, A. Paulraj, T. Kailath, and G. Xu. A contribution to optimal lamp design in rapid thermal processing. *IEEE Transactions on Semiconductor Manufacturing*, 7(1):34–41, 1994.

[77] C. D. Schaper and T. Kailath. Thermal model validation for rapid thermal chemical vapor deposition of polysilicon. *J. Electrochem. Soc.*, 143(1):374–381, 1996.

[78] Y. M. Cho and P. Gyugyi. Control of rapid thermal processing: A system theoretic approach. *IEEE Transactions on Control Systems Technology*, 5(6):644–653, 1997.

[79] C. D. Schaper, T. Kailath, and Y. J. Lee. Decentralized control of wafer temperature for multizone rapid thermal processing systems. *IEEE Transactions on Semiconductor Manufacturing*, 12(2):193–198, 1999.

[80] J. E. J. Schmitz and A. Hasper. On the mechanism of the step coverage of blanket tungsten chemical vapor deposition. *J. Electrochem. Soc.*, 140(7):2112–2116, 1993.

[81] J. J. Thiart and V. Hlavacek. Numerical solution of free-boundary problems: Calculation of interface evolution during CVD growth. *Journal of Computational Physics*, 125:262–276, 1996.

[82] Jung-Hwan Park. *Simulation of Low Pressure Chemical Vapor Deposition Using Combined Reactor Scale and Feature Scale Models.* PhD thesis, Arizonz State University, 1992.

[83] J.-H. Yun and S.-W. Rhee. Simplified simulation of step coverage in chemical vapor deposition with a hemispherical vapor source model. *J. Electrochem. Soc.*, 144(5):1803–1807, 1997.

[84] T. P. Gobbert, T. P. Merchant, L. J. Borucki, and T. S. Cale. A multiscale simulator for low pressure chemical vapor deposition. *J. Electrochem. Soc.*, 144(11):3945–3951, 1997.

[85] S. T. Rodgers and K. F. Jensen. Multiscale modeling of chemical vapor deposition. *J. Appl. Phys.*, 83(1):524–530, 1998.

[86] A. J. Newman. *Modeling and Reduction with Applications to Semiconductor Processing.* PhD thesis, University of Maryland, College Park, 1999.

[87] S. Kommu, G. M. Wilson, and B. Khomami. A theoretical/experimental study of silicon epitaxy in horizontal single-wafer chemical vapor deposition reactors. *J. Electrochem. Soc.*, 147(4):1538–1550, 2000.

[88] S. T. Hsu. *Engineering Heat Transfer.* Van Nostrand Co., Princeton, NJ, 1963.

[89] A. Hasper, J. E. J. Schmitz, J. Holleman, and J. F. Verwey. Heat transport in cold-wall single-wafer low pressure chemical-vapor-deposition reactors. *J. Vac. Sci. Technol. A*, 10(5):3193–3202, 1992.

[90] BTU-ULVAC Inc., North Billerica, MA. *BTU-ULVAC ERA-1000 Selective Tungsten Deposition System*, 1996.

[91] P. J. Timans. Temperature measurement in rapid thermal processing. *Solid State Technology*, 37(4):63–74, 1997.

[92] M. C. Qzturk, F. Y. Sorrell, J. J. Wortman, F. S. Johnson, and D. T. Grider. Manufacturability issues in rapid thermal chemical vapor deposition. *IEEE Transactions on Semiconductor Manufacturing*, 4(2):155–165, 1991.

[93] M. C. Ozturk. Thin-film deposition. In R. B. Fair, editor, *Rapid Thermal Processing: Science and Technology*, pages 110–117, Boston, MA., 1993. Academic Press.

[94] T. Borca-Tasciuc, D. A. Achimov, and G. Chen. Difference between wafer temperature and thermocouple reading during rapid thermal processing. In M. C. Ozturk, F. Roozeboom, P. T. Timans, and S. H. Pas, editors, *Rapid Thermal and Integrated Processing VII*, volume 525 of *Mat. Res. Soc. Symp. Proc.*, pages 103–108, Warrendale, PA, 1998. Materials Research Society.

[95] P. Vandenabeele and W. Renken. Study of repeatability, relative accuracy and lifetime of thermocouple instrumented calibration wafers for RTP. In T. J. Riley et al., editor, *Rapid Thermal and Integrated Processing VI*, volume 470 of *Mat. Res. Soc. Symp. Proc.*, pages 17–22, Pittsburgh, PA, 1997. Materials Research Society.

[96] R. J. Kee, G. Dixon-Lewis, J. Warnatz, M. E. Coltrin, and J. Miller. A FORTRAN computer code package for the evaluation of gas-phase multi-component transport properties. Technical Report SAND86-8246, Sandia National Laboratories, Albuquerque and Livermore, 1986.

[97] P. J. Timans. The thermal radiative properties of semiconductors. In F. Roozeboom, editor, *Advances in Rapid Thermal and Integrated Processing*, chapter 2, pages 35–101. Kluwer Academic, Netherlands, 1996.

[98] T. Sato. Spectral emissivity of silicon. *Japanese J. Applied Physics*, 6(3):339–347, 1967.

[99] J.-M. Dilhac, N. Nolhier, C. Ganibal, and C. Zanchi. Termal modeling of a wafer in a rapid thermal processor. *IEEE Transactions on Semiconductor Manufacturing*, 8(4):432–439, 1995.

[100] Properties of silicon. United Kingdom, 1988.

[101] K. Raznjevic. *Hankbook of Thermodynamic Tables and Charts*. Hemisphere Publishing Co., Washington D. C., 1976.

[102] P. Vandenabeele and W. Renken. The influence of facility conditions on a $\pm 0.25^o$c repeatability lamp voltage controlled RTP system. In T. J. Riley et al., editor, *Rapid Thermal and Integrated Processing VI*, volume 470 of *Mat. Res. Soc. Symp. Proc.*, pages 181–186, Pittsburgh PA, 1997. Materials Research Society.

[103] Computer Boards, Mansfield, MA. *CIO-DAS801 & 802 User's Manual*, revision 1 edition, 1995.

[104] Computer Boards, Mansfield, MA. *CIO-EXP32/16 Hardware Manual*, revision 4 edition, 1994.

[105] National Instruments, Austin, TX. *LabVIEW Reference Manual*, 1996.

[106] L. S. Lerner. *Physics for Scientists and Engineers*. Jones and Bartlett, Sudbury, MA, 1996.

[107] H.-Y. Chang and R. A. Adomaitis. Parameter estimation of a tungsten chemical vapor deposition system using a reduced order model, paper 193c. In *AIChE Annual Meeting*, Dallas, TX, 1999.

[108] H. A. Lord. Thermal and stress analysis of semiconductor wafers in a rapid thermal processing oven. *IEEE Transactions on Semiconductor Manufacturing*, 1(3):105–114, 1988.

[109] S. A. Campbell, K.-H. Ahn, K. L. Knutson, B. Y. H. Liu, and J. D. Leighton. Steady-state thermal uniformity and gas flow patterns in a rapid thermal processing chamber. *IEEE Transactions on Semiconductor Manufacturing*, 4(1):14–19, 1991.

[110] R. A. Adomiatis and Y. h. Lin. A collocation/quadrature-based Sturm-Liouville solver. *Appl. Math. Comp.*, 110:205–223, 2000.

[111] R. A. Adomaitis, Y. h. Lin, and H.-Y. Chang. A computational framework for boundary-value problem based simulations. *Simulation*, 74:30–40, 2000. also in ISR TR 98-41.

[112] Y. h. Lin, H.-Y. Chang, and R. A. Adomaitis. MWRtools: A library for weighted residual method computations. *Computers and Chemical Engineering*, 23:1041–1061, 1999. also in ISR TR 98-24.

[113] Y. h. Lin. *From Detailed Simulation to Model Reduction: Development of Numerical Tools for a Plasma Processing Application.* PhD thesis, University of Maryland, College Park, 1999.

[114] C. A. J. Fletcher. *Computational Galerkin Methods.* Springer-Verlag, New York, 1984.

[115] D. Gottlieb and S. A. Orszag. *Numerical Analysis of Spectral Method: Theory and Applications.* Society for Industrial and Applied Mathematics, Philadelphia, PA, 1977.

[116] C. R. MacCluer. *Boundary Value Problems and Orthogonal Expansions.* IEEE Express, Inc., New York, 1994.

[117] B. Fornberg. *A Practical Guide to Pseudospectral Methods.* Cambridge University Press, New York, 1996.

[118] Suhas V. Patankar. *Numerical Heat Transfer and Fluid Flow.* McGraw-Hill, New York, 1980.

[119] J. H. Ferziger and M. Perić. *Computational Methods for Fluid Dynamics.* Springer-Verlag, New York, 1996.

[120] W. B. Bickford. *A First Course in the Finite Element Method.* Irwin, Inc., 2nd edition, 1994.

[121] D. Funaro. *Polynomial Approximation of Differential Equations.* Springer-Verlag, New York, 1992.

[122] L. Sirovich. Turbulence and the dynamics of coherent structures, part I-III. *Quarterly of Applied Mathematics*, XLV(3):561–590, 1987.

[123] L. Sirovich. Empirical eigenfunctions and low dimensional systems. In L. Sirovich, editor, *New Perspectives in Tubulence*, pages 139–163, New York, 1991. Spring-Verlag.

[124] P. Holmes, J. L. Lumley, and G. Berkooz. *Turbulence, Coherent Structures, Dynamical Systems and Symmetry.* Cambridge University Press, Cambridge, Great Britain, 1996.

[125] G. Berkooz, P. Holmes, and J. L. Lumley. The proper orthogonal decomposition in the analysis of turbulent flows. *Annu. Rev. Fluid Mech.*, 25:539–575, 1993.

[126] R. A. Adomaitis. An orthogonal collocation technique for rapid thermal processing system discretization. Technical Report ISR TR97-63, Institute for Systems Research, University of Maryland, College Park, MD, 1997.

[127] J. Huang. An object-oriented programming approach to implement global spectral methods: Applications to dynamic simulation of a chemical vapor infiltration process. Master's thesis, University of Maryland, College Park, 2000.

[128] L. E. Scales. *Introduction to Non-Linear Optimization.* MacMillan, Hong Kong, 1985.

[129] Y. Bard. *Nonlinear Parameter Estimation.* Academic Press, New York, 1974.

[130] W. H. Press, B. P. Flannery, S. A. Teukolsky, and W. T. Vetterling. *Numerical Recipes in FORTRAN.* Cambridge University Press, New York, 2nd edition, 1992.

[131] J. V. Beck and K. J. Arnold. *Parameter Estimation in Engineering and Science.* John Wiley & Sons, New York, 1977.

[132] H.-Y. Chang and R. A. Adomaitis. Analysis of heat transfer in a chemical vapor deposition reactor: An eigenfunction expansion solution approach. *Int. J. Heat Fluid Flow*, 20:74–83, 1999.